

LOW-STRESS SOLDERING PROCESS TO ASSEMBLE HIGHLY STABLE AND MINIATURIZED LASER RESONATORS



DISSERTATION

for the acquisition of the academic title

Doktor-Ingenieur (Dr.-Ing.)

submitted to the Council of the Faculty of Physics and Astronomy
of the Friedrich-Schiller University of Jena

by Pol Ribes Pleguezuelo

born in Molins de Rei, Catalonia/Spain on 14.08.1984

Supervisors:

Major Supervisor: Prof. Dr. Andreas Tünnermann,
Friedrich-Schiller-Universität Jena

Associate Supervisor: Prof. Dr. Frank Schmidl
Friedrich-Schiller-Universität Jena

Associate Supervisor: Prof. Dr. Reinhart Poprawe
Fraunhofer-Institute für Lasertechnik Aachen

Day of the Disputation: 14th of February 2018

Abstract

Due to a higher variety of laser applications, laser manufactures are nowadays pushed to build compact and robust devices, which are able to perform in more stringent conditions. To achieve such demands, the common assembling techniques using clamping or adhesive means have to be replaced by more sophisticated approaches. These should guarantee the miniaturization of devices (avoiding clamping methods), and include more robust techniques that could offer higher operational thermal range, vacuum compatibility or even being able to withstand space radiation (avoiding adhesive techniques). Techniques as the low-stress soldering solderjet bumping can minimize the input of thermal energy by the application of a precise energy solder reflow through a laser pulse. This allows for the assembly of brittle materials as glasses, crystals or ceramics, and guarantees the possibility of components miniaturization, even assuring higher and more robust bound strengths. Furthermore, it avoids current technologies state of the art constrains as outgassing, and improves its thermal and electrical conductivity device's performances.

However, in order to develop miniaturized laser devices, small-induced stresses produced by soldering techniques as solderjet bumping have to be investigated to guarantee that the stress-induced birefringence effects do not alter the device laser emission. To do so, a method to simulate induced stresses for a laser crystal packaging technique and the consequent study of birefringent effects inside the laser cavities has been developed. The method has been implemented by thermo-mechanical simulations by using ANSYS 17.0. ANSYS results were later imported into a VirtualLab Fusion software package where input/output beams in terms of wavelengths and polarization were analyzed. The outcome of the analysis showed no significant difference between the input and output laser beams using, as an example, few millimeters size components assembled by solderjet bumping technology means.

A miniaturized diode-pumped solid-state laser designed as part of the Raman Laser Spectrometer instrument for the European Space Agency Exomars mission 2020 has been assembled and tested according with the mission's purpose and requirements. Two different processes were compared for the laser assembling: one based on adhesives, following traditional laser manufacturing processes; another by the solderjet bumping technology. The manufactured devices were tested for the processes validation by passing mechanical, thermal cycles, radiation and optical functional tests. The comparison analysis showed a device improvement in terms of reliability of the optical performances from the assembled by adhesive means to the soldered devices. This made the solderjet bumping technique be the final selected candidate to assemble by soldering means the Exomars Flight Module (FM) laser that will be send in 2020 direction to Mars, to search for signs of past or present life on the red planet. The Exomars miniaturized and soldered laser will be the first fully-assembled laser by soldering means that travels to space.

Table of Contents

| | |
|--|-----------------|
| Abstract | <i>i</i> |
| 1 Introduction | 4 |
| 1.1 Motivation..... | 4 |
| 1.2 Objectives of the research..... | 5 |
| 2 Background of the study | 7 |
| 2.1 State of the art..... | 7 |
| 2.1.1 Optical components packaging..... | 7 |
| 2.1.2 Solderjet bumping technology..... | 10 |
| 2.1.2.1 Fineplacer®..... | 12 |
| 2.2 Bonded components verification tools..... | 13 |
| 2.2.1 Stress measurement..... | 14 |
| 2.2.2 Bond strength and applied loads..... | 15 |
| 2.2.2.1 Push tests tools..... | 15 |
| 2.2.2.2 Climatic chamber..... | 16 |
| 2.3 Stress and induced birefringence..... | 16 |
| 2.3.1 Stress-induced Birefringence in laser components..... | 20 |
| 2.3.2 Laser emission..... | 22 |
| 2.3.3 Birefringence effects to the laser emission..... | 23 |
| 2.3.4 Electromagnetic field propagation and depolarization calculation in stress-induced laser crystals..... | 25 |
| 2.3.5 Simulations softwares..... | 27 |
| 2.3.5.1 Mechanical analysis by ANSYS 17.0..... | 28 |
| 2.3.5.2 Optical analysis by VirtualLab Fusion..... | 28 |
| 3 Theoretical modelling and testing | 30 |
| 3.1 Theoretical Modelling..... | 30 |
| 3.1.1 Initial opto-mechanical stress simulations with ANSYS and VirtualLab Fusion..... | 31 |
| 3.1.1.1 Simulations assumptions..... | 31 |
| 3.1.1.2 ANSYS thermo-mechanical initial results..... | 34 |
| 3.1.1.3 Piezo-optic tensor and crystal orientation..... | 35 |

| | | |
|----------|---|------------------|
| 3.1.1.4 | FEM stress results imported in VirtualLab..... | 38 |
| 3.2 | Initial soldering tests | 42 |
| 3.2.1 | Material soldering parametrization | 42 |
| 3.2.1.1 | Soldering response | 44 |
| 3.2.2 | Comparison of simulated and measured stress | 49 |
| 4 | <i>Devices miniaturization</i> | 52 |
| 4.1 | Soldering optimization for device miniaturization tests | 52 |
| 4.2 | Optimization soldering results..... | 53 |
| 4.3 | Push and climatic tests results | 57 |
| 4.3.1 | Initial not cycled push tests..... | 58 |
| 4.3.2 | Climatic chamber test | 59 |
| 4.3.3 | Push test after thermal cycles | 60 |
| 4.4 | Optimization results and conclusions..... | 61 |
| 5 | <i>Case study and design guidelines</i> | 63 |
| 5.1 | Exomars laser | 63 |
| 5.1.1 | Laser device background | 63 |
| 5.1.2 | Laser characteristics and requirements..... | 65 |
| 5.1.3 | Exomars' laser design | 66 |
| 5.2 | Assembly methods..... | 68 |
| 5.2.1 | Adhesive based procedures | 69 |
| 5.2.1.1 | FEM analysis for the adhesive based assemblies..... | 70 |
| 5.2.2 | Low-stress soldering based procedures | 71 |
| 5.2.2.1 | VirtualLab Fusion soldered Exomars laser results | 80 |
| 5.2.2.2 | FEM structural analysis for the low-stress technology assemblies..... | 85 |
| 5.2.2.3 | Power loss due to components metallization | 86 |
| 5.3 | Performed environmental tests on adhesive and soldered devices..... | 88 |
| 5.4 | Results and conclusions | 90 |
| 6 | <i>Conclusions and outlook</i> | 95 |
| | <i>References</i> | <i>i</i> |
| | <i>Nomenclature</i> | <i>xi</i> |

| | |
|---------------------------------------|--------------|
| <i>List of publications</i> | <i>xiv</i> |
| <i>Acknowledgements</i> | <i>xviii</i> |
| <i>Ehrenwörtliche Erklärung</i> | <i>xx</i> |

1 Introduction

1.1 Motivation

Miniaturized laser systems e.g. for Raman spectroscopy or laser based fuel ignition requires high performance in beam, power, and wavelength stability. In addition, the devices used in space or for high temperature applications need to be able to perform in harsh environments usually with minimized volume and weight. The standard precision joining technologies of adhesive bonding using polymer-based glues are inadequate due to temperature instability, volume change over time, and outgassing. Examples of this can be found in the literature, as on the carried out studies for the space laser ALADIN [1], at which intensive analysis to avoid outgassing problems and consequent laser-induced contamination (LIC) were performed (Fig 1.1); or, on the components stability, to robustly assemble a miniaturized diode-pumped solid-state laser (DPSSL) required for the Exomars mission (Fig 1.2) [2], [3].

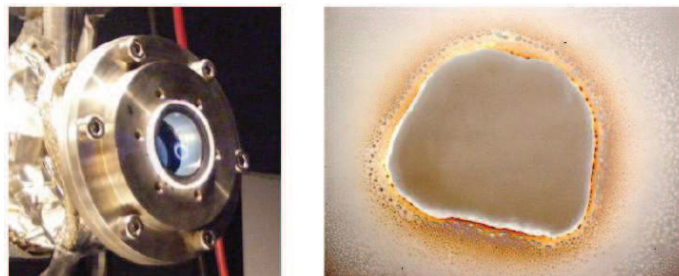


Fig. 1.1. Left, LIC deposition on the window of the vacuum chamber. Right, detail of a LIC deposition [1].

Introducing inorganic solder alloys as an alternative joining media allows for an improved performance, with higher stability and robustness, wider thermal conductivity performance, higher vacuum and radiation compatibility, and longer-term performance. On the other hand, soldering introduces a thermo-mechanical impact during joining and a higher inherent stress at the joint, which can cause a degradation of laser resonators due to stress-induced birefringence and deformation of laser components. With the assembling induced component birefringence, that ultimately affects the components internal index of refraction, the assembled laser crystals could have a variation of the desired optical performances in

terms of laser depolarization, increased M^2 factor, or even changes on the laser output power, which can modify the initial optical performances selected for the designed laser resonator. To combine the much better stability and robustness of miniaturized soldered laser resonators with a low impact on the alignment and birefringence, solder alloys with low impact by thermal reflow using laser technologies were investigated in this work.

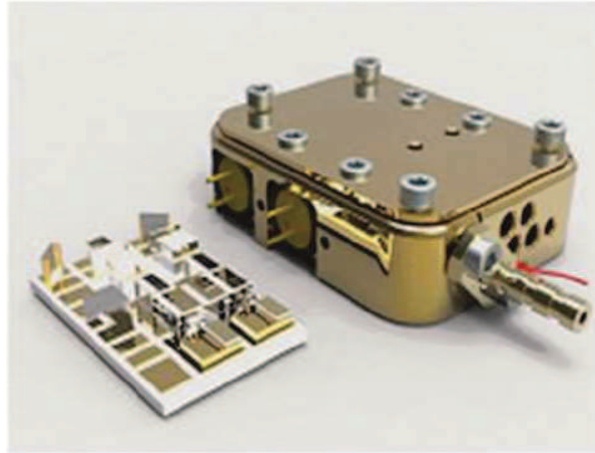


Fig. 1.2. Design of the first investigated laser prototypes for the European Space Agency (ESA) Exomars project. The initial laser device was designed and assembled by adhesive means [3].

1.2 Objectives of the research

Starting from an optical design that combines an Yttrium Aluminium Garnet (YAG) and a second harmonic generation Beta Barium Borate (BBO), a mechano-optical model (analytical basis and Finite Element Method) will be generated to describe the relations between areal distribution of mechanical stress introduced from the boundaries of the resonator components by the soldering technology and the optical performance of the miniaturized resonators.

→ Objective 1: Create a theoretical model design that relates induced packaging stress, induced birefringence and cavity lasers output misbehaviors.

For the main goal of investigating and optimizing the soldering technology, the joint geometries and reflow parameters will be modelled and varied in detail to study the specific influence of the laser beam soldering process on the inherent performance of the miniaturized laser setup, during their assembly. The model of the laser beam soldering process needs in particular to take into account locally introduced inherent joint stress and

deformation during thermal reflow of the solder, which is especially important for birefringence-based effects in active laser crystals and misalignment of passive beam shaping.

→ **Objective 2:** Investigate the laser based soldering technique used to assemble laser devices, and get the basic knowledge of minimum laser cavities sizes without affecting laser output performances (beam depolarization and beam quality).

Then, soldering techniques will be compared to clamping or adhesive techniques to evaluate and prove better performance under highly aggressive environments.

→ **Objective 3:** Compare former assembling techniques with new soldering assembling techniques. Investigate the use of new laser assembling techniques that could work beyond the actual state of the art in terms of robustness.

As a result, a design and technology guideline is derivated, enabling to transfer the results of the specific component investigated to a miniaturized resonator design. The work will involve as an example, the study, modelling, and assembly of a miniaturized frequency doubling DPSS laser device, suitable for use e.g. in Raman spectroscopy under specific space conditions.

→ **Objective 4:** Achieve laser operation of the device assembled by soldering techniques, being able to perform in harsh environmental conditions.

The finally assembled devices will have to pass engineering qualification model tests under specific environmental conditions to assess that soldered prototypes can successfully operate for the purpose and goals of a required scientific space instrument.

2 Background of the study

2.1 State of the art

2.1.1 Optical components packaging

Depending on the designed setup and/or the bonding materials in use, the standard joining techniques can be summarized as they are classified on Fig. 2.1,

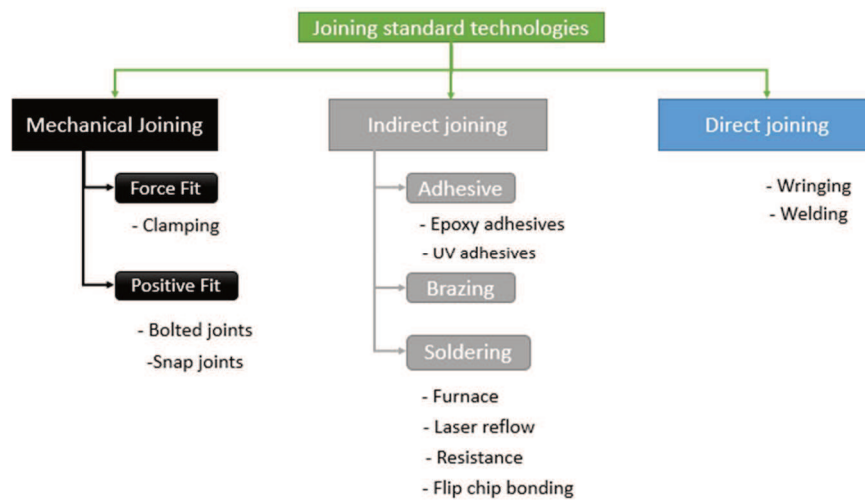


Fig. 2.1. Different joining standard technologies [4]-[5].

For the last few decades and although the wide range of possibilities, optical manufacturing industries have mainly performed their optical assemblies by using polymeric adhesives or different types of clamping methods. These techniques guaranteed low cost manufacturing, adequate optical alignment accuracy, and a relatively long-term performance. For instance, the use of adhesives provided the benefits of bonding the components without an otherwise required pre-treatment, easy integration for 6 degrees of freedom (DOF) arrangements, and in general thanks to the adhesives elasticity, a relative easy process to join materials with different coefficient of thermal expansion (CTE). On the other hand, clamping methods provided a proper solution to robustly assemble complex 3D geometries for which the maximum device size and weight was not an important constrain. Although these techniques could still be an adequate solution for some optical systems, those

who want to guarantee: wider operational and storage temperatures ranges, outgassing free on vacuum, high thermal and electrical conductivity, better reliability on space projects exposed to space radiation and high vibrational conditions; should look for new joining techniques with higher robustness and better alignment features. Today, several soldering techniques for optical components can be implemented in order to overcome these constrains. The benefits and constrains of the formerly used techniques and the newly soldering available technologies for optical components, are compared on Table 2.1.

Table 2.1. Comparison among gluing, soldering, and clamping technologies for optical elements [6].

| Properties | Bonding | | Clamping |
|---|--|--|---|
| | Gluing | Soldering | |
| Temperature stability | < 120° (Optical UV glues) | < 450° | - (compensation of different components CTE) |
| Radiation resistance (required for space applications) | -- (deterioration of organic materials) | ++ | + |
| Long term stability | - (deterioration of organic materials) | + | + - |
| Transparency | ++ | -- (no transparent) | -- (generally no transparent) |
| Conductivity | - (thermal conductivity ~0.10-3.0 W/(m K) @25 °C) | ++ (thermal conductivity ~10-80 W/(m K) @25 °C) | + - (depends on materials used) |

| | | | |
|----------------------------|--|--|--|
| Stress compensation | ++ (low shrinkage down to 0.2%) | - (requires input of thermal energy (~ 200 °C) to bond components) | - (requires force to robustly fasten components) |
| Low outgassing | -- (outgassing due to the use of organic components- e.g. Minimum Total Mass Loss ~1 %) | ++ (for metals normally $10^{-12} \dots 10^{-14}$ mbar l/s/cm ² @450 °C) | + - (depends on the used materials. E.g. low outgassing peek Total Mass Loss 0.31 %) |

As an example, the formally used technologies would be hardly used in laser devices for space applications, because of adhesive outgassing problems that would result in LIC and laser-induced damage (LID) [1],[7], or because of the relatively large size and weight required for clamping methods [2],[8]. Several other options using soldering techniques for optic components are described in the literature. Examples of those are:

- the Leica Geosystems AG three-dimensional miniaturized optical surface-mounted devices or “TRIMO”, an automated assembly technique for small optical components [9],
- the Carl Zeiss SMT method and device for connecting an optical element to a frame [10],
- the Osram Opto Semiconductors GmbH arrangement of micro-optical components on substrates [11];
- the Fraunhofer IOF transmission laser beam soldering technique using thin film solder layers [12],
- and the Fraunhofer IOF laser-based solderjet bumping technique [13].

Each of these different techniques can be used with different materials and/or by different preformed shapes to guarantee that the overall result conforms to the requirements specified by the end user's needs. Also, each of these techniques use distinct approaches to

reflow and finally solder the desired materials and components (Fig. 2.2), for which different amount of thermal input of energy is required.

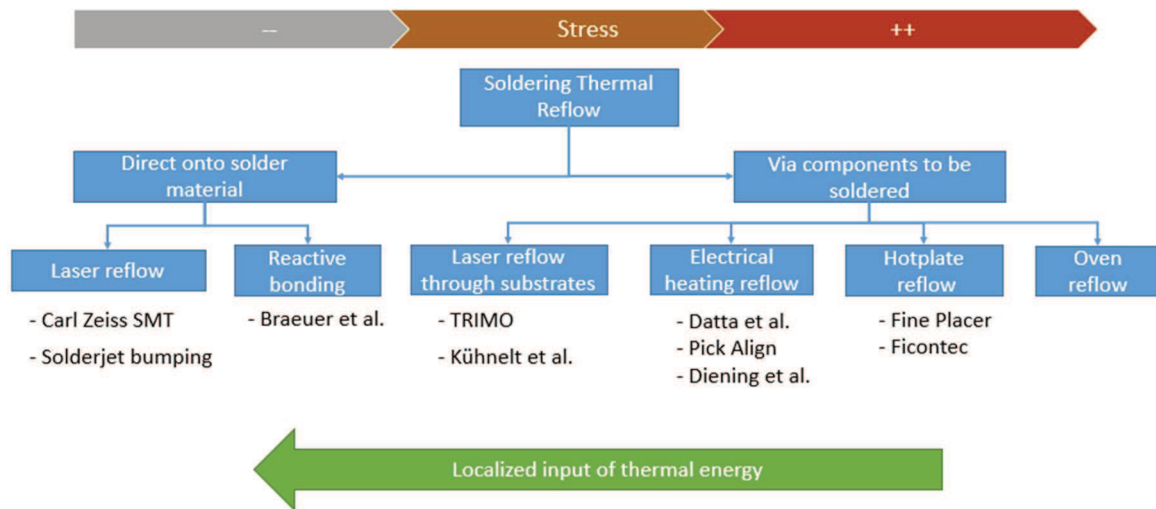


Fig. 2.2. Examples of soldering techniques that can be used to assemble optical components classified according to the soldering input of thermal energy to reflow the alloy: CarZeiss SMT [10], Solderjet bumping [13], Braeuer et al. [14], TRIMO [9], Kühnelt et al. [11], Datta et al. [15], Pick Align [16], Diening et al. [17], Fine Placer [18], and Ficontec [19].

In our case study, and considering the advantages showed in Table 2.1, the solderjet bumping technique was selected. Moreover, this technique can guarantee solder alloy application into complex 3D geometries and low-induced stress onto the components to be bound by the application of localized input of thermal energy, in contrast with similar techniques mentioned above. A comparison study among techniques used to assemble optical crystals (including the solderjet bumping technique) can be found in [8].

2.1.2 Solderjet bumping technology

Solder-joining using metallic solder alloys is an alternative to adhesive bonding. Laser-based soldering processes are especially well suited for the joining of optical components made of fragile and brittle materials such as glasses, ceramics and crystals, due to a localized and minimized input of thermal energy [13]. Different techniques of heating solder alloys by laser irradiation are proposed using either the thin film solder layers [12], such as Pick&Align resistance soldering technique [16],[20] or the jetting of laser-molten solder droplets [13]. Solderjet bumping is a technique adapted from flip chip processing of semiconductor devices that also allows for the flux-free and contact-free processing of

optical components and 3D-packaging. It uses spherical solder preforms of various soft solder alloys (e.g. tin-based lead-free solders, low melting indium alloys or high melting eutectic gold-tin, gold-silicon or gold-germanium solders) in a diameter range of 40 μm to 760 μm . The solder spheres are transferred from a reservoir to a placement capillary with a conical tip and an inner diameter that is slightly smaller than the diameter of the spheres. After positioning the capillary next to the joining geometry using an articulating robot or a gantry system, the solder alloy is molten by an infrared laser pulse and jetted out of the capillary by applying nitrogen pressure. The jetting of liquid solder volumes provides a very good thermal contact of the alloy with the components, and allows for the joining within complex 3D-integrated geometries. The bond head of the solderjet bumper integrates solder volume feeding, reflow and application of liquid solder droplets in a compact device and allows for highly automated and flexible use (see Fig. 2.3).

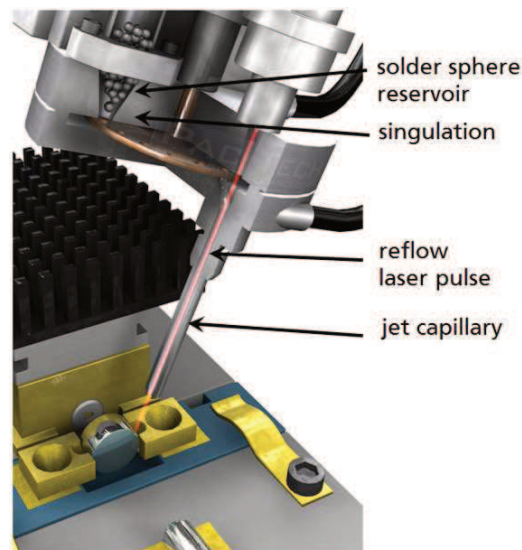


Fig. 2.3. Schematic drawing of the solderjet bond head able to solder droplets with 6 degrees of freedom (DOF).

However, the formation of a metallic solder joint using components made of non-metallic materials with solderjet bumping requires a wettable metallization layer applied to the components. Such surfaces can be provided by thin film (e.g. physical vapour deposition) or thick film (e.g. screen printing of metal pastes) processes. Sputtered three-layer systems using titanium adhesion layer, a platinum diffusion barrier, and a noble gold finish preventing oxidization and acting as a wetting surface, provide superb conditions for wetting of liquid solder droplets (Fig. 2.4).

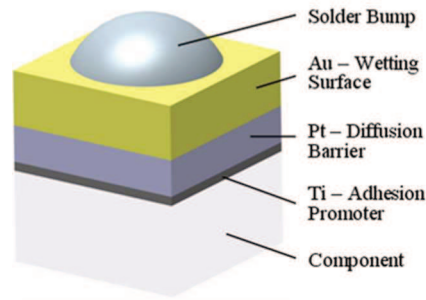


Fig. 2.4. Example of three sputtered layers (Ti/Pt/Au) over the substrate component to later be able to create a wettable surface for the solder bump.

Typical photonic applications of solderjet bumping are described in the literature [13]. Sub-micron accuracy in placement of components, direct fiber coupling by soldering of polarization maintaining fibers and the hermetic sealing of an endoscopic tip are reported. Further examples show the mounting of sensitive micro-optical components such as gradient-index lenses [21]. The assembly of a multi-beam deflection array for next-generation lithography outlines the features of this soldering technique with respect to vacuum compatibility and very high component placement accuracy. Silicon-based micro-structured MEMS devices for the deflection of multiple electron beams are precisely attached to ceramic carrier substrates utilizing both mechanical fixation and electrical contacting by the solder joint [22].

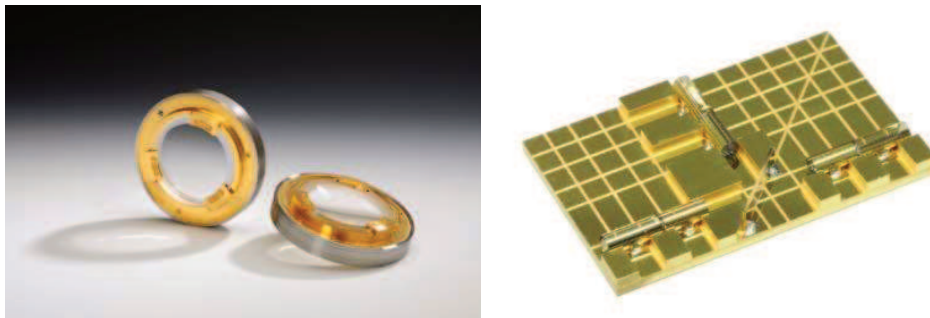


Fig. 2.5. Examples of solderjet bumping assemblies. Left, lens mount geometry soldered with solderjet bumping technique [23]. Right, wavelength division multiplexing device for optical measurements assembled by similar means [21].

2.1.2.1 Fineplacer®

Although the work in this dissertation is focused on localized and minimized input of thermal energy, in some cases a Fineplacer device (Fig 2.6) in combination to solderjet bumping technology was used to reflow the pre-applied bumps, as described in chapter 5.2.2.

The Fineplacer lambda (Finetech GmbH & Co.) is a technology used to sub-micron position and assemble components based on flip-chip reflow soldering.



Fig. 2.6. Fineplacer lambda from Finetech GmbH & Co. It contains two cameras (left and over the device) to allow fine adjustments, an operating plate with the pick-up tool and a hot plate; and a computer to program temperature profiles [18].

The Fineplacer lambda is designed for applications as laser-bar and diode-bonding, VCSEL/photodiode bonding or multi-stage assembly of opto-electro-mechanical systems. Its interchangeable pick-up tools guarantee the possibility to adapt it to a whole range of different applications [18]. The bonding material can be applied by using different methods. In our case, the components to be bond which did not need 3D positioning were initially bumped by the use of solderjet bumping technology. Later, the bumped components were precisely positioned over the substrate components through the pickup tool. Finally, the components were thermally reflowed to the alloy melting temperature by the use of the pick-up tool and hot plate heated surfaces.

2.2 Bonded components verification tools

After laser components assembling, the glasses and crystals will firstly need to be analysed to guarantee low-induced stress and consequent stress-induced birefringence on them. To do so, the real induced stress will be empirically analysed after soldering, by using a polarimeter device. Secondly, push and ambient tests will be performed to assess if the assembled devices will be capable to experience external loads, since our goals is to robustly assemble miniaturized laser devices.

2.2.1 Stress measurement

A polarimeter device is an instrument able to study the induced stress on transparent materials by analysing the anisotropy of the velocity of the light when travelling across the material, and by calculating the light retardation of different wavelength polarizations (Fig. 2.7). This can be explained with,

$$\Delta = \frac{\alpha\lambda}{180^\circ} \quad (2.1)$$

where Δ is the optical retardation calculated in nm, α the polarization angle and λ the wavelength of the used light across the component.

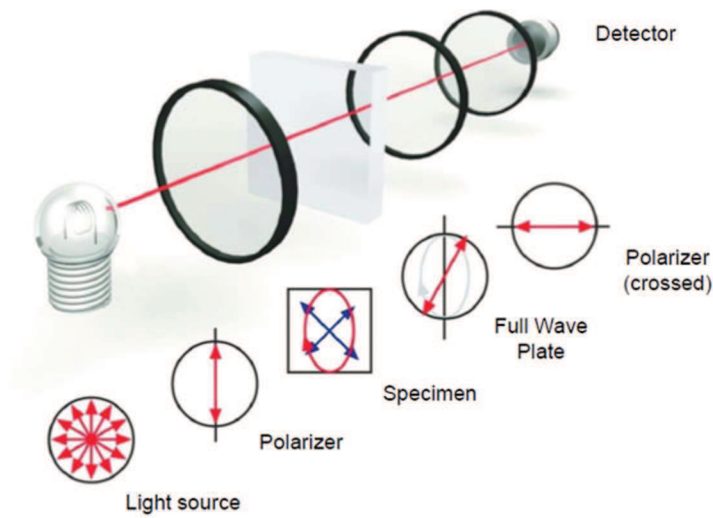


Fig. 2.7. Schematic of Ilis polarimeter functionality [24].

This effect can also be explained by the presence of induced stress on a laser crystal, for which, the internal refractive index is changed altering consecutively the propagation of light. The phase difference of the propagated light through a stress material can be expressed as follows,

$$\Delta = \frac{2\pi t}{\lambda} (n_1 - n_2) \quad (2.2)$$

where t is the component thickness. Using the following chapter 2.3.1 equations, this can be later transformed into the studied material stresses by using the piezo-optical constant tensor π_{ijkl} ,

$$(\sigma_1 - \sigma_2) = \frac{\Delta\lambda}{2\pi t \pi_{ijkl}} \quad (2.3)$$

where $(\sigma_1 - \sigma_2)$ is the produced stress, and π_{ijkl} the piezo-optic constant tensor expressed on the analysed light propagation direction as will be extensively described on chapter 2.3.4.

2.2.2 Bond strength and applied loads

As mentioned on previous chapters, one of the main advantages of soldering optical components is the possibility of obtaining robust assembled devices able to perform in harsh environmental conditions. The robustness-limiting factor for the components assembled by the solderjet bumping technique is supposed to be the soldering alloy ultimate tensile strength (UTS); as an example 45 MPa for SAC305 alloy. In order to optimize the soldering approach by minimizing the induced stress and maximizing the soldering bond strength, the bond component strength was studied by push tests analysis before and after ambient tests.

As an example, the maximum required loads for the Exomars mission payload and devices (since it contains a DPSSL) [25], were used to asses if the chosen assembling technique can assure enough laser device robustness.

2.2.2.1 Push tests tools

After assembling the components, the joint strength has been studied by pushing until tearing the assembled components apart by using a Zwick Roell Z020 (Fig.2.8).



Fig. 2.8. Schematic of Zwick Roell Z020 [26].

With the tensile ultimate strength of the applied alloy, it was used the following formula to estimate, compare, and to prove if the joint between components has been successfully achieved with the desired bond strength,

$$F = A * UTS \quad (2.4)$$

where F is the resulting bond strength force in N, A the alloy covered area, and UTS the ultimate tensile strength of the alloy used material (45 MPa for SAC305). For small optical components similar to 2 mm (YAG or BBO) cube sides, the maximum loads required for a space mission such as Exomars would be below 1 N [25].

2.2.2.2 Climatic chamber

Following Exomars mission space requirements [25], a climatic chamber model TCH7050 from TIRA Umweltsimulation GmbH was used to test the soldered samples, in an eight temperature cycles between -60 °C to +70 °C, with a dwell time >15 minutes and with an approximate ramp of 1 °C/min (Fig. 2.9).

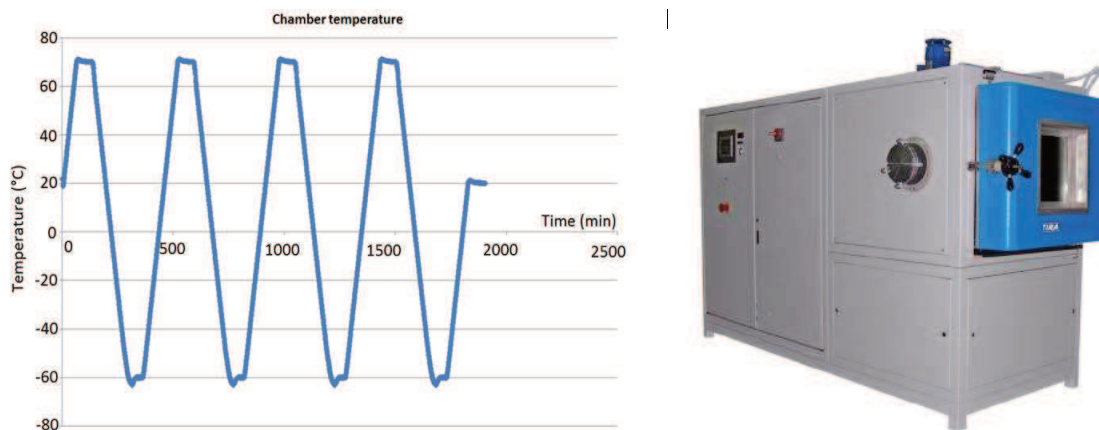


Fig. 2.9. Left, temperature profile used to test bonded samples. Right, TCH7050 from TIRA Umweltsimulation GmbH [27].

The samples were inspected with a microscope after the tests, and the resulting bond strength after thermal loads studied again by a push tests analysis.

2.3 Stress and induced birefringence

Laser components assembled with solderjet bumping technique can be bonded with a small induced stress; however, laser components for miniaturized laser devices requires an additional study to guarantee that this small induced stress does not affect the laser crystal

resonator configuration with a consequent change on the laser beam emission, as an example. For that reason, a deep study on soldering induced stress on laser components had to be carried out. In general, a uniaxial stress produced in a body can be described as the result of an external applied force per unit per area as,

$$\sigma = \frac{F}{A} \quad (2.5)$$

The induced stress produced by soldering laser components with solderjet bumping technology is caused by mechanical-stress due to alloy shrinkage during alloy cooling down; but mainly by thermal stress due to differences on the materials CTE's. This last effect is expressed by Liu et al. [35] as,

$$\sigma = E\Delta\alpha\Delta T \quad (2.6)$$

where E is the Young's Modulus, $\Delta\alpha$ the differences of the materials CTE's, and ΔT the temperature difference between alloy solidification and room temperature.

This applied force on a body, produces a body deformation or strain that can be calculated through to the Young Modulus and Poisson ratio material properties. Using Hooke's law for an isotropic linear material, the relation between tensile stress (σ), extensional strain (ϵ) and the Young Modulus (E) can be expressed as [28]-[29],

$$E = \frac{\sigma}{\epsilon} \quad (2.7)$$

To obtain more accurate 3D-geometry approximation, the Hooke's Law needs to be substituted for second rank tensors expression as,

$$\sigma_{ij} = c_{ijkl}\epsilon_{kl} \quad (2.8)$$

where σ_{ij} and ϵ_{kl} are the induced vector principal stresses and vector principal strains; respectively, and c_{ijkl} the elastic stiffness with 81 constants values tensor directly related with the Young's Modulus and Poisson's ratio (Eq. (2.12)). This four-rank tensor can be reduced (even in presence of stress) due to the crystals symmetry, to a second-rank matrixes using Voigt notation and Nye's convention with Table 2.2,

Table 2.2. From matrix to tensor notation using Voigt notation and Nye's convention.

| | | | | | | |
|-----------------|----|----|----|-------|-------|-------|
| Tensor notation | 11 | 22 | 33 | 23,32 | 31,13 | 12,21 |
| Matrix notation | 1 | 2 | 3 | 4 | 5 | 6 |

Thus, being able to express the above-mentioned tensors for the stress,

$$\begin{bmatrix} \sigma_{11} & \sigma_{12} & \sigma_{13} \\ \sigma_{21} & \sigma_{22} & \sigma_{23} \\ \sigma_{31} & \sigma_{32} & \sigma_{33} \end{bmatrix} \rightarrow \begin{pmatrix} \sigma_1 & \sigma_6 & \sigma_5 \\ \sigma_6 & \sigma_2 & \sigma_4 \\ \sigma_5 & \sigma_4 & \sigma_3 \end{pmatrix} \rightarrow \begin{pmatrix} \sigma_x \\ \sigma_y \\ \sigma_z \\ \sigma_{xy} \\ \sigma_{zx} \\ \sigma_{zy} \end{pmatrix} \quad (2.9)$$

and similarly, for the strain,

$$\begin{bmatrix} \epsilon_{11} & \epsilon_{12} & \epsilon_{13} \\ \epsilon_{21} & \epsilon_{22} & \epsilon_{23} \\ \epsilon_{31} & \epsilon_{32} & \epsilon_{33} \end{bmatrix} \rightarrow \begin{pmatrix} \epsilon_1 & \frac{1}{2}\epsilon_6 & \frac{1}{2}\epsilon_5 \\ \frac{1}{2}\epsilon_6 & \epsilon_2 & \frac{1}{2}\epsilon_4 \\ \frac{1}{2}\epsilon_5 & \frac{1}{2}\epsilon_4 & \epsilon_3 \end{pmatrix} \rightarrow \begin{pmatrix} \epsilon_x \\ \epsilon_y \\ \epsilon_z \\ \frac{1}{2}\epsilon_{xy} \\ \frac{1}{2}\epsilon_{zx} \\ \frac{1}{2}\epsilon_{zy} \end{pmatrix} \quad (2.10)$$

reducing the independent components. Being σ_{ij} symmetric even with the existence of external forces, one can assume that it is also true for the elastic-stiffness constant's tensor, and its symmetry is also maintained with, $c_{ijkl} = c_{ijlk}$ and $c_{ijkl} = c_{jikl}$, reducing the independent components of 81 values tensor to a 36 constant values matrix. Using Nye's notation is possible reduce and write c_{ijkl} as,

$$c_{ijkl} = \begin{bmatrix} c_{1111} & c_{1122} & c_{1133} & c_{1123} & c_{1131} & c_{1112} & c_{1132} & c_{1113} & c_{1121} \\ c_{2211} & c_{2222} & c_{2233} & c_{2223} & c_{2231} & c_{2212} & c_{2232} & c_{2213} & c_{2221} \\ c_{3311} & c_{3322} & c_{3333} & c_{3323} & c_{3331} & c_{3312} & c_{3332} & c_{3313} & c_{3321} \\ c_{2311} & c_{2322} & c_{2333} & c_{2323} & c_{2331} & c_{2312} & c_{2332} & c_{2313} & c_{2321} \\ c_{3111} & c_{3122} & c_{3133} & c_{3123} & c_{3131} & c_{3112} & c_{3132} & c_{3113} & c_{3121} \\ c_{1211} & c_{1222} & c_{1233} & c_{1223} & c_{1231} & c_{1212} & c_{1232} & c_{1213} & c_{1221} \\ c_{3211} & c_{3222} & c_{3233} & c_{3223} & c_{3231} & c_{3212} & c_{3232} & c_{3213} & c_{3221} \\ c_{1311} & c_{1322} & c_{1333} & c_{1323} & c_{1331} & c_{1312} & c_{1332} & c_{1313} & c_{1321} \\ c_{2111} & c_{2122} & c_{2133} & c_{2123} & c_{2131} & c_{2112} & c_{2132} & c_{2113} & c_{2121} \end{bmatrix} \quad (2.11)$$

$$\equiv \begin{pmatrix} c_{11} & c_{12} & c_{13} & c_{14} & c_{15} & c_{16} \\ c_{21} & c_{22} & c_{23} & c_{24} & c_{25} & c_{26} \\ c_{31} & c_{32} & c_{33} & c_{34} & c_{35} & c_{36} \\ c_{41} & c_{42} & c_{43} & c_{44} & c_{45} & c_{46} \\ c_{51} & c_{52} & c_{53} & c_{54} & c_{55} & c_{56} \\ c_{61} & c_{62} & c_{63} & c_{64} & c_{65} & c_{66} \end{pmatrix}$$

The inverse of the piezo-optic tensor matrix can be then also expressed in terms of Young modules and the Poisson ratio. The 36 constant matrix can be differently expressed depending on the crystal internal structure. As an example, for the case of isotropic materials this expression is written as,

$$c^{-1} = \begin{pmatrix} 1/E_x & -v_{xy}/E_x & -v_{xz}/E_x & 0 & 0 & 0 \\ -v_{yx}/E_y & 1/E_y & -v_{yz}/E_y & 0 & 0 & 0 \\ -v_{zx}/E_z & -v_{zy}/E_z & 1/E_z & 0 & 0 & 0 \\ 0 & 0 & 0 & \frac{2(1+v_{xy})}{E_x} & 0 & 0 \\ 0 & 0 & 0 & 0 & \frac{2(1+v_{yz})}{E_y} & 0 \\ 0 & 0 & 0 & 0 & 0 & \frac{2(1+v_{xz})}{E_z} \end{pmatrix} \quad (2.12)$$

Where being c^{-1} symmetric also [30], one can simplify the matrix in terms of the Young Modulus and the Poisson's ratio with the following equivalences because of the isotropic behaviour with,

$$\begin{aligned} \frac{v_{yx}}{E_y} &= \frac{v_{xy}}{E_x} \\ \frac{v_{zx}}{E_z} &= \frac{v_{xz}}{E_x} \\ \frac{v_{yz}}{E_z} &= \frac{v_{yz}}{E_y} \end{aligned} \quad (2.13)$$

reducing, for isotropic materials, this expressions to a three independent constant values matrixes,

$$c^{-1} = \begin{pmatrix} c_1 & c_2 & c_2 & 0 & 0 & 0 \\ c_2 & c_1 & c_2 & 0 & 0 & 0 \\ c_2 & c_2 & c_1 & 0 & 0 & 0 \\ 0 & 0 & 0 & c_3 & 0 & 0 \\ 0 & 0 & 0 & 0 & c_3 & 0 \\ 0 & 0 & 0 & 0 & 0 & c_3 \end{pmatrix} \quad (2.14)$$

with this consideration Eq. (2.8) can be expressed for general materials as,

$$\begin{pmatrix} \sigma_x \\ \sigma_y \\ \sigma_z \\ \sigma_{xy} \\ \sigma_{zx} \\ \sigma_{zy} \end{pmatrix} = \begin{pmatrix} c_{11} & c_{12} & c_{13} & c_{14} & c_{15} & c_{16} \\ c_{21} & c_{22} & c_{23} & c_{24} & c_{25} & c_{26} \\ c_{31} & c_{32} & c_{33} & c_{34} & c_{35} & c_{36} \\ c_{41} & c_{42} & c_{43} & c_{44} & c_{45} & c_{46} \\ c_{51} & c_{52} & c_{53} & c_{54} & c_{55} & c_{56} \\ c_{61} & c_{62} & c_{63} & c_{64} & c_{65} & c_{66} \end{pmatrix} \times \begin{pmatrix} \epsilon_x \\ \epsilon_y \\ \epsilon_z \\ \frac{1}{2}\epsilon_{xy} \\ \frac{1}{2}\epsilon_{zx} \\ \frac{1}{2}\epsilon_{zy} \end{pmatrix} \quad (2.15)$$

where the independent values of c_{ijkl} will depend on the crystal internal structure to be studied [28].

2.3.1 Stress-induced Birefringence in laser components

A mechanical stress induced onto a laser crystal simultaneously generates an anisotropic density distribution on the component, that creates differences in the material's refractive indices mathematically defined by the indicatrix (represented as an ellipsoid that describes the different velocities of light passing through the material) [28],[31]. The effect of different light velocities travelling inside a component that creates an optical anisotropy is also called birefringence. This effect can be described as changes on the material indicatrix B_{ij} with [32],

$$B_{ij} = B_{0,ij} + \Delta B_{ij} \quad (2.16)$$

with $i, j = 1, 2, 3$ respectively. The second-rank tensor $B_{0,ij}$ represents the free-of-stress indicatrix tensor, and ΔB_{ij} represents the indicatrix changes produced due to induced stress, which can also be expressed as,

$$\Delta B_{ij} = \pi_{ijkl} \sigma_{kl} \quad (2.17)$$

where $k, l = 1, 2, 3$, and the Einstein's summation rule is applied here. The second-rank tensor σ_{kl} represents the induced vector principal stress, and π_{ijkl} is the fourth-rank piezo-optic constants tensor described for each material. With both Eq. (2.16) and (2.17), the indicatrix tensor B_{ij} can be calculated when certain stress σ_{kl} is present. Then, the dielectric constant tensor ε_{ij} can be calculated using the following relation [33],

$$[\varepsilon_{ij}] = [B_{ij}]^{-1} \quad (2.18)$$

and the resulting ε_{ij} can be used for the subsequent optical simulation on the crystals. The relations in Eq. (2.16)-(2.18) hold in any coordinate system. However, it should be emphasized that the tensors in each equation must be expressed in the same coordinate when being applied. For crystal materials, due to their symmetry properties, it is often easier to describe their properties in the crystalline coordinate system, for example, the piezo-optic tensor π_{ijkl} is usually only given in the bibliography in such systems [28]. Eventually, it is convenient to describe the stress σ_{ij} with respect to the actual crystal geometry in the lab coordinates system; and for the sake of subsequent optical simulation, the dielectric constant ε_{ij} needs to be given in the lab coordinate system. To treat the coordinate systems carefully, one must firstly define two Cartesian coordinate systems $x - y - z$ and $x' - y' - z'$

representing the lab and the crystalline coordinate systems respectively, and $[a_{ij}]$ as the transformation matrix from lab to the crystalline system. Because stress is usually described in the lab system with respect to x, y, z , while the piezo-optic tensor is often given in the crystalline system with respect to x', y', z' . To apply Eq. (2.17), these two quantities must be expressed in the same coordinate system. Instead of transforming the fourth-rank piezo-optic tensor, it was chose to transform the second-rank stress tensor into the crystalline system for simplicity. Because of the symmetry property, the stress is often expressed in the abbreviated manner, according to Nye's conventions [28], as σ_n , with $n = 1, \dots, 6$. To apply the 3x3 coordinate transformation matrix, it was first re-write the abbreviated σ_n explicitly as σ_{ij} , and then use the equation below,

$$[\sigma'_{ij}] = [a_{ij}][\sigma_{ij}][a_{ij}]^T \quad (2.19)$$

to calculate the stress tensor with respect to x', y', z' , in the crystalline system. The coordinate transformation does not change the symmetry property, and the stress tensor σ'_{ij} can also be abbreviated as σ'_n according to Nye's convention. Also, because of to the symmetry property of crystals and using Nye's convention [28], the tensors in Eq. (2.17) can be abbreviated and can be rewritten in the crystalline coordinate system with respect to x', y', z' , as,

$$\Delta B'_m = \pi'_{mn} \sigma'_n \quad (2.20)$$

with $m, n = 1, \dots, 6$. In practice, the piezo-optic tensor is almost always given in the abbreviated manner as a 6x6 matrix in the crystalline system. After performing the calculation in Eq. (2.20), $\Delta B'_m$ can be rewritten in the explicit form as $\Delta B'_{ij}$.

Next, by using Eq. (2.16) the indicatrix with the influence of stress can be calculated. Due to the facts that 1) the tensor $\Delta B'_{ij}$ that is obtained from Eq. (2.20) is given in crystalline system; and 2) the free-of-stress indicatrix tensor has a simple diagonal form in the crystalline system; performing the calculation of Eq. (2.16) in crystalline system, and that gives,

$$B'_{ij} = B'_{0,ij} + \Delta B'_{ij} \quad (2.21)$$

with,

$$B'_{0,ij} = \begin{cases} (n'_i)^{-2} & \text{when } i = j \\ 0 & \text{else} \end{cases} \quad (2.22)$$

where n'_i is the principal refractive indices of the crystal. Having obtained B'_{ij} in the crystalline coordinate system, it was easy to obtain the dielectric constant tensor ϵ'_{ij} in the crystalline system, by directly inverting the matrix $[B'_{ij}]$ according to Eq. (2.18). However, since the values of $\Delta B'_{ij}$ are much smaller than those of $B'_{0,ij}$ by magnitudes, a direct matrix inversion on $[B'_{ij}]$ would cause numerical errors. To take the influence of $\Delta B'_{ij}$, which is induced by the stress, into a correct consideration, the matrix inversion was performed according to [34], as below,

$$[\epsilon'_{ij}] = [B'_{0,ij} + \Delta B'_{ij}]^{-1} \approx [B'_{0,ij}]^{-1} - \eta [B'_{0,ij}]^{-1} [\Delta B'_{ij} / \eta] [B'_{0,ij}] \quad (2.23)$$

with

$$\eta = \frac{1}{9} \sum_{i=1}^3 \sum_{j=1}^3 \Delta B'_{ij} \quad (2.24)$$

defined as the average value of the matrix elements in $[\Delta B'_{ij}]$. Finally, after applying Eq. (2.23), it was performed a coordinate transformation back to the lab system and obtain,

$$[\epsilon_{ij}] = [a_{ij}]^T [\epsilon'_{ij}] [a_{ij}] \quad (2.25)$$

as the dielectric constant tensor in the lab coordinate system. Up to this point, it is demonstrated the practically complete method to relate the stress from the soldering process and the dielectric constant tensor that determines the optical properties. This enables further analysis of the optical effects that take place in such crystals materials.

2.3.2 Laser emission

Light Amplification by Stimulated Emission of Radiation commonly referred as LASER, is the defined capacity of interaction between the radiation and mater of some materials. This interaction is normally characterized by the exchange of energy between the discrete energy states created by an atomic structure and an external source that excites those particles,

$$\Delta E = E_2 - E_1 = h\nu_{21} \quad (2.26)$$

where E is defined by two discrete energy levels (also known as E_2 convection band, and E_1 valence band); or by ν_{21} the particles' frequency needed to excite and change the energy level of the electrons, and h the Planck's constant (Fig. 2.10). The materials able to exchange between its energy levels sub-atomic particles for later creating the laser emission are usually called semiconductors. In thermal equilibrium, those materials tend to have the lower energetic levels filled with free electrons (valence bands), however at a $T > 0$ the relative population between valence and conduction bands ($\frac{N_2}{N_1}$) of energy level can be described by the Boltzmann equation as,

$$\frac{N_2}{N_1} = \exp\left(\frac{-(E_2 - E_1)}{kT}\right) \quad (2.27)$$

Laser materials as Nd:YAG crystals can describe this lasing behaviour as an energy exchange by photons absorption (external energy source as could be a pumping diode) and later by laser photon emission (relaxation or laser emission) as seen in Fig. 2.10.

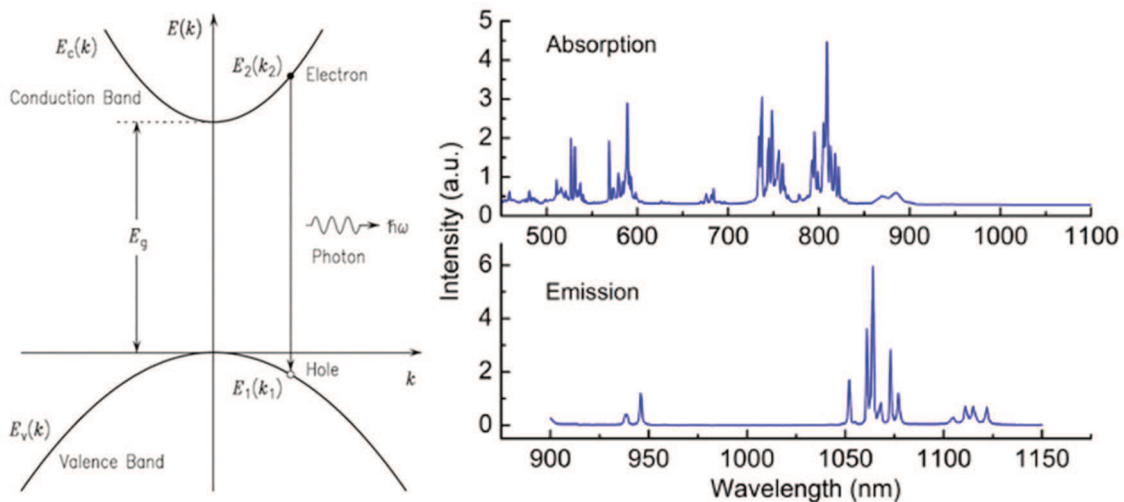


Fig. 2.10. Left, energy band structure with nearly free carrier approximation [35]. Right, Nd:YAG absorption close to 808 nm; normally created by an external pumping source. Energy emission around 1064 nm produced by particles recombination [36].

2.3.3 Birefringence effects to the laser emission

High birefringence effects close to the laser beam path inside the optical components can cause linear laser beam depolarization loss by decoupling power from p to s light polarization or vice versa. Later, this effect would remove the caused new polarization from

the original beam path creating a distortion beam shape changing an ideal Gaussian input beam $M^2=1$ to a $M^2 >1$ [37].

In the majority of published articles in the literature, this is just calculated as described in [38], and due to induced thermal stress and thermal inhomogeneities because of the diode-pumping power. In these cases, the depolarization produced by stress-induced birefringence is defined as a fraction of energy lost from p to s light polarization (or vice versa) due to light pass through the laser component, and dependent to the radius distance from the pumped area. As an example, in the literature [37], this is expressed in terms of laser output-power loss for laser systems with an intra-cavity polarizer under the effect of light depolarization, and modification of the main laser beam as,

$$\frac{I_{out}}{I_{in}} = 1 - \sin^2(2\phi)\sin^2\left(\frac{\delta}{2}\right) \quad (2.28)$$

where I , is the input and output power; ϕ , is the angle between the polarizer and the principal stress-birefringence axes; and δ , is the polarization phase shift of the emerging light. δ , can be also expressed in terms of the refractive indexes as,

$$\delta = \frac{2\pi}{\lambda}L(\Delta n_{\phi} - \Delta n_r) \quad (2.29)$$

where n_r is the radial refractive index, and Δn_{ϕ} the tangential component. This induced phase difference, will result in emerging elliptically polarization of light. These equations Eq. (2.28) and Eq. (2.29), are usually just being able to be solved for highly symmetric crystal structures, as cubic or isotropic [38]-[39].

In our study, it was implemented a more sophisticated method through the permeability matrix calculated as explained on chapter 2.3.1, and by using the electromagnetic field propagation as will be explained in the following chapter, 2.3.4. However, it was avoided the study of stress-induced birefringence consequences on output power since, in our simulations, it was assumed an input Gaussian TEM₀₀ beam, and further degenerate or higher TEM modes could be also responsible for increased output power [40]. In a real case, one should had done an iterative multi-pass analysis for which each beam's resonance would affect and generate previous and new TEM modes, and to later calculate the power for each of those; as well as the calculation of gain for the active laser crystals and/or SHG induced effects. Since the focus of the study was based on the packaging and how to calculate the soldering limits, it was decided to avoid a complete simulation analysis, focusing just in beam depolarization ratio. However, interested readers can refer to [41],[42],

where these effects are independently calculated for single component analyses with VirtualLab Fusion; showing the feasibility of the study.

For our study, the results will be shown in terms of laser beam depolarization losses, as this is the first physical produced effect, and because a full study for a laser cavity that contains more than one component would require really powerful and time consuming calculations. For that reason, it was used as a boundary conditions, a maximum depolarisation ratio and loss of 1% (maximum power loss produced after high transmission thin films applied on laser components), and a beam quality factor up to $M^2=1.2$.

2.3.4 Electromagnetic field propagation and depolarization calculation in stress-induced laser crystals

Strictly speaking, the stress distribution inside the crystal is in general inhomogeneous. Thus, it was used $\epsilon_{ij}(x, y, z)$ to fully characterize the optical properties of the material. However, in common laser examples, the beam radius is much smaller than the dimension of the crystal slab; for that reason it was decided to define the beam path centred along the z-axis, as shown in Fig. 2.11. This fact allows us to simplify the analysis by considering the inhomogeneity of $\epsilon_{ij}(z)$ only along the z-axis. Furthermore, the continuous inhomogeneity can be numerically approximated as a set of homogeneous layers [43] with different dielectric constant tensors $\epsilon_{ij}^{(p)}$, with the superscript (p) as the index of p -th layer.

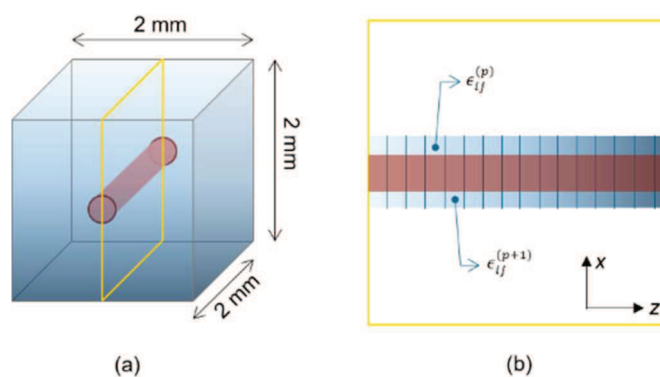


Fig. 2.11. In (a), simulated 2 mm side crystal cube with and internal laser beam represented as a red cylinder. The beam has a much smaller size than the dimension of the crystal cube. The cross-section marked within the yellow frame is shown in (b), where the inhomogeneity along z-direction is approximated as layered structures.

In the isotropic medium on the left side of the crystal where $z \leq z^{\text{in}}$, we only need the transverse field vector components E_x and E_y to characterise the electromagnetic field [44]. To perform spectrum-of-plane-wave analysis for the general field, it was first calculate the angular spectrum of the input field,

$$\tilde{\mathbf{E}}_{\perp}^{\text{in}}(\boldsymbol{\kappa}) = \begin{bmatrix} \tilde{E}_x^{\text{in}}(\boldsymbol{\kappa}) \\ \tilde{E}_y^{\text{in}}(\boldsymbol{\kappa}) \end{bmatrix} = \begin{bmatrix} \mathcal{F} E_x^{\text{in}}(\boldsymbol{\rho}) \\ \mathcal{F} E_y^{\text{in}}(\boldsymbol{\rho}) \end{bmatrix} \quad (2.30)$$

with $\boldsymbol{\kappa} = (k_x, k_y)$, $\boldsymbol{\rho} = (x, y)$, and \mathcal{F} denotes a two-dimensional (2D) Fourier transform. Then, the input field can be treated as a superposition of plane waves with different weights that are determined by the Fourier transform. Next, each plane wave is to be propagated through the layered birefringent material. This process can be expressed as,

$$\tilde{\mathbf{E}}_{\perp}^{\text{out}}(\boldsymbol{\kappa}) = \mathbf{T}(\boldsymbol{\kappa}) \tilde{\mathbf{E}}_{\perp}^{\text{in}}(\boldsymbol{\kappa}) \quad (2.31)$$

with

$$\mathbf{T}(\boldsymbol{\kappa}) = \begin{bmatrix} t_{xx}(\boldsymbol{\kappa}) & t_{xy}(\boldsymbol{\kappa}) \\ t_{yx}(\boldsymbol{\kappa}) & t_{yy}(\boldsymbol{\kappa}) \end{bmatrix} \quad (2.32)$$

as the transmission coefficients matrix. To calculate $\mathbf{T}(\boldsymbol{\kappa})$, it was used the numerically stable S-matrix method, and for that purpose, the knowledge on the plane waves in each layer is required. Based on the 4×4 -matrix formulation from Berreman [45], Landry et al. developed it to a form that is preferable for numerical calculations [46]. It was adopted their method and calculated the plane waves by solving the corresponding eigenvalue problem that is described by Eq. (2.30) in [46]. However, unlike the authors of [45] & [46], who built up the transfer matrix directly based on the eigen solutions, it was sorted out the plane waves according to their energy flowed directions, in order to prepare them for the S-matrix calculation. For this sorting, it was followed the criteria proposed by Li in Sec. 4.3 of [47]. Then the recursive S-matrix formulas can be applied and the well-developed S-matrix method is not to be repeated here [48]. Once the transmission coefficients matrix is obtained, the output angular spectrum can be obtained by using Eq. (2.30). Performing inverse Fourier transform on the output angular spectrum, it was obtained the output field as,

$$\mathbf{E}_{\perp}^{\text{out}}(\boldsymbol{\kappa}) = \begin{bmatrix} E_x^{\text{out}}(\boldsymbol{\kappa}) \\ E_y^{\text{out}}(\boldsymbol{\kappa}) \end{bmatrix} = \begin{bmatrix} \mathcal{F}^{-1} E_x^{\text{out}}(\boldsymbol{\kappa}) \\ \mathcal{F}^{-1} E_y^{\text{out}}(\boldsymbol{\kappa}) \end{bmatrix} \quad (2.33)$$

By combining Eq. (2.30), (2.31) and (2.32), it can be written the complete calculation flow from input to output field, as

$$E_{\perp}^{out}(\kappa) = \begin{bmatrix} \mathcal{F}^{-1} & \mathbf{0} \\ \mathbf{0} & \mathcal{F}^{-1} \end{bmatrix} \begin{bmatrix} t_{xx}(\kappa) & t_{xy}(\kappa) \\ t_{yx}(\kappa) & t_{yy}(\kappa) \end{bmatrix} \begin{bmatrix} \mathcal{F} & \mathbf{0} \\ \mathbf{0} & \mathcal{F} \end{bmatrix} \begin{bmatrix} E_x^{in}(\rho) \\ E_y^{in}(\rho) \end{bmatrix} \quad (2.34)$$

Following the sequence in Eq. (2.34), it was implemented a numerical algorithm in the physical optics design software VirtualLab Fusion [49], by using its programming interface.

On the other hand, in the cases at which the laser beam would be comparable to the laser crystal size, we will have to add to the effect of induced-stress birefringence, the effect of high stresses-inhomogeneity onto X and Y directions that would also affect the laser beam propagation. In those cases, instead of performing the analysis through a unidimensional beam-stress analysis as seen on Fig. 2.11, we could create an array of (n, n) beams and repeat the study with a similar analysis by going through Eq. (2.30) to (2.34).

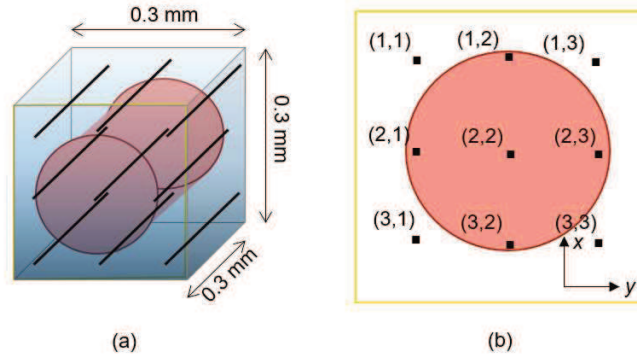


Fig. 2.12. In (a), schematic of small crystal (example 0.3 mm side cube) in comparison with laser beam (example of 200 μm diameter laser beam) with a (3,3) matrix studied cases for the light beam path propagation. In (b) X-Y plane for the (3,3) matrix example; by doing so one can take into account the different stress inhomogeneity's that will result in laser beam depolarization.

With this, one can obtain a more realistic approach for small components sizes. Although this example (Fig. 2.12) was limited to a (3,3) study, this can easily be expanded to a (n, n) analysis with VirtualLab software, depending to the user's accuracy needs.

2.3.5 Simulations softwares

In order to be able to create a simulation method capable of processing mechano-optical effects on laser cavities, a two-step analysis starting with the mechanical effects with ANSYS 17.0 to later import the stress results onto a VirtualLab Fusion software was created.

2.3.5.1 Mechanical analysis by ANSYS 17.0

ANSYS is a FEM (Finite Element Method) software, which allows to simulate physical interactions on different disciplines. Using different physics packages (as structural, vibrational, fluid dynamics, heat transfer or electromagnetics) coupled to each other one can obtain a better understanding of linear and non-linear dynamics effects on simulated processes [50]. ANSYS can import external CAD data or create its own geometries, and as well import or create its own material properties.

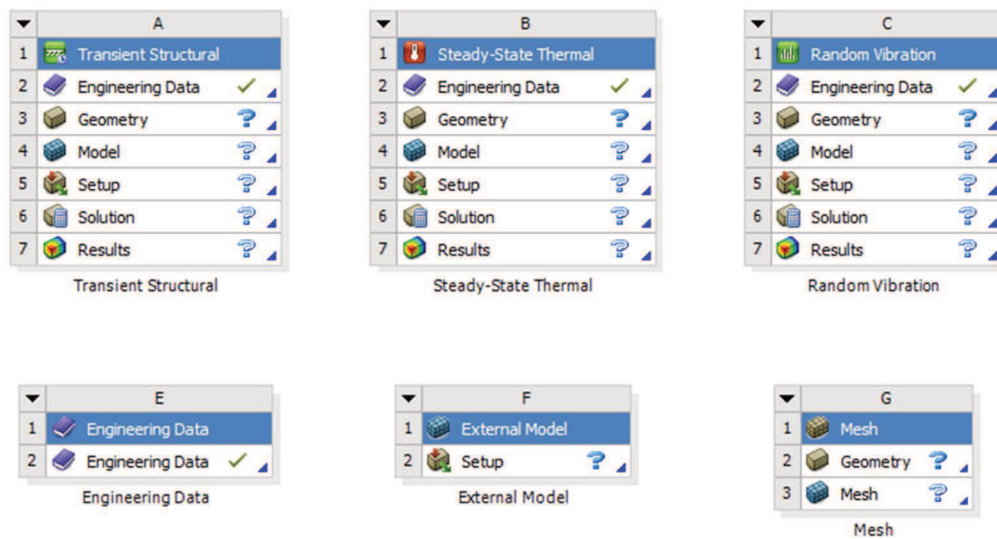


Fig. 2.13. Example of different ANSYS 17.0 packages available (first row), and example of available tools to design the models (second row).

For the study, the models were created by using ANSYS Design Modeller to later couple the designed components and created materials by using a Transient Thermal to a Transient Structural analysis. Different physics boxes and engineering tools are shown in Fig. 2.13.

2.3.5.2 Optical analysis by VirtualLab Fusion

VirtualLab Fusion physical optics software is a customizable tool that helps users to solve optical designs by using the different operation tool boxes [49]. Starting from a ray tracing to investigate standard geometric optics system performances, passing through geometric field tracing, diffractive optics, and to laser resonator designs. For the study, the laser resonator toolbox was customized in order to introduce the dielectric permeability matrix in terms of stress results, obtained with ANSYS 17.0, and by following the

mathematical approach seen on chapter 2.3.1 and 2.3.4. This helped us to obtain laser crystal output parameters in terms of laser beam depolarization.

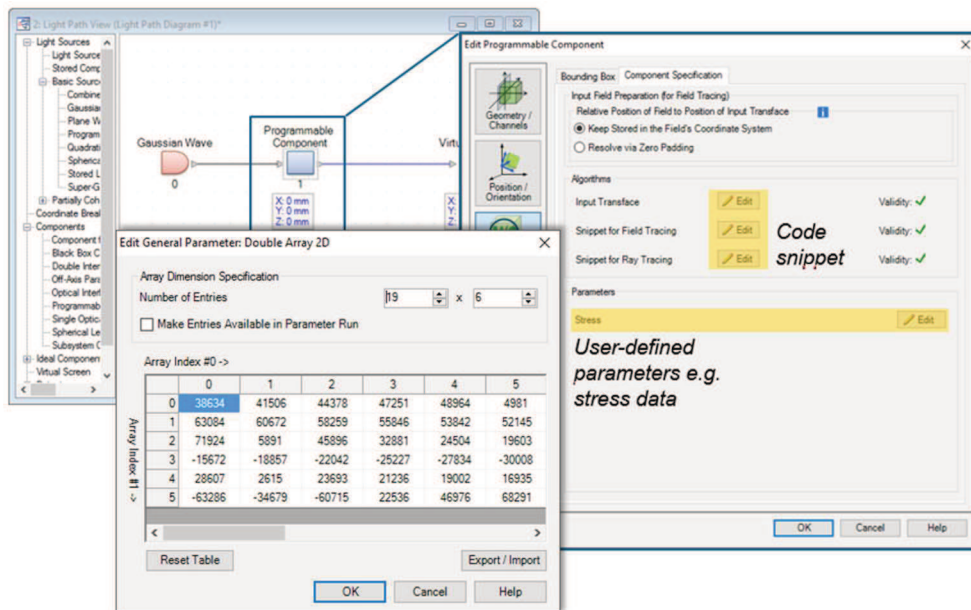


Fig. 2.14. Example of self-integrated stress module in VirtualLab. A Gaussian wave beam is introduced into and inhomogeneous body defined by the dielectric permeability matrix extracted from ANSYS.

3 Theoretical modelling and testing

3.1 Theoretical Modelling

In order to study the stress-induced birefringence produced on the laser materials due to packaging, a theoretical mechanical and later optical simulations were coupled thanks to the mathematical approaches as seen on chapter 2.3.1. Initial mechanical simulations with ANSYS 17.0 had been compared with stress results produced with a Polarimeter. Later, stress results had been converted into the dielectric matrix by following the mathematical description on chapters 2.3.1 and 2.3.4. Finally, the results were imported to VirtualLab Fusion software in order to investigate changes for laser resonator capabilities. Once the method to simulate stresses has been confirmed with real stress measurements, it was easy to re-run the simulations in order to obtain efficient packaging in terms of the components' geometry, optical performances and bonding robustness.

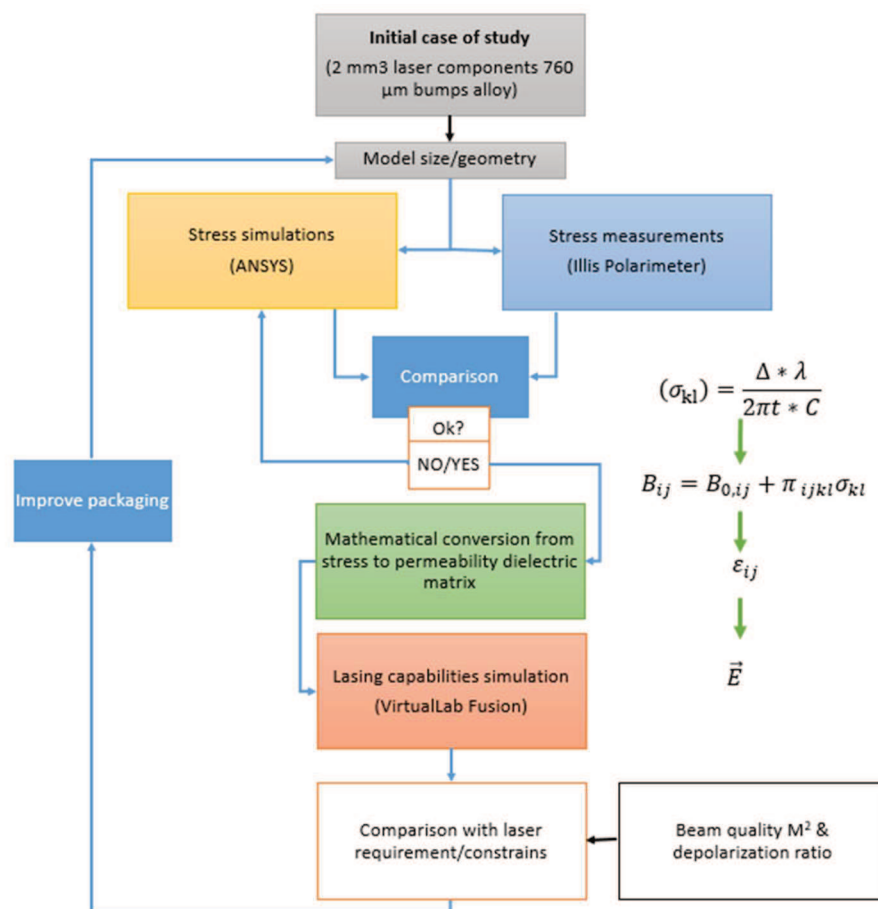


Fig. 3.1. Established step-by-step design guidelines method to simulate and verify stress-induced birefringence due to packaging. Right of the chart, the related used mathematical formulas.

3.1.1 Initial opto-mechanical stress simulations with ANSYS and VirtualLab Fusion

In order to verify our simulations method an initial common DPSSL configuration was selected. It was initially chose a plano-plano laser cavity represented by the most well-known and used laser materials in DPSSL devices; an yttrium aluminium garnet or YAG ($Y_3Al_5O_{12}$) active crystal, a second harmonic generator (SHG) beta-barium borate (β - BaB_2O_4 or BBO), and finally an output dichroic laser mirror made of fused quartz (SiO_2). The selected soft solder alloy used to join the laser components to an aluminum nitride (AIN) baseplate was SnAgCu (SAC) [31].

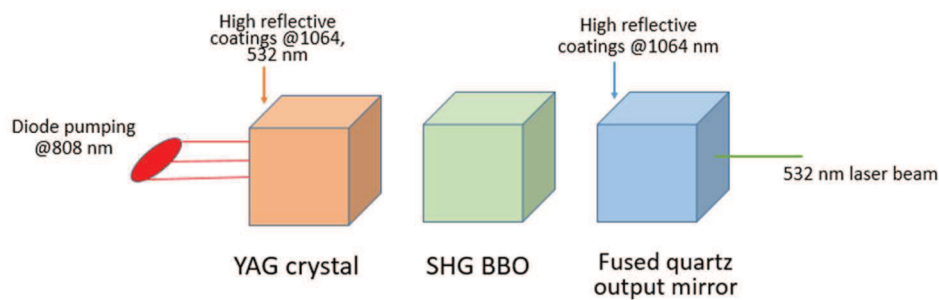


Fig. 3.2. Schematic representation of the studied DPSSL cavity. A pumping diode at 808 nm, and the plano-plano laser cavity represented by the three components; the YAG crystal, the SHG BBO and the output mirror.

The simulations were first performed with a Finite Element Method using ANSYS 17.0 software to replicate the crystal packaging procedures and calculate the induced stresses. Then, the calculated stress-induced birefringence was converted into the dielectric matrix thanks to each component's piezo-optic tensor, to be finally imported into VirtualLab Fusion software to study the packaged components' lasing capabilities.

3.1.1.1 Simulations assumptions

For the sake of simplicity, the optical components were created as independent 2 mm side cubes soldered by two 760 μ m diameter SAC alloy spheres. They were bonded onto a $5 \times 5 \times 0.25$ mm AIN baseplate with the ANSYS Design Modeler (Fig. 3.3). Later, the components' material properties were defined for each component as seen in Tables 3.1 & 3.2. In the case of the soldering alloy, instead of doing a complete phase change transition from liquid to solid that would increase the complexity of the simulations, some temperature

dependent mechanical characteristics were included in the analysis as seen in Table 3.2 and Fig.3.4.

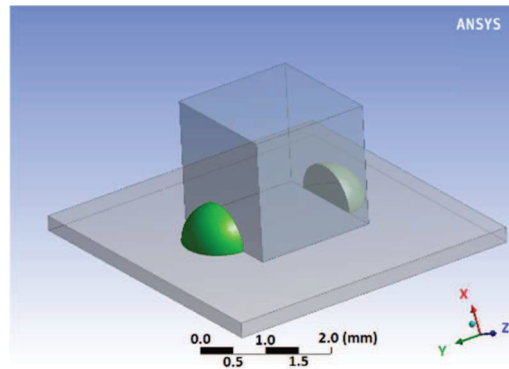


Fig. 3.3. An example of the designed geometry used for each laser component. In the case of the SHG BBO crystal, it was created by using two different coordinate systems (crystallographic and laboratory coordinates system, as explained in chapter 2.3.3). The two different coordinate systems were important to be able to define the material orthotropic characteristics (as seen in table 1), but also to define the required crystal phase matching angle of 22.8° for SHG needs [37].

Table 3.1. Main physical properties of laser materials used.

| Laser components | YAG[37] | Fused quartz | BBO[51] |
|---|------------|--------------|--|
| Density (Kg/m ³) | 4560 | 2200 | 3850 |
| Young's Modulus (Pa) | 3.1078E+11 | 7.25E+10 | 7.53E+10 (X&Y direction) 2.67E+10 (Z direction) |
| Shear Modulus | | | 7.80E+09 (XY direction) |
| Poisson's Ratio | 0.25 | 0.17 | 3.18E+10 (ZY&XZ direction) 0.186 (XY direction) |
| Thermal conductivity (W/m ^o C) | 13 | 1.38 | 0.268 (YZ&XZ direction) 0.08 (X&Y direction) |
| Specific Heat (J/Kg ^o C) | 590 | 740 | 0.8 (Z direction) 496 |

Table 3.2. Main physical properties of soldering alloy and baseplate used.

| Packaging materials | SAC305 | AIN |
|---|--------|----------|
| Density (Kg/m ³) | 7380 | 3260 |
| Young's Modulus (Pa) | Fig. 4 | 3.30E+10 |
| Poisson's Ratio | Fig. 4 | 0.24 |
| Thermal conductivity (W/m ^o C) | 58 | 160 |
| Specific Heat (J/Kg ^o C) | - | 740 |
| Enthalpy | Fig. 4 | - |

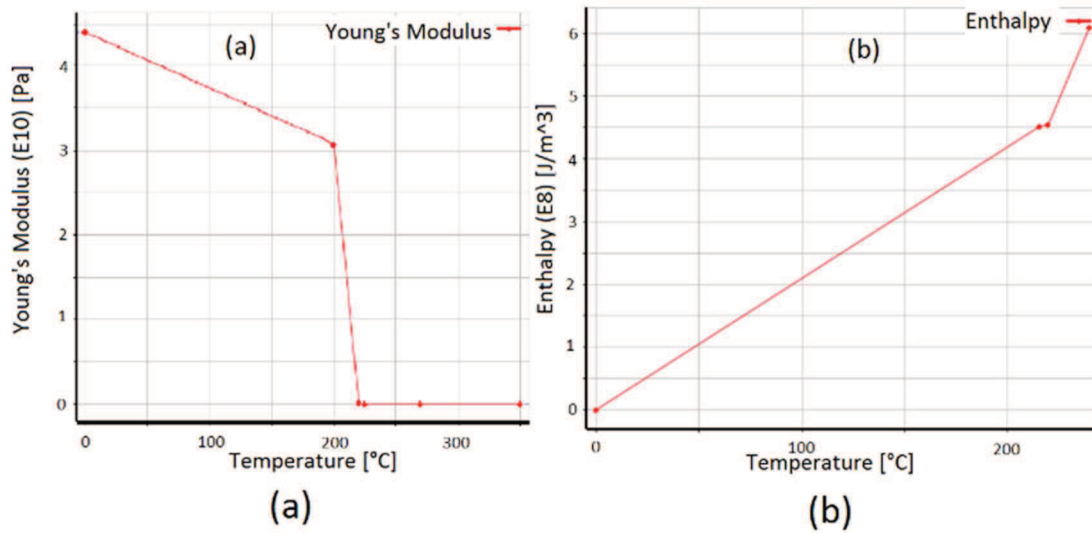


Fig. 3.4. Thermally dependent mechanical material properties. In (a) isotropic elasticity, Young's Modulus. In (b), enthalpy for the alloy phase change. The alloy thermal dependent characteristics have been extracted by experimental data from the company Setaram Instrumentation (France).

The SAC alloy enthalpy was calculated for the phase change transition by using the following equations,

$$H_S = \delta C_s (T_s - T_0) \quad (3.1)$$

$$H_L = H_S + \delta C_{TR} (T_L - T_S) \quad (3.2)$$

$$H_+ = H_L + \delta C_L (T - T_L) \quad (3.3)$$

where H_S is the enthalpy at a solid temperature, δ the SAC305 density, C_s the heat capacity at a solid temperatures, H_L the enthalpy at a liquid transition phase, C_{TR} the heat capacity at the transition phase, and H_+ and C_L the enthalpy and heat capacity at above transition phase temperatures, respectively. Later, a FEM transient thermal analysis was coupled to a transient structural analysis in ANSYS to study the cooling-down process from the SAC alloy (approximate melting temperature 217 °C) from 230 °C to 22 °C and the consequently induced stress on the components assembly.

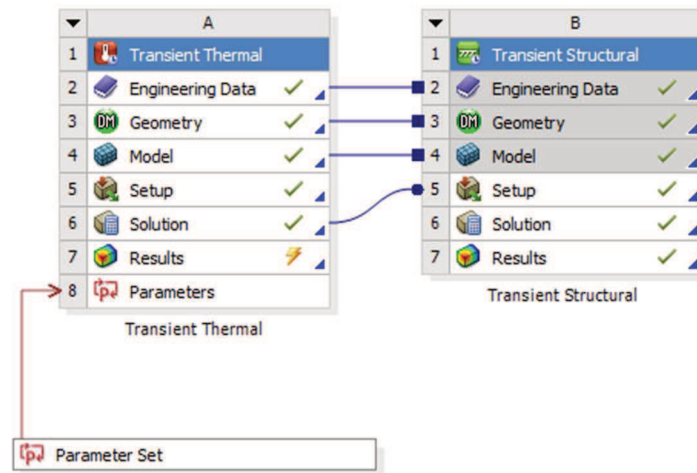


Fig. 3.5. Transient Thermal analysis coupled to a Transient Structural analysis. Parameter set helps the ANSYS user to re-run created simulations but by changing input parameter values.

Finally, with a post processing analysis, the vector principal stresses was extracted along the optical beam path inside the laser components in order to study the components birefringence and possible lasing misbehavior.

3.1.1.2 ANSYS thermo-mechanical initial results

The transient thermal analysis simulated with ANSYS 17.0 showed an almost instant cooling-down process in all the three studied materials thanks to the low-stress solderjet bumping technique as seen in Fig. 3.6.

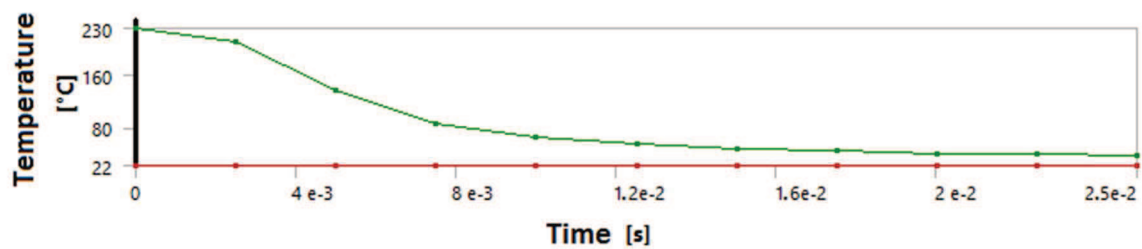


Fig. 3.6. Maximum soldering alloy phase change temperature during cooling-down process (green), and whole assembly minimum temperature (red). The almost instant cooling-down process on the BBO simulation is shown in this figure. FEM simulations carried out for YAG and fused quartz showed similar cooling-down ramps.

Later, the transient thermal analysis results were coupled sub-step by sub-step to a static structural analysis where the internal stresses were calculated:

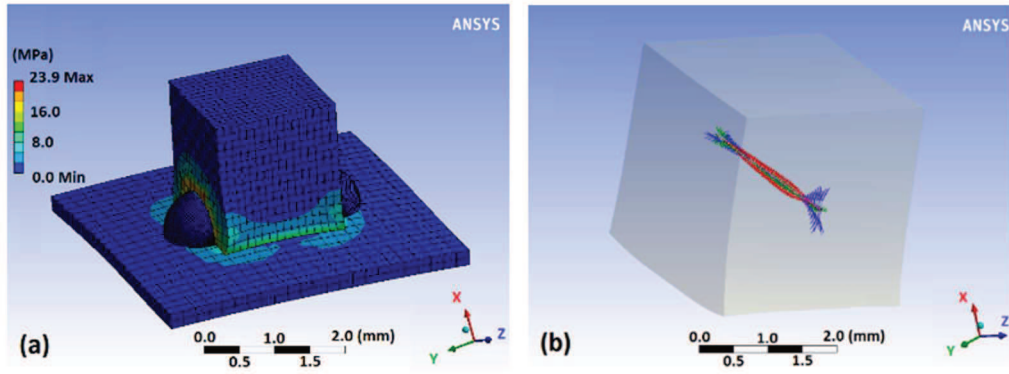


Fig. 3.7. In (a) Von-Mises stress calculated in MPa for the BBO FEM analysis. (b) Vector principal stresses calculated along the propagation direction of the laser beam in MPa (maximum, middle and minimum principal stresses in red, green and blue, respectively). Similar results were obtained for the YAG crystal and the fused quartz laser output mirror.

Then, the vector principal stresses in MPa were extracted for each of the simulations following a laser beam propagation path and transformed into changes of the components indicatrix matrix thanks to the piezo-optic tensors calculated in the laboratory system using the shown equations from Eq. (2.16) to Eq. (2.20).

3.1.1.3 Piezo-optic tensor and crystal orientation

Following the mathematical steps defined in chapter 2.3.1 and 2.3.4, and in order to obtain ε_{ij} , the induced stresses σ_{kl} calculated along the laser beam by ANSYS had been transformed from the laboratory coordinate systems, to the crystal orientation system σ'_n . In the case of the YAG crystal, usually grown by the Czochralski method (Fig. 3.8), and also cut along the [111] direction, it was used the same transformations as in Q. Lü et. al. [32], where a_{ij} from Eq. (2.19) can be expressed as,

$$[a_{ij}]^{YAG} = \frac{1}{\sqrt{6}} \begin{bmatrix} \sqrt{3} & 0 & -\sqrt{3} \\ -1 & 2 & -1 \\ \sqrt{2} & \sqrt{2} & \sqrt{2} \end{bmatrix} \quad (3.4)$$

where in this case, it was assumed that x' and y' are perpendicular to the slab faces. In the case of the BBO with crystal grown and cut along the [001] direction, the resulted stress matrix had to be just rotated 22.8° along the Y axis (Fig. 3.8) in order to accomplish the SHG phase matching. Doing so, a_{ij} from Eq. (2.19) is represented by,

$$[a_{ij}]^{BBO} = \begin{bmatrix} \cos \theta & 0 & -\sin \theta \\ 0 & 1 & 0 \\ \sin \theta & 0 & \cos \theta \end{bmatrix} \quad (3.5)$$

where $\theta = 22.8^\circ$. In the case of fused quartz, being an isotropic and amorphous material no transformation was required.

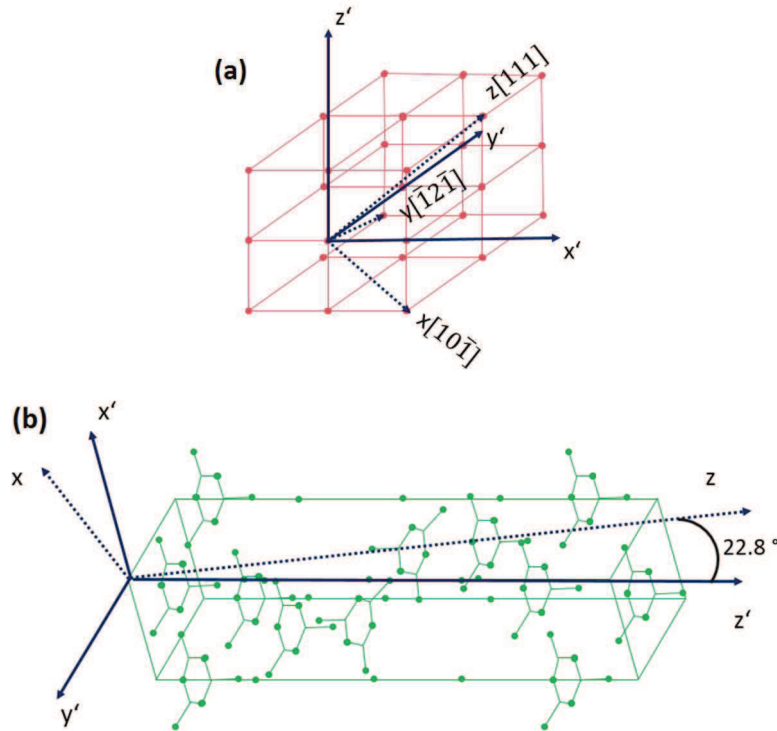


Fig. 3.8. Coordinates transformations needed to move the coordinates from the laboratory to the crystal coordinate system. In (a) crystal structure of cubic YAG. x' , y' , z' , coordinates in the crystallographic structure and x , y , z , in the laboratory system [32]. In (b), crystal structure of BBO. x' , y' , z' , coordinates in the crystallographic structure and x , y , z , in the laboratory system [52].

Once the stresses had been transformed into the crystalline coordinate system, abbreviated as σ'_n , it was just needed to know the piezo-optical constant tensors π'_{mn} to be able to apply Eq. (2.20). Being the YAG a cubic $m3m$ crystal, the BBO a trigonal $\bar{3}m$ crystal, and the fused quartz an isotropic material, and due to the crystal symmetry and Nye's convention the fourth-rank tensors expressed with 81 independent values can be reduced into a 36 independent values matrix [28], in our case we can express the piezo-optic tensors as,

$$[\pi'_{mn}]^{YAG, m3m} = \begin{bmatrix} \pi'_{11} & \pi'_{12} & \pi'_{12} & 0 & 0 & 0 \\ \pi'_{12} & \pi'_{11} & \pi'_{12} & 0 & 0 & 0 \\ \pi'_{12} & \pi'_{12} & \pi'_{11} & 0 & 0 & 0 \\ 0 & 0 & 0 & \pi'_{44} & 0 & 0 \\ 0 & 0 & 0 & 0 & \pi'_{44} & 0 \\ 0 & 0 & 0 & 0 & 0 & \pi'_{44} \end{bmatrix} \quad (3.6)$$

$$[\pi'_{mn}]^{BBO, \bar{3}m} = \begin{bmatrix} \pi'_{11} & \pi'_{12} & \pi'_{13} & \pi'_{14} & 0 & 0 \\ \pi'_{12} & \pi'_{11} & \pi'_{13} & -\pi'_{14} & 0 & 0 \\ \pi'_{31} & \pi'_{31} & \pi'_{33} & 0 & 0 & 0 \\ \pi'_{41} & -\pi'_{41} & 0 & \pi'_{44} & 0 & 0 \\ 0 & 0 & 0 & 0 & \pi'_{44} & 2\pi'_{41} \\ 0 & 0 & 0 & 0 & \pi'_{14} & \pi'_{11} - \pi'_{12} \end{bmatrix} \quad (3.7)$$

$$[\pi'_{mn}]^{Fused\ quartz, Isotropic} = \begin{bmatrix} \pi'_{11} & \pi'_{12} & \pi'_{12} & 0 & 0 & 0 \\ \pi'_{12} & \pi'_{11} & \pi'_{12} & 0 & 0 & 0 \\ \pi'_{12} & \pi'_{12} & \pi'_{11} & 0 & 0 & 0 \\ 0 & 0 & 0 & \pi'_{44} & 0 & 0 \\ 0 & 0 & 0 & 0 & \pi'_{44} & 0 \\ 0 & 0 & 0 & 0 & 0 & \pi'_{44} \end{bmatrix} \quad (3.8)$$

Table 3.3. Piezo-optic constants for the crystals in the crystallographic orientation [53] as expressed in Eq. (2.20).

| | YAG | BBO | Fused quartz |
|-----------------------------------|-----------|------------|--------------|
| $\pi'_{11} (\text{m}^2/\text{N})$ | -1.21E-13 | -1.70E-12 | 2.03E-13 |
| $\pi'_{12} (\text{m}^2/\text{N})$ | 5.08E-14 | -1.35E-12 | 3.18E-12 |
| $\pi'_{13} (\text{m}^2/\text{N})$ | - | 1.75E-12 | - |
| $\pi'_{14} (\text{m}^2/\text{N})$ | - | -2.00E-12 | - |
| $\pi'_{31} (\text{m}^2/\text{N})$ | - | -1.60E-12 | - |
| $\pi'_{41} (\text{m}^2/\text{N})$ | - | -2.03E-12 | - |
| $\pi'_{33} (\text{m}^2/\text{N})$ | - | 3.7E-12 | - |
| $\pi'_{44} (\text{m}^2/\text{N})$ | -5.38E-13 | -26.30E-12 | -2.98E-12 |

Afterwards, the full indicatrix tensor with consideration of stress was calculated, according to Eq. (2.20). That requires the knowledge the free-of-stress refractive indices, as defined in Eq. (2.21). For YAG crystal, its refractive index is defined as [54],

$$n^2 = 1 + \frac{2.293\lambda^2}{\lambda^2 - 0.1095^2} + \frac{3.705\lambda^2}{\lambda^2 - 17.825^2} \quad (3.9)$$

for the BBO crystal, its ordinary and extra-ordinary refractive indices are defined as [52],

$$n_o^2 = 2.7405 + \frac{0.0184}{\lambda^2 - 0.0179} - 0.0155\lambda^2 \quad (3.10)$$

$$n_e^2 = 2.3730 + \frac{0.0128}{\lambda^2 - 0.0156} - 0.0044\lambda^2 \quad (3.11)$$

and for the fused silica [55],

$$n^2 = 1 + \frac{0.6962\lambda^2}{\lambda^2 - 0.0684^2} + \frac{0.4079\lambda^2}{\lambda^2 - 0.1162^2} + \frac{0.8975\lambda^2}{\lambda^2 - 9.896^2} \quad (3.12)$$

where λ is the wavelength given in micrometers. With all the information above, it was easy to obtain ε_{ij} , which will be used to analyze the stress induced effects on the laser beam in the next section.

3.1.1.4 FEM stress results imported in VirtualLab

In contemplation of laser crystal lasing investigation, several cases per input wavelength and crystal conditions were evaluated as described in Table 3.4.

Table 3.4. Studied laser resonator cavity produced beams and stress crystal conditions. The diode-pumping emission wavelength of 808 nm was avoided for being granted between both extreme 532 nm and 1064 nm laser cavity wavelengths.

| Laser cavity beam | Crystal condition (YAG/BBO/Fused quartz) |
|---|--|
| 1. Gaussian @1064 nm from YAG emission, 50 μm waist radius, E_y -polarization | a. Ideal case: without stress |
| | b. Real case: with actual applied stress |
| 2. Gaussian @532 nm produced by BBO SHG, 50 μm waist radius, E_x -polarization | c. Comparing case: with increased stress (10x) by design |

Starting with the YAG crystal, and E_y -polarized input Gaussian at 1064 nm in front of the crystal, the output field behind the crystal under the three different crystal conditions can be seen in Fig. 3.9.

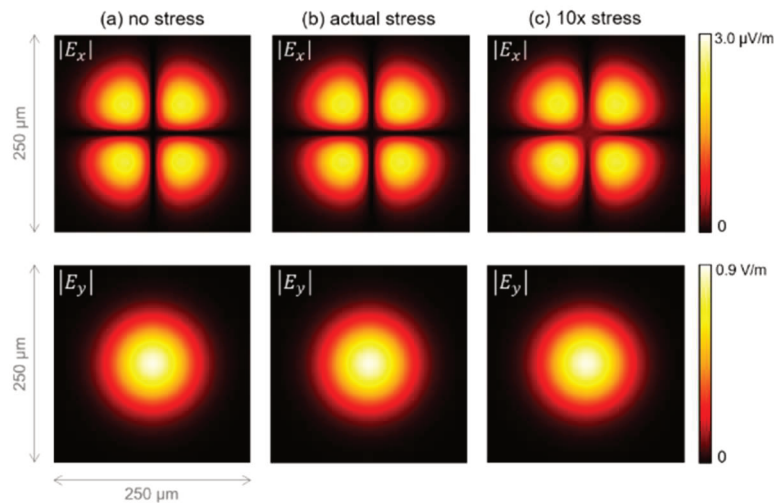


Fig. 3.9. Amplitude of the transmitted field behind the YAG crystal, with E_y -polarized Gaussian at 1064 nm as the input. Column (a) ideal case without stress; column (b) with actual solderjet bumping packaging induced stress; column (c) with 10× increased stress. Upper row corresponds to the E_x -component and lower row the E_y -component.

Although the input field in front of the YAG crystal is linearly polarized along the y -direction, due to the possible polarization crosstalk that happens when light is refracted at the crystal surface, it was obtained a non-zero $|E_x|$ in the output field, even in the case without stress-induced birefringence, as shown in column (a) of Fig. 3.9. Comparing column (b) with column (a), the actual solderjet bumping packaging induced stress shows almost no influence on the output field; while if the stress values are increased to 10 times as the actual ones by design, $|E_x|$ in column (c) shows a slight difference in its central part. Obviously, the change in the central part of $|E_x|$ is caused by the stress-induced birefringence, while its major profile remains as in column (a), which corresponds to the free-of-stress case. Switching to the case with E_x -polarized input Gaussian at 532 nm as input, it was obtained the output field as in Fig. 3.10.

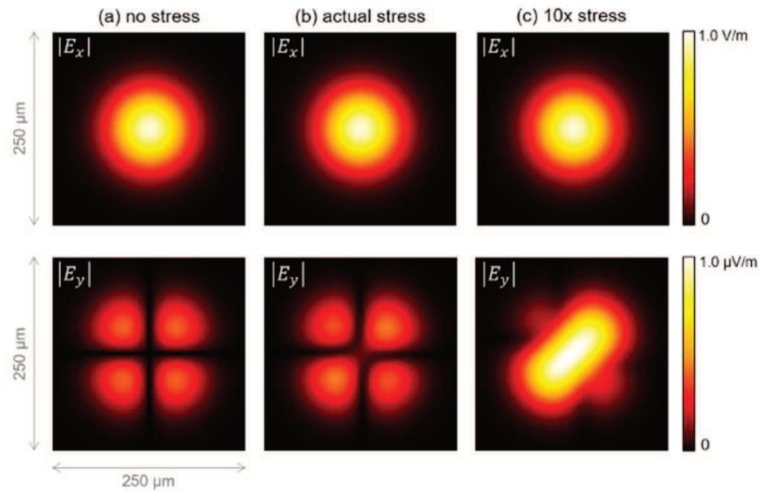


Fig. 3.10. Amplitude of the transmitted field behind the YAG crystal, with E_x -polarized Gaussian at 532 nm as the input. Column (a) ideal case without stress; column (b) with actual solderjet bumping induced stress; column (c) with 10 \times increased stress. Upper row corresponds to the E_x -component and lower row the E_y -component.

In column (a) of Fig. 3.10 in which no stress is present, one can also see a non-zero $|E_y|$, although the input field is linearly polarized along x-direction. Nevertheless, in comparison to column (a) of Fig. 3.9, the strength of polarization crosstalk for the beam @532 nm in the free-of-stress case is smaller. Therefore, the effects of stress-induced birefringence can be clearly seen in column (b) and (c). Especially in column (c), when the stress values are increased to 10 times of the actual ones, the induced birefringence is so strong that the distribution of $|E_y|$ is very different from that in column (a), which corresponds to the free-of-stress case. Following to this, in a similar manner, it was investigated the BBO crystal. Starting with the E_y -polarized input Gaussian at 1064 nm as the input. In our experiment, the BBO crystal is cut at the angle $\theta = 22.8^\circ$ and used in the $o + o \Rightarrow e$ configuration for SHG. According to the geometry sketched in Fig. 3.11(b), an ordinary wave in the BBO crystal should be linearly polarized along y-direction, while an extra-ordinary wave polarized along x-direction. Therefore, it is defined the polarizations of both beams @1064 and 532 nm as in Table. 3.4.

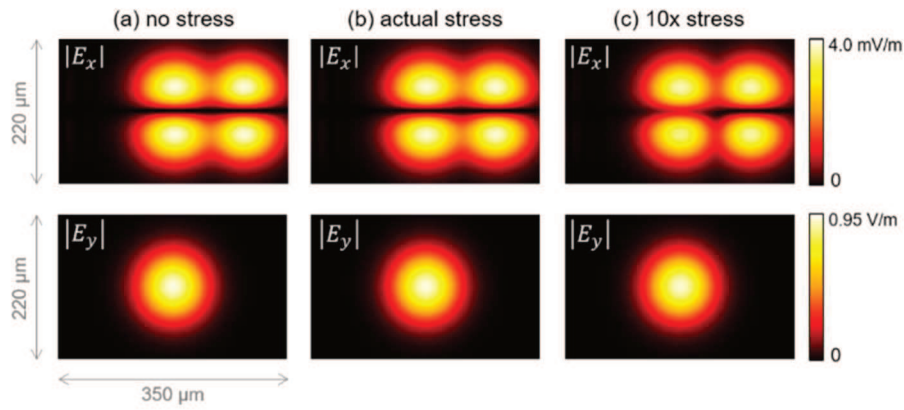


Fig. 3.11. Amplitude of the transmitted field behind the BBO crystal, with E_y -polarized Gaussian at 1064 nm as the input. Column (a) ideal case without stress; column (b) with actual stress; column (c) with 10× increased stress. The upper row corresponds to the E_x -component and lower row the E_y -component.

Unlike the case of YAG crystal, which is naturally isotropic, the BBO crystal is uniaxial anisotropic. Thus, the distribution of $|E_x|$ in Fig. 3.11 shows a lateral shift, because polarization along x-direction corresponds to the extra-ordinary wave according to the geometry described in Fig. 3.11(b). When the E_x -polarized Gaussian at 532 nm was used as the input, it is obtained the output field as seen in Fig.3.12.

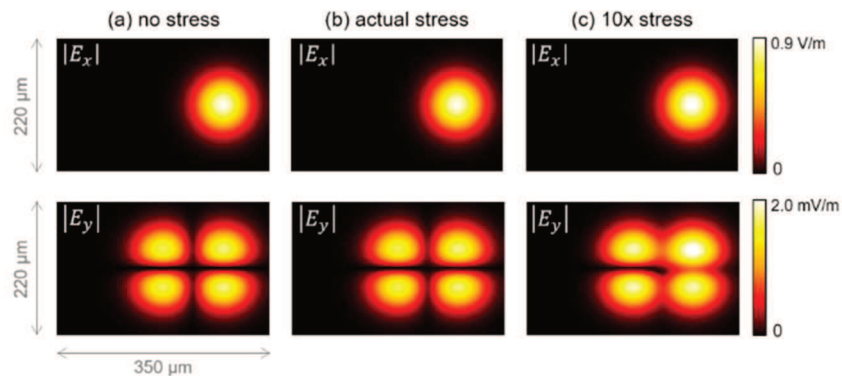


Fig. 3.12. Amplitude of the transmitted field behind the BBO crystal, with E_x -polarized Gaussian at 532 nm as the input. Column (a) ideal case without stress; column (b) with actual studied stress; column (c) with 10× increased stress. Upper row corresponds to the E_x -component and lower row the E_y -component.

When measuring the center of $|E_x|$ distribution in Fig. 3.12, it gave the values of 111 μm in our simulation, this lateral shift corresponds to a walk-off angle of 3.18° , which is in good agreement with the literature [56].

If the case of BBO (Fig. 3.11 and 3.12) is compared with that of YAG (Fig. 3.9 and 3.10), it is not hard to see that the strength of polarization crosstalk in BBO is much stronger than that in YAG, because BBO is naturally anisotropic. As a result, even when the stress values are increased by design, only slight changes are visible in column (c) in Fig. 3.11 and 3.12. For the fused quartz analysis, the results were similar to the above seen results for E_y and E_x , with respect to 532 nm and 1064 nm wavelengths for the different stress analyzed cases. The above method used to investigate stress-induced birefringence produced in this case by the solderjet bumping technique for laser crystals packaging showed an almost negligible effect on the laser crystal capabilities for the materials and geometries used. The results showed a small-induced stress effect along the laser beam direction that did not compromise the output laser beams.

3.2 Initial soldering tests

In order to prove the previously mentioned mechano-optical simulations and to study the material real cases, similar to the simulated materials had been assembled by solderjet bumping technique means. Later, the stress has been measured with an Illis GmbH polarimeter to compare and verify simulated results.

3.2.1 Material soldering parametrization

Solderjet bumping technology is a technique able to assemble optical components through a low-stress soldering process by applying solder droplets onto brittle materials that have previously been metallized by sputtering techniques. These materials (crystals or glasses) have normally little or no evidence of possible plastic deformation when an external strength is applied, causing internal material structure fracture. The solderjet bumping technique can adjust the input-energy produced by the IR laser reflow needed to melt the soldering alloy, to finally bond the desired component materials. Thus, the laser energy (mJ) can be adjusted by varying the laser current (A) and laser pulse (ms). In order to adjust the energy to each of the component's materials a DoE has to be carried out. For our study, it is used a Design-Expert® Software Version 10 and a Face Centred Cubic Central Composite Design [57]. Different input energies mJ (A,ms) have to be contrasted with the responses given by the different materials (damage on material and bump melted diameter). Each material will have different response to damage (brittle strength and surface quality

dependent) and melted bump diameter (heat transfer coefficient dependent), according to its thermo-mechanical properties. After assessing the correct energy for each optical material and substrate, the energies had to be cross-correlated between the optical components and base materials to obtain a correct fit. For the study, it was created DoE for BBO, YAG and FS optic materials that had to be bonded to AlN and KOVAR substrate materials, as seen on the table below. Different solder droplet bumps sizes of SAC305 were also investigated for each of the materials.

Table 3.5. Optic materials and substrate materials studied with different soldering applied sizes.

| | Materials | Bump diameter (μm) |
|----------------------------|------------------|---|
| Optic Material | YAG | 300, 400, 760 |
| | BBO | 100, 300, 400, 760 |
| | FS | 300, 400, 760 |
| Substrate materials | AlN | 300, 400, 760 |
| | KOVAR | 300, 400, 760 |

In the case of the BBO material and because it is extremely sensible to applied external forces (in our case also due to an improper polishing quality), an initial 100 μm diameter bump patches were applied (with a low bump reflow energy) on the material surfaces to work as a bond surface between these patches and the substrate where the BBO has to be bound. In the first place, this helped to protect the component's surface and, secondly, it provided a better wettability area in which higher diameter bumps, applied with higher laser reflow energy were used to bound the laser crystal to the desired substrate material without damaging the components' internal structure (Fig. 3.13).

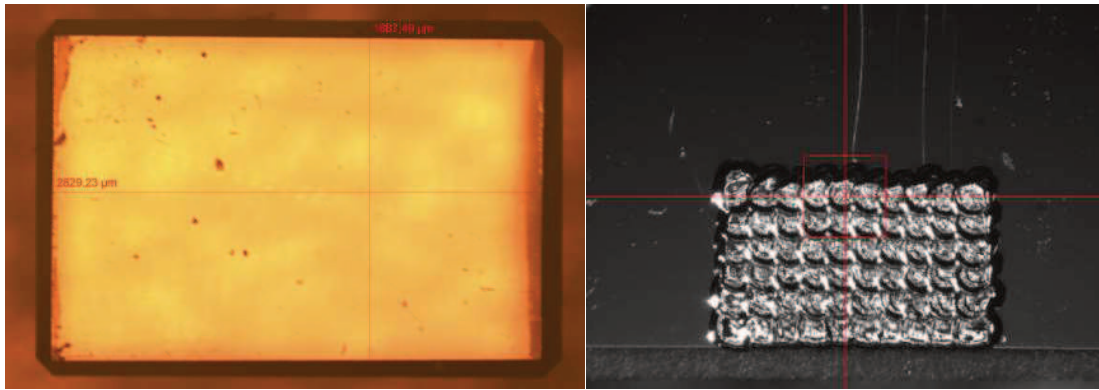


Fig. 3.13. Left, poor surface BBO quality after polishing. Right, applied 100 μm bump diameter patch made of 60 bumps after component metallization. On the second image, one can also easily see how the presence of scratches on the component could finally lead to internal superficial component cracks after soldering.

3.2.1.1 Soldering response

The material's response to different laser energy applied bumps was assessed through bump melted size on surfaces (Fig. 3.14 and 3.15), damage on optic materials (Fig. 3.16 & 3.17), and finally force needed to shear the melted bumped alloy (Fig. 3.18). The shear force was the ultimate prove of good wettability of bumps over materials, plus a good way to assess if the chosen energies for the optic materials were also in agreement with the energy needed to bond them to the substrate materials. The bump shear tests were performed with a Delvotec 5600 Pull-/Shear tester from F&S BONDTEC (Austria).

Table 3.6. Example of performed tests using different in-put factors, and with the subsequent analysed response.

| | Factor 1 | Factor 2 | Response 1 | Response 2 | Response 3 |
|-----|------------------------|-----------------------|------------|----------------------------|---------------------|
| Run | A:laser current (A) | B:pulse width (ms) | Damage | Diameter (μm) | Shear Test F(cN) |

Bump melted diameter: The desired droplet melted diameter is normally defined and approximated by Fraunhofer IOF experience by the formula,

$$1.25 * d_b < d < 1.75 * d_b \quad (3.13)$$

where d_b is the original bump diameter and d the melted bump diameter after soldering reflow [58] (Fig. 3.14).

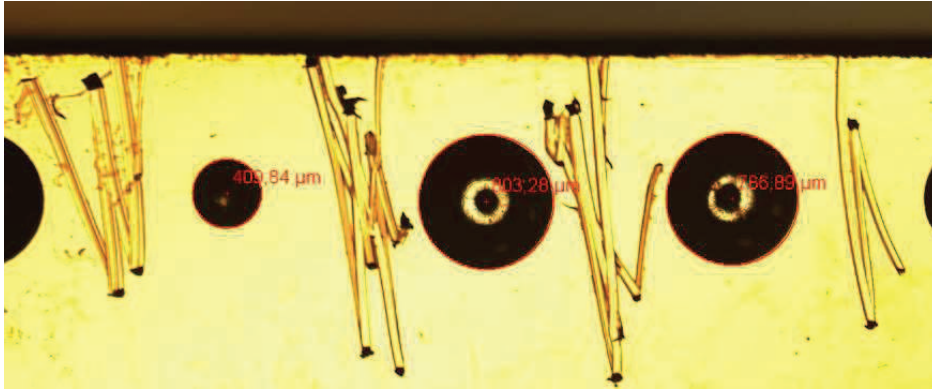


Fig. 3.14. Example of different melted diameter 400 μm bumps on a YAG sample. First bump left, with a response diameter of 409 μm applied with a laser current of 50 A, and with a pulse width of 2 ms (~ 100 mJ). Second bump middle, 803 μm diameter applied with a laser 62.5 A and 5 ms (~ 350 mJ). Third bump right, 786 μm diameter applied with a laser 62.5 A and 3.5 ms (~ 200 mJ).

With the minimum and maximum diameter considerations (Eq. (3.13)), it was easy to obtain an approximate desired input laser energy (in terms of laser pulse width and laser current), that would result onto desired melted bump diameter, represented on Fig.3.15 as the green area, located in the centre of the graphic.

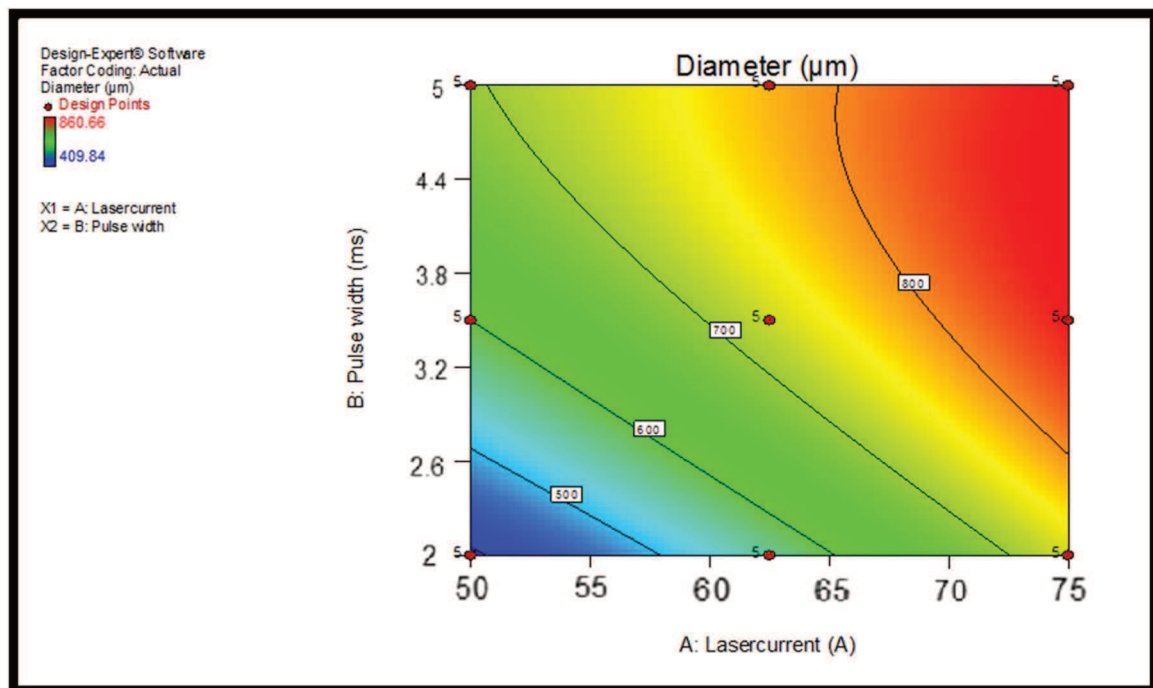


Fig. 3.15. Graphic results of input-factor energy in terms of laser current and pulse width, contrasted with bump melted diameter (bluish area $1.25 * d_b < d$, red area $d > 1.5*d_b$).

Example of results of 400 μm bumps applied on YAG.

Damage: The damage occurred due too much laser energy applied on the components surfaces. The damage was identified by four different possible responses: (1) no presence of damage; (2) material abrasion; (3) crack; (4) major crack (Fig. 3.16).

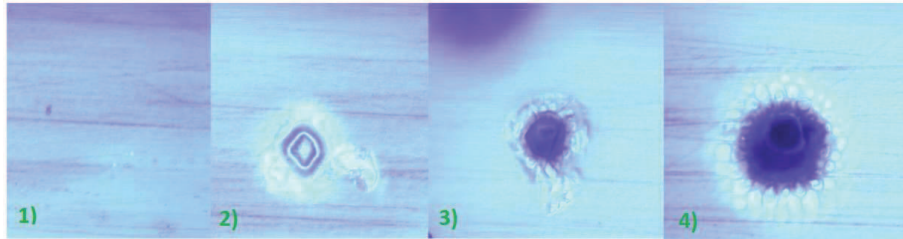


Fig. 3.16. Example of examined damage on BBO. (1) No presence of damage; (2) material abrasion; (3) crack; (4) major crack.

With this, it was find a desired response to the input laser energy factors (pulse width and laser current) in the same way as seen in Fig. 3.17 without damaging the material's inner surface.

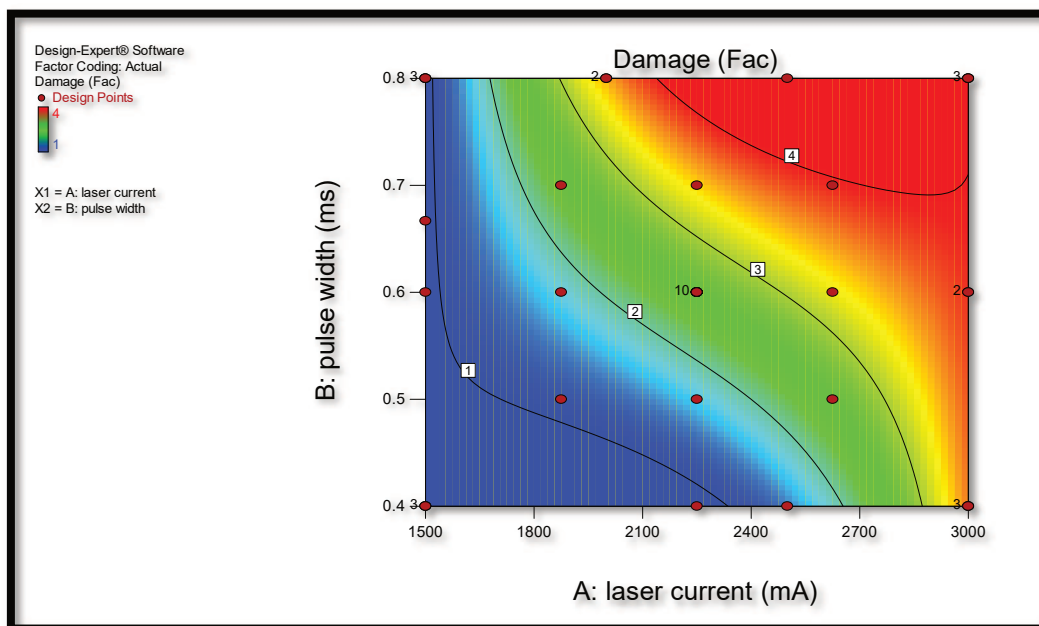


Fig. 3.17. Graphic results of input-factor energy (in terms of laser current and pulse width) contrasted with created crystal damage (bluish area no damage, red area major crack and desirable area in green). Example of results of 100 μm bumps applied on BBO.

Shear force: the needed force to shear the melted bump applied on the surfaces is empirically approximated by Fraunhofer experience [58] by,

$$F_{max} = \tau * \frac{\pi}{4} * d^2 \quad (3.14)$$

where τ is the alloy material yield strength (45 MPa for SAC305), and d the bump melted diameter. This last formula can give us an idea about the approximated desired bonding conditions and the correct alloy wettability expected for an already melted bump diameter.

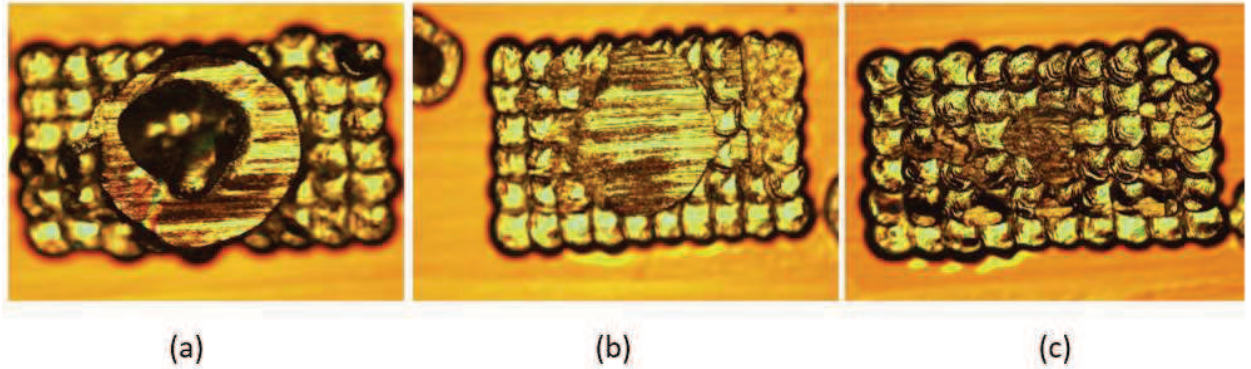


Fig. 3.18. Example of sheared 300 μm diameter SAC305 bumps over protecting BBO patches. The expected shear force using the Eq. (3.13) for 300 μm SAC bumps would be between 490 to 650 cN. (a) Too much energy (~ 210 mJ) created a slot on the melted profile, resulting as a low response to the shear tests with a result force of 277 cN. (b) Correct energy assessment (~ 150 mJ) showed a good shear force profile, and resulting shear energy force of 512 cN. (c) With insufficient energy (~ 120 mJ), the bump was totally peeled from the BBO patch; no strong bonds between applied SAC305 bumps were created. The resulting shear force to remove the applied bump on this last case was 90 cN. The shear tests were performed with a Delvotec 5600 Pull-/Shear tester from F&S BONDTEC (Austria).

Results: with the previously shown input factors and output responses, it was assessed the required laser energy application (in terms of laser pulse width and laser current), in order to obtain a correct adhesion and wettability of the bumps (SAC305 alloy) to bond the selected optical and substrate materials. The desirability graphic was the result of the correlation between good bump wetted diameter (in terms of laser reflow I(A) and Pulse(ms)) following Eq. (3.13), and the study of low damage (in terms of laser reflow I(A) and Pulse(ms)). As an example, the desirability graphic of 400 μm bumps applied on YAG is shown in Fig 3.19.

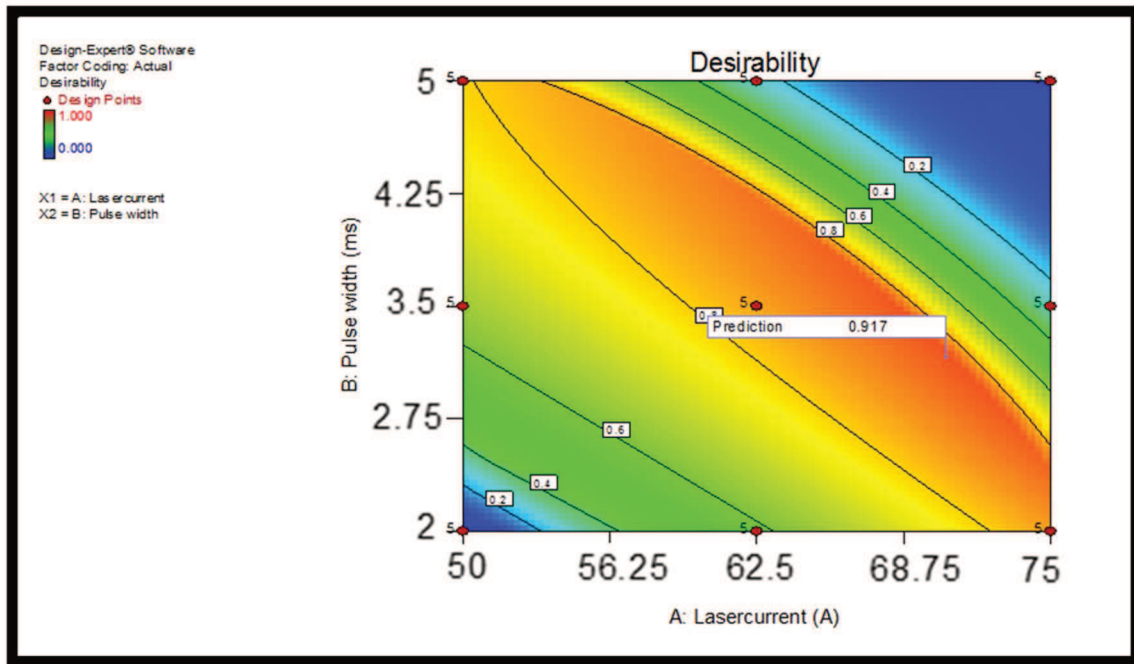


Fig. 3.19. Final YAG soldering energy desirability in terms of Laser current (A) and laser Pulse (ms) using 400 μm soldering bumps.

After obtaining the desirability graphic for each of the combinations, it was selected the best candidates by analysing the shear force results and Eq. (3.14). With this, it was possible to finally obtain a table with the desirable energy needed to bond the optical to the substrate materials for each one of the possible combinations and bump sizes as seen on Table 3.7.

Table 3.7. Finally selected used laser energy to bond optical and substrate materials with respect to the laser current and laser pulse needed to melt the soldering alloy.

| | 300 μm bump | | | 400 μm bump | | | 760 μm bump | | |
|--------------------|------------------------|------------|-------------|------------------------|------------|-------------|------------------------|------------|-------------|
| | Current (A) | Pulse (ms) | Energy (mJ) | Current (A) | Pulse (ms) | Energy (mJ) | Current (A) | Pulse (ms) | Energy (mJ) |
| BBO - AIN | 5.1 | 5.25 | 150 | 56 | 5.5 | 205 | 63 | 10 | 389 |
| BBO - KOVAR | 5.1 | 5.25 | 150 | 56 | 5.5 | 205 | 63 | 10 | 389 |
| YAG - AIN | 5.6 | 7 | 217 | 68.75 | 3.5 | 210 | 92 | 7.7 | 398 |
| YAG - KOVAR | 5.6 | 7 | 217 | 68.75 | 3.5 | 210 | 92 | 7.7 | 398 |

| | | | | | | | | | |
|---------------|-----|---|-----|----|---|-----|----|---|-----|
| FS –AIN | 5.6 | 7 | 217 | 60 | 5 | 232 | 92 | 8 | 441 |
| FS – KOVAR | 5.6 | 7 | 217 | 57 | 5 | 211 | 92 | 8 | 441 |

3.2.2 Comparison of simulated and measured stress

Once the soldering assembling energies for each of these materials were found, the next step was to verify whether simulated stresses were comparable with real created stresses. For our purpose, 2 mm four side polished cubes and 5×5×1 mm AIN baseplates, as described in chapter 3.1 were manufactured. Later, the components where metallized with Ti/Pt/Au to be finally bonded using SAC305 alloy, and by the assessed solderjet bumping energies described on the Table 3.7.

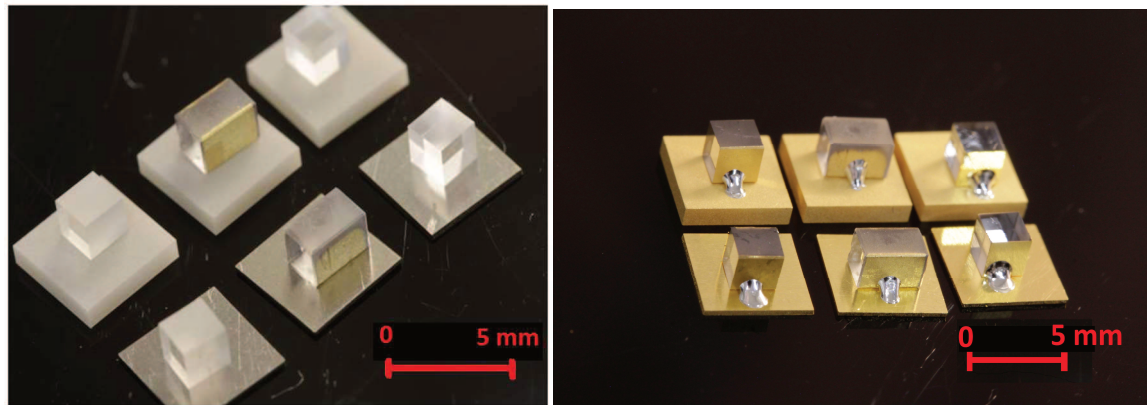


Fig. 3.20. Detail of manufactured AIN (back) and KOVAR (front) baseplates and laser components with the same configuration as shown on Fig. 3.2 (YAG-BBO-FS). Left, components before metallization and soldering processes. Right, soldered components to baseplates.

Stress simulations with ANSYS (calculated as explained on chapter 3.1.1.2) showed results with a maximum stress of 0.004 MPa and a minimum close to 0 MPa for YAG crystal due to the soldering process as seen in Fig. 3.21. For the real tests with crystal YAG, the components manufacturing processes produced much higher stresses on the crystal edges. This made impossible to asses any difference on crystal internal birefringence due to the packaging procedures. Since no real difference was found between the components before and after soldering, it was considered that solderjet bumping will not create a difference on the components laser capabilities due to the components packaging for YAG components with a cube side similar to 2 mm size.

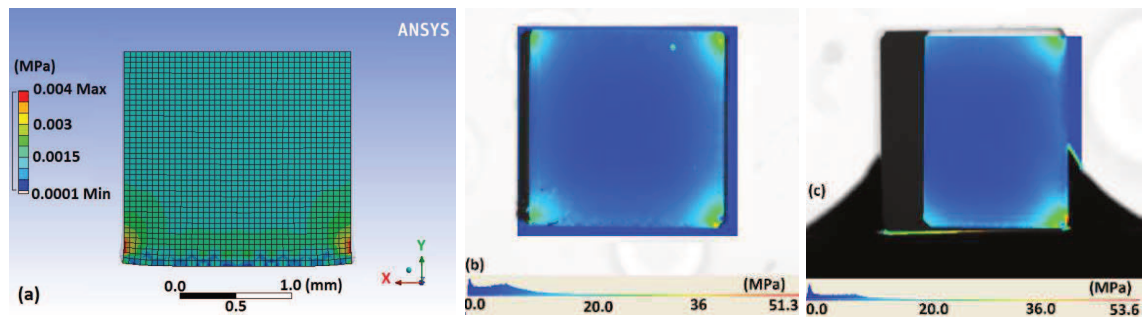


Fig. 3.21. Comparison between simulated stresses and real measured stresses after components assemble. In (a) simulated YAG. In (b) YAG stress due to manufacturing procedures (crystal cutting and polishing). In (c) similar stress as in (b) but after soldering.

In the case of the SHG-BBO, and due to the high material birefringence when cut in a 22.8° used to obtain second phase matching, was impossible to determine internal stresses by the use of a polarimeter machine. To overcome this problem, a c-cut BBO (0° in respect of the optical axis) was used to determine if our packaging technique was in agreement with our simulations. Although the results as seen in Fig. 3.22 (b) are still showing fringes produced by material birefringence (probably because cutting angle tolerances) some stress could be identified close to the soldering areas. As it can be seen in Fig. 3.22, both simulated and created stresses have just a small superficial stress, far from the beam path, and both seem to be in agreement.

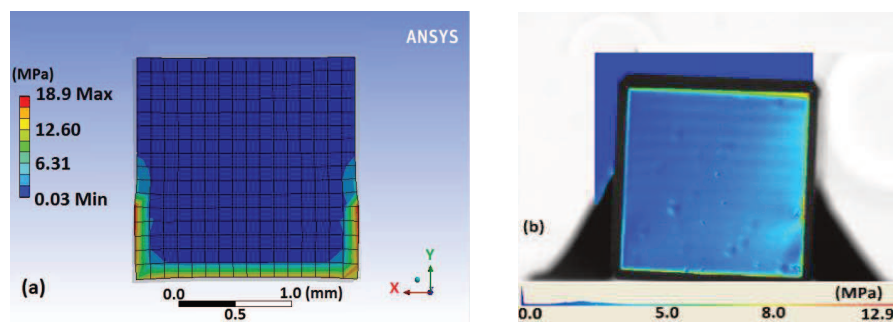


Fig. 3.22. Comparison between simulated stresses and real measured stresses after components assemble for BBO. In (a) simulated BBO. In (b) assembled by solderjet means BBO.

For the final case of the fused silica cubes, thanks to easier manufacturing processes and no internal material-birefringence problems, the results were easier to analyse. Both cases show a similar induced-stress pattern, with almost no stress influence on the middle of the crystal (approximate laser beam area), and showed a close to 1 MPa stress near the soldered areas.

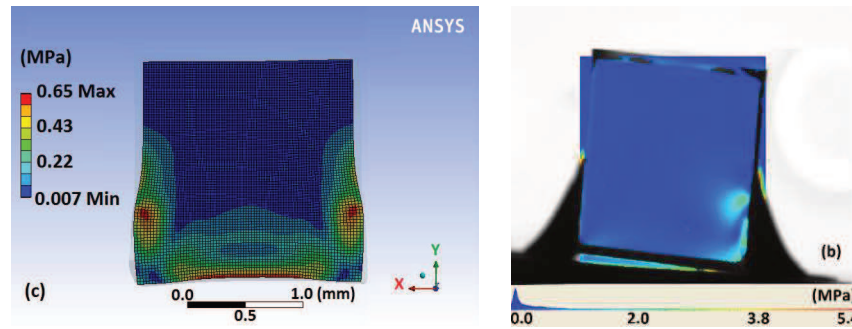


Fig. 3.23. Comparison between simulated stresses and real measured stresses after components assemble. In (a) simulated FS cubes. In (b) resulting stresses measured with a polarimeter.

After comparing the components simulations with the real assembled crystals, it is seen how despite the used simplifications (avoiding complete liquid-to-solid phase change simulation), and being working close to the minimum analysable stress by the polarimeter (0.1 MPa), both simulations and measured stresses seem to be in agreement. The centre area of the crystals seems to be almost free of stress produced by the soldering procedures (below the minimum analysable by the polarimeter <0.1 MPa), and similar stresses are being seen on the crystal's sides close to the soldering areas.

This comparison study between the produced stresses created by the bonding alloy on simulated cases by ANSYS 17.0 and by the measured stresses using a polarimeter device for the real assembled components, show that our initial simulation results are in agreement with the real applied stress. Proving also that the created method is valid for subsequent laser analysis with VirtualLab Fusion software. By proving so, it had been also demonstrated that laser cavities with such a laser crystal geometries could be assembled by the use of the solderjet bumping technique without affecting the laser emission. In the following chapter, we will try to assess the better approach to even reduce the applied stresses by varying the bump used sizes, the soldering position, and by analysing the minimum optical component size that can be bonded without affecting the subsequent laser emission.

4 Devices miniaturization

After using the theoretical model to understand and analyse stresses in laser crystal packing processes, and after comparing the simulated results with real assembled results, the following step was to assess and optimize the minimum components' possible sizes that could still guarantee low induced stresses but high robustness. For this study, FS cubes were used, since it is a common and easily to work-with material compared to the other previously mentioned laser materials, as BBO and YAG.

4.1 Soldering optimization for device miniaturization tests

To better understand the technology limits in terms of miniaturization, different combination of crystal sizes and soldering approaches were studied. The main goal was to find the limit of device miniaturization, guaranteeing low stress-induced birefringence near the laser beam path, as well as maintaining high joint robustness to guarantee device operation in harsh environmental conditions. To do so, different component size cases were studied as seen on Fig. 4.1 and described on Table 4.1.

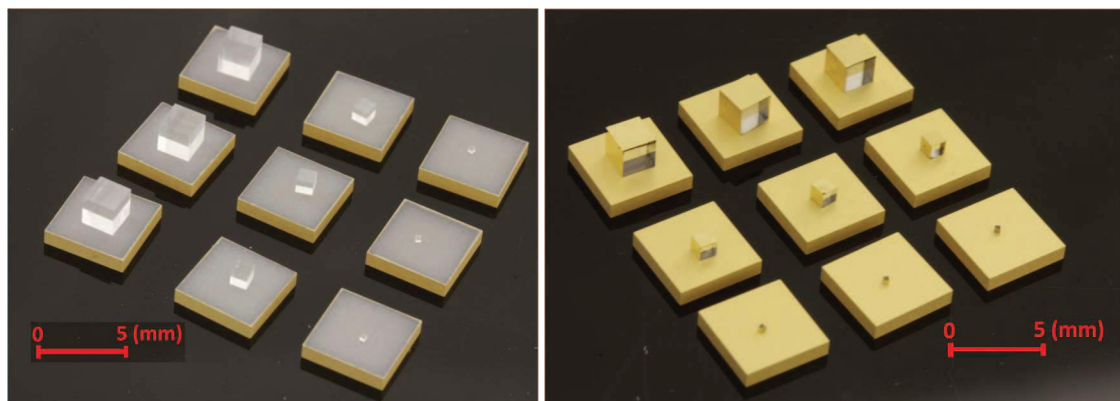


Fig. 4.1. In the picture, different sizes of manufactured FS cubes are displayed; biggest at the back row with measuring 2 mm side cubes, in the middle row, cubes manufactured measuring 1 mm side cubes and the smallest in the front row, measuring 0.3 mm side cubes. Left, cubes and AlN base-plate before metallization. Right, after the metallization of components with Ti/Pt/Au layers needed for further soldering tests.

Table 4.1. Different studied combinations of crystal and SAC305 alloy bump sizes used to solder the components. Each configuration was tried with different amount of solder bumps, depending on the crystal available area.

| Crystal size Bump size | FS 0.3 mm side cube | FS 1 mm side cube | FS 2 mm side cube |
|----------------------------|---------------------|--------------------------------------|--|
| 300 μm diameter | 2 bumps. 1x side | 2 bumps. 1x side 4 bumps. 2x side | 4 bumps. 2x side 6 bumps. 3x side |
| 400 μm diameter | 2 bumps. 1x side | 2 bumps. 1x side 4 bumps. 2x side | 2 bumps. 1x side 4 bumps. 2x side 6 bumps. 3x side |
| 760 μm diameter | 2 bumps. 1x side | 2 bumps. 1x side | 2 bumps. 1x side |

Similarly, these different configurations were simulated by ANSYS 17.0 in order to verify if the results matched the real stress soldered samples.

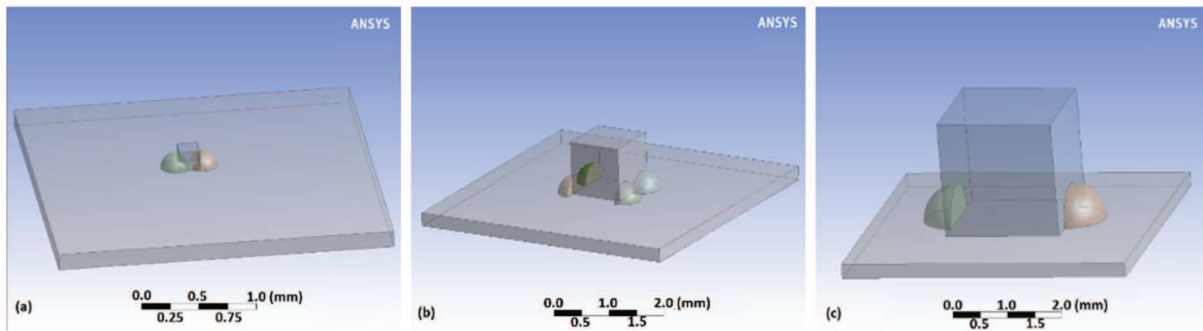


Fig. 4.2. Different simulated geometries as seen on Table 4.1. In (a) a 300 μm side cube soldered to a base plate with two soldering bumps of 300 μm diameter (before laser reflow). In (b) a 1 mm side cube soldered to a base plate with four soldering bumps of 400 μm diameter (before laser reflow). In (c) a 2 mm side cube soldered to a base plate with two soldering bumps of 700 μm diameter (before laser reflow).

4.2 Optimization soldering results

For the analytical study, it has been used ANSYS 17.0. A transient thermal simulation using the alloy enthalpy for SAC305 (as seen in chapter 3.1.1) was implemented to analyse the alloy solidification (thermal range from 230 $^{\circ}\text{C}$ to 22 $^{\circ}\text{C}$) onto the laser crystal. Later, the same simulated examples showed on Fig. 4.2 were assembled as seen in Fig 4.3, by soldering the components as described on Table 4.1; to be later measured using a polarimeter Illis GmbH [59].

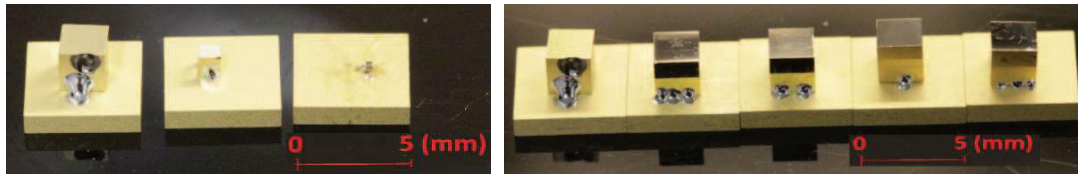


Fig. 4.3. Different sizes of manufactured and soldered FS cubes. Left image, different soldered cube sizes (2 mm, 1 mm and 0.3 mm sided cubes) soldered with different soldering alloy diameter sizes (760, 400 and 300 μm). Image onto the right, different 2 mm side cubes soldered with different amount and size of soldering bump's.

Simulated stresses following the laser beam path are shown on the Fig. 4.4, for all the described cases on Table 1. This stress-result along the laser beam path was to be later used on the VirtualLab Fusion lasing simulations.

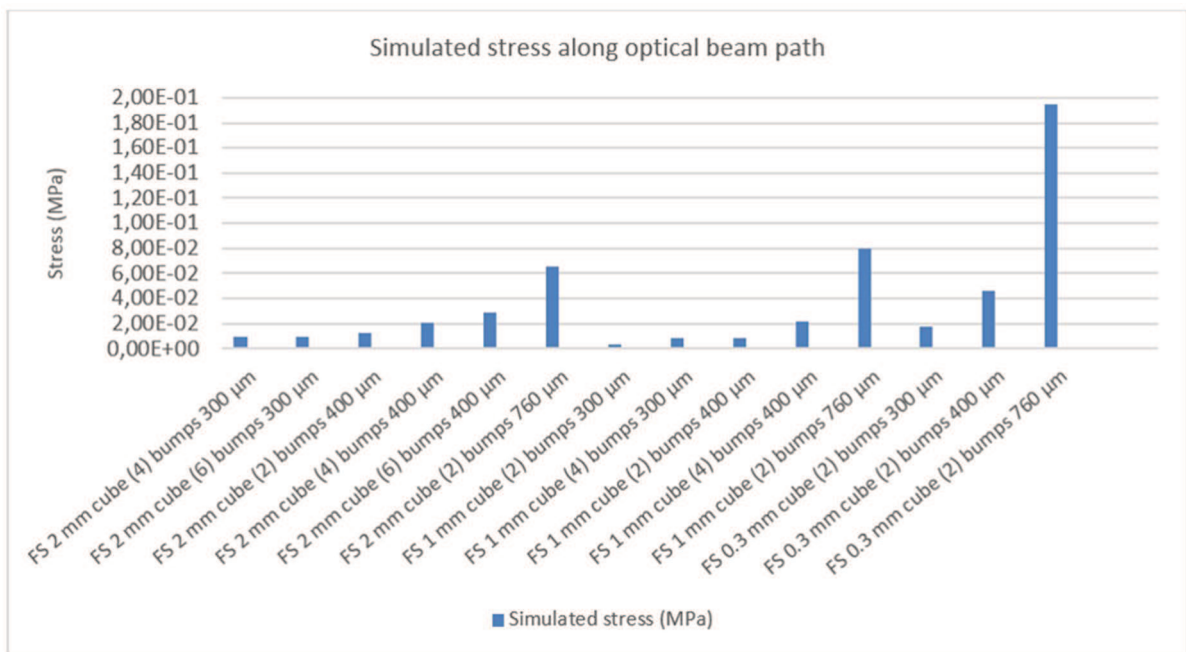


Fig. 4.4. Average stress (MPa) on the laser optical path simulated, for each component geometry as seen on Table 4.1.

On the other hand, simulated stress results (left column in Fig. 4.5) were contrasted to real measured stress results (right column in Fig. 4.5).

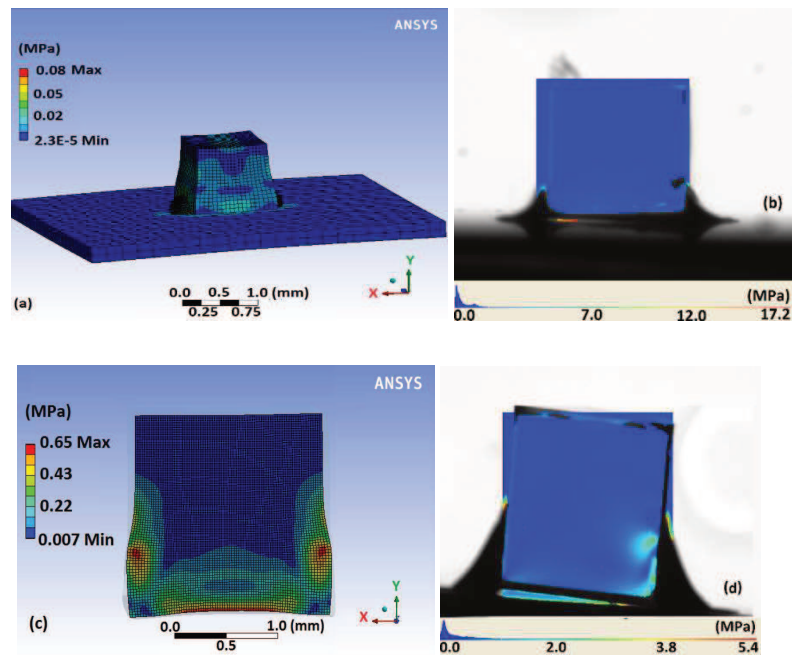


Fig. 4.5. In (a) minimum stress on optical path for a 1 mm side cube soldered with two 300 μm solderjet bumps. In (b) similar soldered case measured with a polarimeter, stress value not measurable for being below the minimum detectable value (maximum detected stress is outside the FS component) (a). In (c)&(d) higher measurable stress on a 2 mm side cube soldered with two 760 μm bumps; both simulated and real-measured cases show similar stress with almost 1 MPa close to the soldered areas.

The stress measurement for components below 1 mm size was difficult to be analysed due to the minimum size (millimetres range) and resolution (0.1 MPa) of the polarimeter device. However, after seeing how the results of the real-soldered cases with cube sizes of 2 mm and 1 mm are close to the simulated measurements, it was assumed that this would also be the case for smaller cube sizes. The induced-stress along the laser beam path in the centre of the cube was difficult to be measured in most cases, since it was below the minimum detectable stress in the polarimeter device (<0.1 MPa). However, as we could see in Fig. 4.5, the stress distribution near the soldered areas was similar for both the simulated and real soldered cases.

Later, in order to investigate the laser effects produced by the stress-induced birefringence, the results extracted from ANSYS have been analysed by VirtualLab Fusion software, where several cases for the input wavelength per fused silica component condition were evaluated as seen in Table 4.2.

Table 4.2. Studied laser produced beams and stress crystal conditions.

| Laser cavity beam | Component condition (FS cubes) |
|---|---|
| 1. Gaussian @1064 nm emission, 50 μm waist radius, E_y -polarization | a. Ideal case: without stress b. Comparing case: with (0.2x) stress by design c. Real case: with actual applied stress d. Comparing case: with increased stress (5x) by design |

Introducing an input E_y -polarized Gaussian beam at 1064 nm (as it is a common wavelength for laser cavities with Nd:YAG crystals [60]), the output laser beam was studied in terms of laser depolarization. Taking into account one of the results with higher induced stress (that has also been measured with the polarimeter device as seen in Fig. 4.5), as it is the 1 mm side FS cube soldered with 760 μm bumps, it was obtained results for the beam depolarization ratio as seen on Fig. 4.6.

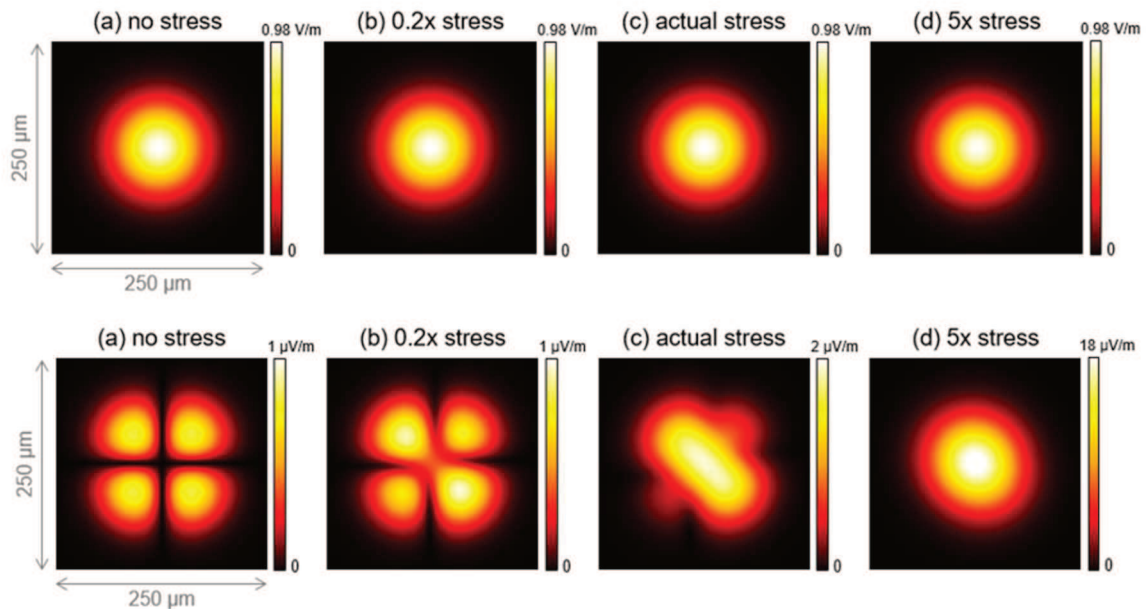


Fig. 4.6. Amplitude of the transmitted field behind the FS component, with E_y -polarized Gaussian at 1064 nm as the input. Column (a) ideal case without stress; column (b) with 0.2x applied stress (c) with actual solderjet bumping packaging induced stress; column (d) with 5x increased stress. Upper row corresponds to the E_y -component and lower row the E_x -component.

In Fig. 4.6 one can see a non-zero output field for the case without of stress; this response is due to the result of a crosstalk effect caused by reflection of light at the component surface. Comparing column cases (a) with no stress, and (b)-(c) & (d) with applied stress, one can see a beam mode change in the E_x -component; however this effect seems to introduce a maximum depolarization ratio below 0.001 % for each one of the studied cases. On the other hand, the simulations were implemented with some applied

simplifications, as it is, using a unidimensional beam stress [31] along the middle of the laser beam path; this could be effective for the cases at which the laser beam is much smaller than the beam cube size. In those cases at which the beam size is in the same order of magnitude as the laser component size one has to make sure, it is also taken into account stresses on the cube sides where higher stress is present, as seen in Fig. 4.5. In this study, and in order to avoid stress-effects produced on the sides of the 300 μm side cubes, where the stress has a higher inhomogeneous behaviour, the beam depolarization ratio was calculated for which the maximum stress was similar to 0.5 MPa; in those cases the beam depolarization ratio was about 0.1%, also insignificant for most of laser applications. In a similar way the output beam profile did not change significantly from the initial Gaussian beam, as it is possible to be seen on the first row of Fig. 4.6. The results for all the soldered and simulated cases as described in Table 4.1, showed for all the assembled components only a small-induced stress effect produced by the solderjet bumping laser-crystal packaging technique, not overpassing a beam depolarization ratio over the 1% and a beam quality factor $M^2 > 1.2$.

4.3 Push and climatic tests results

After proving how solderjet bumping created only a low induced stress on the miniaturized and bonded components, the next step was to test if those assembled different cube sizes could withstand the required high loads, as they are need it for example, in some space laser applications [61]. Considering the low mass, and the different materials of the assembled components, one can use Eq. (2.6) and the common force equation,

$$\sigma = E \Delta\alpha\Delta T \quad (2.6)$$

$$F = m * a \quad (4.1)$$

to compare in magnitude the difference between the thermal (non-operational temperatures) and the mechanical loads (acceleration, vibration ,etc.). For the case of the Exomars mission as and e.g. [25], and taking into the consideration, a mechanical acceleration of 1500 g, the mass of a 2 mm side cube of FS ($\sim 2 \cdot 10^{-5}$ gr), and the Eq. (4.1), in contrast with the non-operational thermal gradient between -60 $^{\circ}\text{C}$ to +70 $^{\circ}\text{C}$ using Eq. (2.6); one can notice that thermal loads could be several-hundred times higher than the mechanical loads. Being the thermal loads much harsh and as they are the mechanical loads, it is evaluated on the next chapters if this soldering bonds can survive this demanding requirements by performing thermal cycles. For the sake of comparison, it was contrasted

the bond strength for samples that did not passed thermal cycles in respect for those that had previously been cycled by performing push tests on them.

4.3.1 Initial not cycled push tests

For the analysis, it was contrasted a theoretical bond strength calculated taking into account melted bump covered area for the different initial bumps sizes (300 μm , 400 μm and 760 μm) by using alloy maximum yield strength (45 MPa for SAC305) [58]; comparing it later with the real force required to tear apart the soldered components. The push test on soldered components were performed with a Zwick Roell GmbH Z020. The comparison between theoretical force and measured force on soldered samples can be seen in Fig. 4.7.

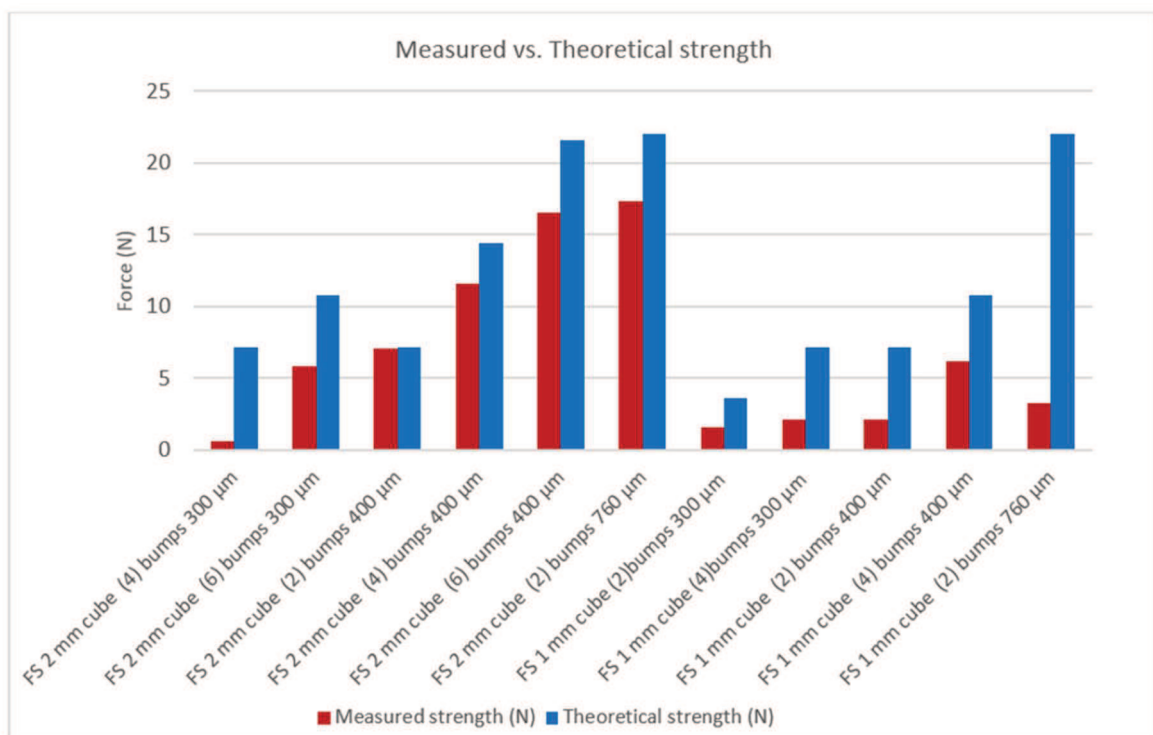


Fig. 4.7. The measurement of bonding strength between SAC305 alloy and fused silica cubes soldered on AlN baseplate using solderjet technique (red bars). This result follows similar trend with the theoretical bonding strength calculation using Eq. 2.4 (blue bars).

The results show in most of the cases a similar trend for which we can relate the amount of the used alloy with the resulting final bond strength. For those cases for which the results are not comparable (as an example the 2 mm cube (4) bumps of 300 μm and the 1mm cube (2) bumps 760 μm), the cause could be differences on final bump covered area (bump

misplacement) or even defects on components edges that led to component rupture though the FS glass.

This results, in contrast with the beam depolarization ratio results, could help users to select which would be the component size and required strength for the needed application. For the case of the 300 μm sided cubes, it was impossible to perform the test due to the available tools of the Zwick Roell GmbH Z020 to push the components, also in the range of some millimetres.

4.3.2 Climatic chamber test

In order to prove if the assembled components can withstand loads similar to the ones required for space applications, as in the case of Exomars mission [25], an environmental-thermal test was performed. It was used a climatic chamber model TCH7050 from TIRA Umweltsimulation GmbH to test the soldered samples in a eight temperature cycles between $-60\text{ }^{\circ}\text{C}$ to $+70\text{ }^{\circ}\text{C}$, with a dwell time >15 minutes and with an approximate ramp of $1\text{ }^{\circ}\text{C}/\text{min}$ (Fig. 4.8).

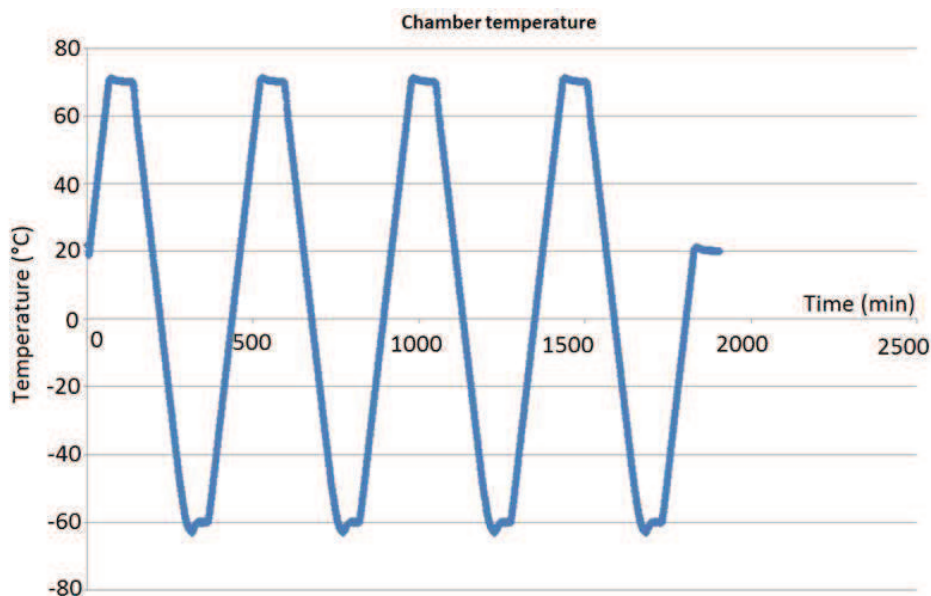


Fig. 4.8. Thermal cycles reproducing the minimum and maximum non-operational required temperatures for Exomars Mission.

Due to the different material CTE, the different thermal loads could create higher von Misses stressed on the material joints, compromising the final bond strength or even damaging internally the laser components. To assess if any change on the bond strength was

produced, further push tests in similar soldered components as shown in in Fig.4.7 were repeated after performing the thermal cycles as seen in Fig. 4.8.

4.3.3 Push test after thermal cycles

Push test for the same assembled geometries were repeated as in chapter 4.3.1 after previously mentioned thermal cycles between $-60\text{ }^{\circ}\text{C}$ to $+70\text{ }^{\circ}\text{C}$ as shown in Fig. 4.8. The results showed a chart as seen in Fig. 4.9.

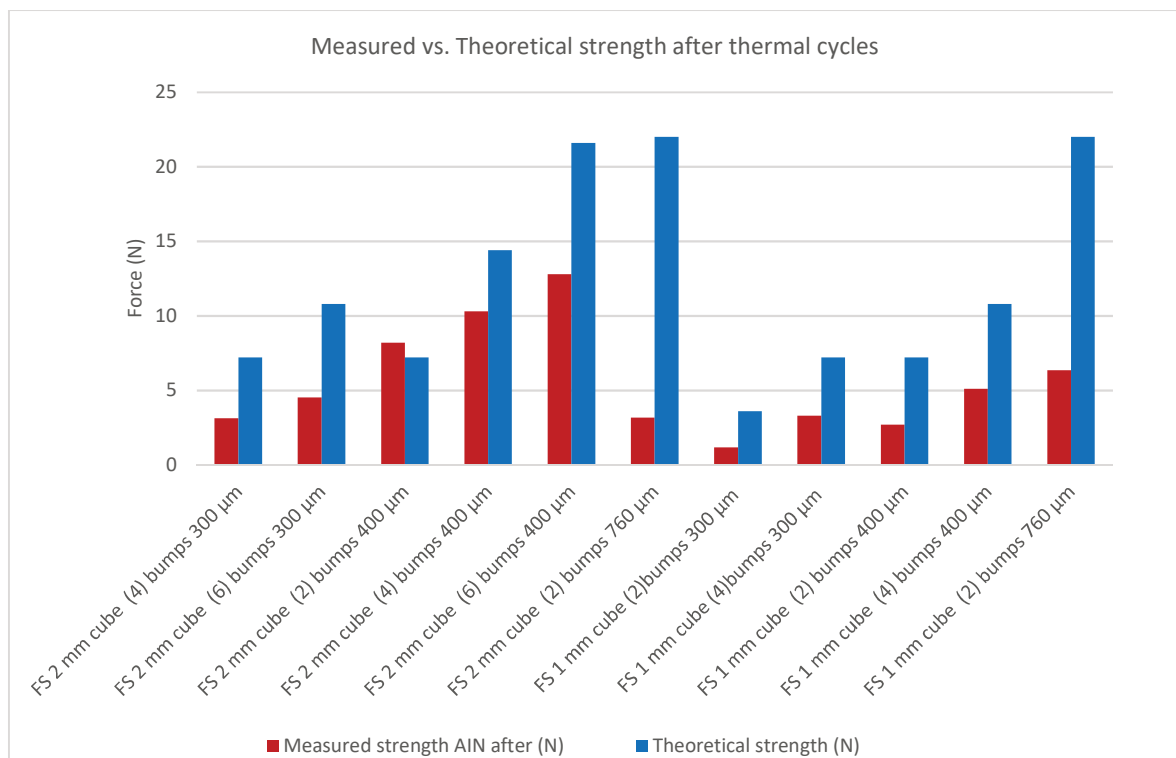


Fig. 4.9. The measurement of bonding strength between SAC305 alloy and fused silica cubes soldered on AIN baseplate using solderjet technique (red bars) after climatic cycles as shown in previous chapter 4.3.2. This result follows similar trend with the theoretical bonding strength calculation using Eq. 2.4 (blue bars).

Although a comparison between the theoretical and real experienced forces to tear apart the components could in some cases not be equivalent, Fig. 4.9 did not show neither a clear decrease of bond strength force on the assembled components. In some cases more and in some other less force was needed; as it happened also on Fig. 4.7. This effect was probably produced by slight differences on the bump placement among the components to be assembled (FS cube and AIN base), or defects on the soldered FS cube edges.

Moreover, the applied thermal cycles could also influence the generated internal component birefringence, affecting subsequently the laser emission. To check if this effect was produced, the internal stress was measured before and after thermal cycles. In most cases, the stress showed a progression as seen on Fig. 4.10.

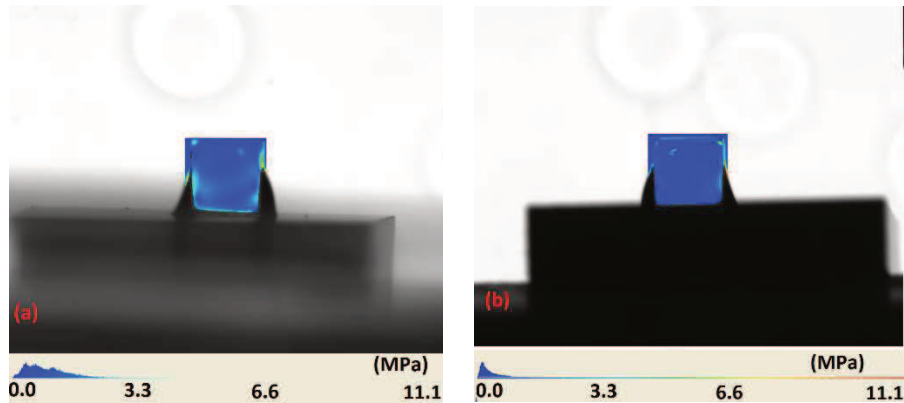


Fig. 4.10. Measured stress in MPa on a 1 mm cube sample soldered with two 400 μm bump before (a) and after (b) thermal cycles. A stress-relaxation process is visible by comparing (a) and (b).

In most of the cases, the results showed a relaxation on the component birefringence after the thermal cycles. By Fraunhofer experience [6], a stress-relaxation process is usually produced following the days and even weeks after components assemble. For that reason, it was not possible to attest if this birefringence-relaxation was a natural time-related process, or also due to the thermal cycles applied on the components. In any case, the initial birefringence produced due to the packaging technique did not strongly affect the laser emission as seen in Fig. 4.6, and even less, the lower measured internal birefringence after thermally cycling the components.

4.4 Optimization results and conclusions

A simulation method as described in [31] has been followed, and the components soldering results had been contrasted with polarimeter stress measurements in order to investigate the optimization and miniaturization of laser components packaged with solderjet bumping technique. The objective was to draw a distinction for cases at which the resulting beam depolarization and M^2 reached values higher than 1% and 1.2; respectively. Solderjet bumping technique showed much better results than the maximum expected results in all analysed cases. In the study, it was simulated and soldered components down to 300 μm

cube sizes, without strongly affecting the laser emission and with a resulting bonding strength that complies approximately with theoretical values. These results, attest solderjet bumping as a reliable technique able to assemble components down to the laser beam size (as in the case of fibers) without strongly effecting the laser beam emission.

The study has been implemented by the use of FS material for the sake of simplicity. However, it can be used for any other laser materials by adjusting the simulations with corresponding material properties [61]; easily found in [53].

Taking into account the mass of each of this FS cube sizes and considering as an example loads similar to the ones described for the Exomars European Space Agency (ESA) mission [25], each component would need to withstand a maximum of 0.3 N to resist mission mechanical loads (calculated using Eq. (4.1), and by the loads as described in [61]). However, as we have seen on Fig. 4.7 and Fig. 4.9, most of the cases could handle a forces similar to 5 N, far-over the mission demands. Thus, solderjet bumping technique seems to be a reliable technique to assemble robust miniaturized laser devices without strongly affecting the emission in terms of beam quality and depolarization ratio.

5 Case study and design guidelines

5.1 Exomars laser

After seeing the capabilities of the low-stress soldering technique called solderjet bumping and its promising qualities in terms of low-stress packaging, which can robustly bond laser components under an almost residual stress. It will be shown in this chapter, how it was used the solderjet bumping technique to assemble a DPSSL device, which required to be designed and assembled with the best possible benefits in terms of miniaturization and robustness. Following the established engineering design guidelines (Fig. 5.1) for the described methods, a miniaturized DPSSL was assembled for the Exomars ESA 2020 project, according to its optical and space mission requirements [61].

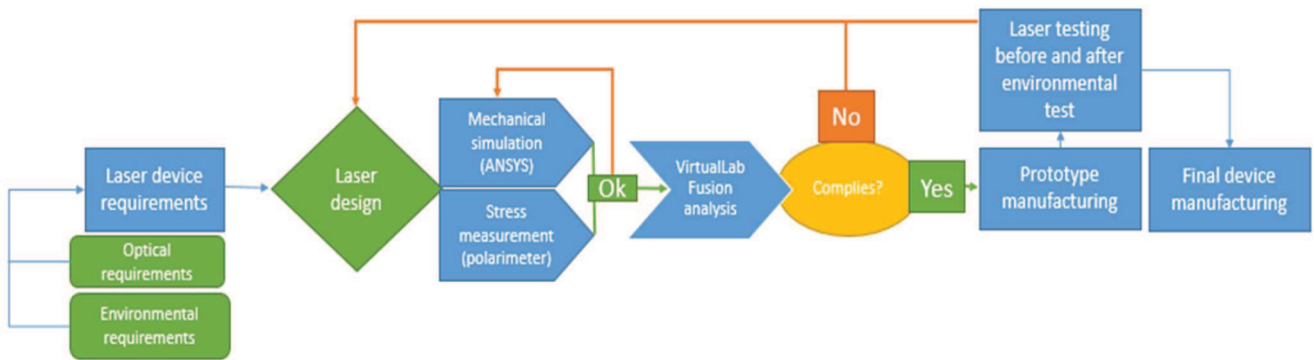


Fig. 5.1. Engineering guidelines. The figure shows the step by step established process used for this chapter dissertation, which can be applied by interested readers to assemble similar laser devices required for operating in harsh environmental conditions.

5.1.1 Laser device background

The 2020 European Space Agency Exomars mission will be the first Martian research project that comprises the combining capabilities of driving across the planet, drilling up to two meters below the surface and having a stationary surface science platform [62]. The main research purposes of the rover mission will be to search for signs of past and present life on the planet; characterize in depth water/geochemical structures; and investigate the planet subsurface to better understand the planet's crust evolution [63]. The Exomars instrument suite includes the Raman Laser Spectrometer (RLS) instrument [64] covering a spectral shift from 150-3800 cm^{-1} with a spectral resolution of 6 cm^{-1} below 2000 cm^{-1} [65].

The RLS can be divided in three main embodiments: the Instrument Control and Excitation Unit (ICEU), that includes a miniaturized and compact DPSSL that generates 532.1 nm stable green light required to excite the crushed samples and produce the Raman effect scattered light [3]; the spectrometer unit (SPU), based on single transmission holographic grating; and the internal Optical Head (iOH), that brings the laser light from the ICEU onto the Martian sample and the scattered filtered and isolated Raman signal back to the SPU (Fig. 5.2).

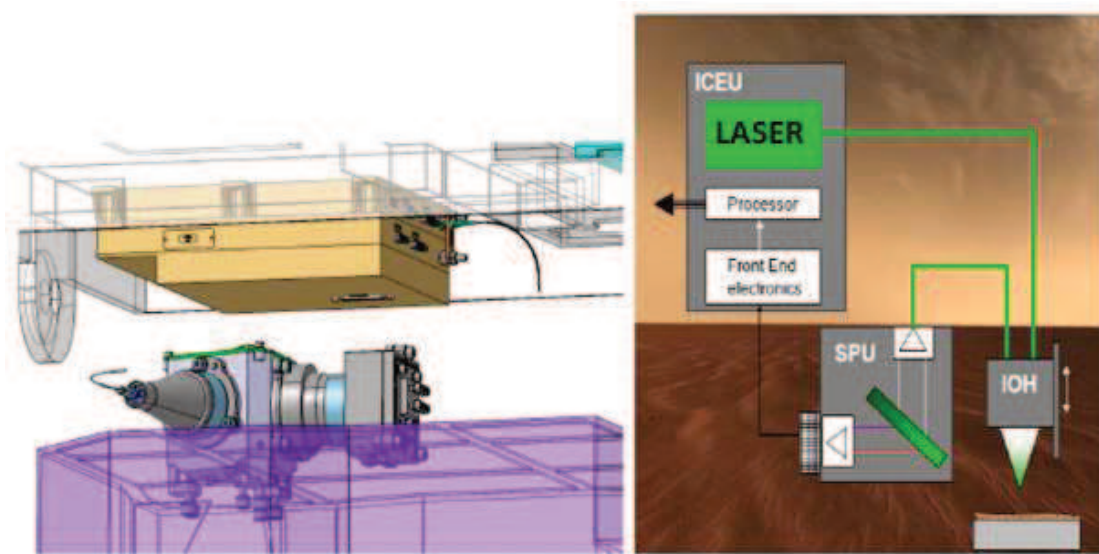


Fig. 5.2. RLS, spectrometer unit (SPU), instrument control excitation unit (ICEU) and the internal Optical Head (iOH) configuration on Exomars functional diagram of the Martian Rover [63].

The excitation source of the Raman Laser Spectrometer instrument has to be a highly stable, narrowband laser working at 532 nm [66], with the following technical requirements [67]:

- continuous emission at 532 +/-1 nm with wavelength stability $<\pm 0.05$ nm and with a Full Width at Half Maximum (FWHM) stability of <0.03 nm during 20 min time,
- optical output power range between 20-35 mW with a stability of 5%, noise level less than 1.5%,
- operational temperature from 15-45 °C.

To ensure the success of the mission, the laser source has a cold redundant design with two independent laser resonators. The design has to be implemented under additional

physical constraints, such as low weight (similar to 50 g), small size (around 7 cm³) and high efficiency (30 mW @ 532 nm with less than 2 W electrical consumption) [67]. Some of the previous requirements, or combinations of them, are not easily achieved by common DPSSL assembling techniques as adhesive or mechanical clamping methods [6].

5.1.2 Laser characteristics and requirements

The Exomars Raman Laser and the technology used for the assembly will have to pass the ESA qualification standards before the final flight model (FM) can be assembled [68]. Several solid state lasers have already been used in space missions [69]-[70]; however due to the laser characteristics and mission purposes, the requirements and performed tests on the devices must be adjusted to the specific mission needs; for the Exomars mission devices these are [25]:

- working capacity of 2000 hours with 8000 on/off cycles,
- withstand space radiations as high as an ionizing dose of 20 krad and a proton flux of $5.4 \cdot 10^{10}$ MeV*p/cm² from three different radiation sources: solar energetic particles during the journey, back-scattered and secondary radiation at Mars surface, and neutron and photon fluxes emitted from the Exomars Rover,
- thermal non-operational range between -60 °C to +70 °C and operational range between +15 °C to +45 °C,
- ultra-high cleanliness; outgassing total mass loss (TML)< 0.1% and collected volatile condensable materials (CVCM)< 0.01%,
- heavy vibration and shock (Table 5.1) similar to the conditions expected for the laser during the mission launch, cruise, landing and operational time on the planet's surface.

Table 5.1: Vibrations tests loads for the Exomars Engineering Qualification Model (EQM) lasers tests.

| | | | |
|--------|----------------|-------------|-----------------------------------|
| Sine | 5 Hz | 1 g / 1g | In-plane / out-plane |
| | 30 Hz | 20 g / 25 g | |
| | 100 Hz | 20 g / 25 g | |
| Random | 20 Hz to 40 Hz | +6 dB/OCT | In-plane / out plane during 120 s |
| | 40 to 450 Hz | 0.16 | |
| | 450 to 2000 Hz | -6 dB/OCT | |
| | grms | 11 | |
| Shock | 100 Hz | 25 g | Performed per axis |
| | 200 Hz | 1500 g | |
| | 10000 Hz | 1500 g | |

In order to validate the devices' capabilities under the environmental conditions summarized above, the assembled laser devices will have to withstand functional laser performance (to verify technical requirements), mechanical, thermal cycling, and radiation environmental tests [68].

5.1.3 Exomars' laser design

Different options have been studied in order to achieve the technical and optical requirements summarized on the previous chapter. Different laser components could guarantee better optical performances in terms of narrow wavelength emission but, for instance, lower thermal dissipation or radiation resistance. The different components tried by experimental analysis for the designed laser are summarized on the graphic below.

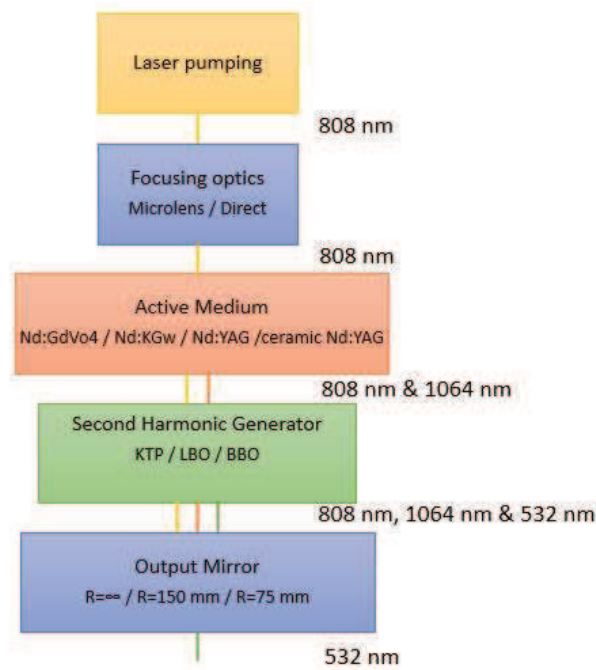


Fig. 5.3. Different laser components studied to be used for the Exomars laser and correspondent wavelength emission. The components' diagram is organized as they are mounted in the laser, following the light direction.

The finally selected components used for the Exomars resonator laser cavity that provided a functional device able to perform with the required optical performances were (Fig. 5.4): a CW (continuous-wave) q-mount diode pumping emitting at 808 nm. Later, a micro-lens (Fast axis collimator or FAC) was used to obtain a high energy density on the first millimetre of the laser active media. The active medium was finally selected to be a ceramic Nd(1%):YAG with HT808 nm and HR1064 nm (High Transmission and High Reflection; respectively), and a second side with HT1064 nm and HR532, because of a narrower linewidth emission and because it provides a better thermal conductivity [71]. Followed by a SHG crystal BBO (HT1064&532 nm coatings in both sides), because it showed a better doubling efficiency, being less sensitive to temperature changes, and being known to have higher radiation resistance levels than its competitors [72]. And a final output mirror made of fused silica and HR1064 nm and HT532 nm coatings.

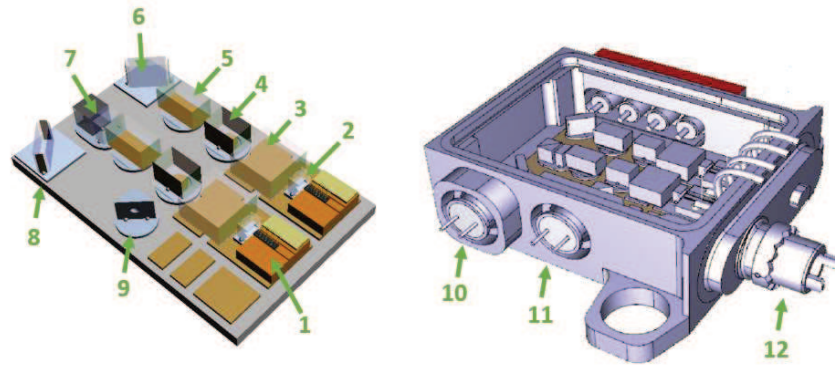


Fig. 5.4. Left, design of assembled DPSSL by soldering means. The total amount of solder alloy used to assemble the Martian laser was 0.012 g of SAC305 and 0.006 g of Au80Sn20. The optical components (emitting laser diode and laser active medium crystals) which have heat dissipation factors were assembled over copper pads bonded on an aluminium base plate (orange pads under the components). Other optical components (lenses, mirrors, and crystals) were integrated onto KOVAR pads pre-assembled on an aluminium nitride (AlN) base plate for CTE mismatch reasons (grey pads under the components). Right, laser-housing design assembled by soldering technology. (1) Pumping diodes. (2) FAC. (3) Active crystal. (4) SHG. (5) Output laser cavity mirror. (6) Folding mirror. (7) Lambda half and polarization combiner cube. (8) folding mirror in front of (10) power feedback photodiode. (9) Pinhole-mirror in front of the autofocus photodiode (11). (12) Mini-AVIM output fiber connector bringing the light to the Martian sample.

Later, other optical components were added to the laser device's design in order to bring both laser beams from both laser channels to the same output fiber and finally to the Martian samples that have to be analysed. The components needed were: a fold mirror to turn the laser beam 90°; true-zero order $\lambda/2$ (quartz), to turn the laser beam polarization, and to be able to combine both beams by using a polarizer cube; a double polarization beam splitter, to turn the laser beam once more while allowing a 5% of light pass to a power feedback control photodiode (in charge of guaranteeing a constant laser output power) [67]&[72]; and a pinhole-mirror element, used to let both coaxial beam arrive to the output fiber and to reflect the back scattered light from the sample to an autofocus photodiode in charge of adjusting the focused light onto the Martian sample.

5.2 Assembly methods

Laser manufacturers typically use polymeric adhesives or different mechanical clamping methods for their optical assemblies. In the case of the miniaturized DPSS laser for a Martian mission and due to the stringent mission's requirements, different assembly

approaches have been studied and compared. Mechanical clamping methods were avoided in this case since the mission requirements demand for a small size and low weight device, whereas mechanical clamping normally represents heavier and bulkier instruments [6]. The first approach used was based on adhesives, and after the first long-term stability problems were found, a low-stress soldering technique was assessed and finally implemented. In both cases, FEM analyses were performed; the study included static (acceleration and thermo-elastic) and dynamic (vibration and shock) loads as described on section 5.1.2.

5.2.1 Adhesive based procedures

Because of the small size of the laser resonator, its waist and the induced thermal lens, the designed laser resonator showed to be highly sensitive to components misalignments (~ 10 arcseconds). In addition to optical stability, other requirements were prescribed for the pre-selected adhesives, including low outgassing rates, withstanding temperatures from -70 °C to $+125$ °C, small shrinkage and high rigidity to resist thermal shock and harsh vibration conditions. A preliminary list of adhesives included standard low-viscosity adhesives with controlled UV curing processes (Vitalit 7041, Masterbond UV22, Loxeal UV 30-30, DELO KATIOBOND 4594, Noa88) as well as space qualified adhesives with low outgassing values, and commonly longer curing times (Epotekm 353, Masterbond EP21TDCHT-LO). Among these adhesives, two different ones were finally chose: Masterbond UV22 and Masterbond EP21TDCHT-LO (Fig. 5.5) as the best candidates for the DPSS laser. A comparison of both adhesives is shown in Table 5.2.

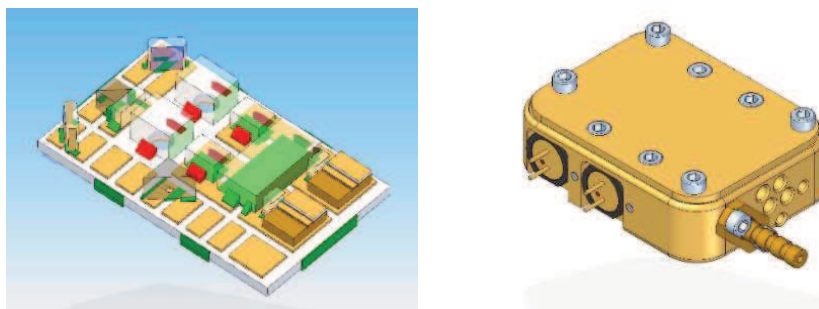


Figure 5.5. Left, design of assembled DPSSL by adhesive based procedures. The total amount of adhesive used to assemble the Martian laser was 0.031 g of UV22 (green colour) and 0.021 g of EP21TDCHT-LO (red colour). Right, design of the laser housing screwed and sealed by adhesive means.

Table 5.2. Strengths and weaknesses of the chosen adhesives for the Exomars laser assembly (data from Masterbond products datasheets).

| | Strengths | Weaknesses |
|---------------------|--|---|
| UV22 | Fast curing (5-10 seconds) Tensile strength 31 MPa | High shrinkage (<2 %) |
| EP21TDCHT-LO | Passes NASA low outgassing specifications Small shrinkage (<0.5%) | Slow curing (2-3 days) Tensile strength 17 MPa |

5.2.1.1 FEM analysis for the adhesive based assemblies

FEM simulations were carried out previous of devices manufacturing in order to verify if these prototypes could withstand Exomars mission requirements (as seen in section 5.1.2). Initial thermal analyses for non-operational mission requirements regarding temperatures were performed showing von Mises stresses of ~34.4 MPa in the adhesive patches between the optical elements and the AIN baseplate (Fig. 5.6). The stresses showed negative margins of safety (in the range of -0.1 to -0.8). Since the negative margins of safety had strong dependence on the adhesive simulation, it was considered to verify these results after the laser assembly, and during the validation thermal cycling by functional laser performance tests [73].

Modal analyses showed a first, second and third eigenfrequencies of 4418 Hz, 4867 Hz and 6791 Hz, therefore fulfilling the requirement that the assembly first eigenfrequency should be over 140 Hz [74]. The sine and random vibration frequency ranges were under the first resonance frequency, so no amplification was expected in none of the assembled parts. Quasi-static analysis on the three axes did not show irreversible deformation between the optical components and the AIN substrate. Finally, 100-1500 g shock in the z-direction was simulated; no relevant stresses that could generate irreversible deformation on the optical laser were detected.

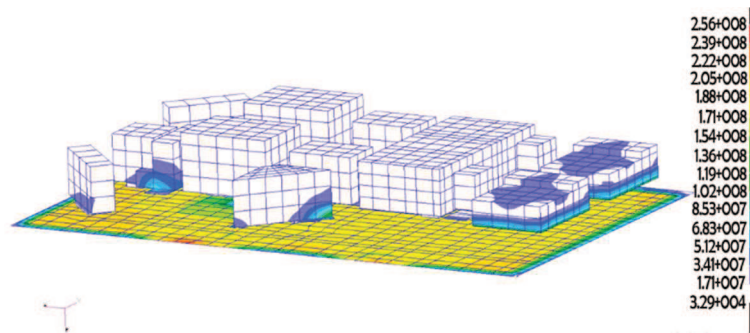


Fig. 5.6. Von Mises stresses (Pa) produced during non-operational thermal analysis between the AIN baseplate and the optical resonator laser cavity components.

5.2.2 Low-stress soldering based procedures

Solderjet bumping technology is a low-stress, long-term stable and organic-free soldering technique patented by PacTech GmbH and Fraunhofer IOF [75]. The technology is based on the application of small spherical, liquid droplets of solder alloy jetted by a pressurized nitrogen capillary. Being the solderjet bumps made with a small diameter (ranging from 40 μm to 760 μm) and melted by a very precise infrared laser pulse, just a small thermal stress is induced on the optical components during reflow and soldering. The use of metallic alloys on glass, crystal or ceramic optical components requires a polished (in order to have higher strength against thermomechanical stresses) and wettable surface on the areas to be bonded. A thin film sputtered three-layer system is used in order to avoid the presence of oxides and to guarantee the metallic adhesion on the optical components. It comprises a titanium adhesion layer, a platinum diffusion barrier and a noble gold finish that prevents oxidation and acts as a wetting surface [12]. The three layer (Ti/Pt/Au) system was applied with a DC Magnetron sputtering technique with a total thickness close to 0.5 μm (Annex 1). Solderjet bumping technology offers the possibility to work with various solders (Au80Sn20, Sn63Pb37, Ag97Si3, etc.), however, based on Fraunhofer's experience [12], the materials to be assembled, and space conformity, Au80Sn20 and Sn96.5Ag3Cu0.5 (SAC305) were the ones selected to be used on the miniaturized Martian laser (Fig. 5.4).

In optics assemblies the liquid solder-jetted bumps are usually applied at the interface between the two components to be joined, allowing for 3D arrangements; however, solderjet bumps can also be used to pre-solder a surface that later can be reflowed by other techniques. This last approach is normally used when the component

just needs a rough alignment and/or better thermal contact for heat dissipation. For the Exomars laser, both different assembling processes were used, depending on each component's alignment and heat dissipation needs:

a) **Laser resonator components assembled by Fineplacer means**

For heat dissipative elements with rough alignment needs, the most suitable process implemented was Flip Chip Assembly on a Fine Placer (as described on section 2.1.2.1). The process also required Ti/Pt/Au metallization on the components to be bonded; then, bumps made of Au80Sn20 alloy were applied by solderjet bumping technology on the optical components. Finally, by using Fine Placer technology (Fig. 5.7), both components were soldered by applying a 2-12 N force (depending on masses, wetting surfaces and materials to be soldered), and by reflowing the assembly up to the alloy melting point 280 °C. The number of applied bumps onto the optical crystals represented a homogeneous thickness of approximate 5 µm of Au80Sn20 under the components after being melt. In the case of the laser components, only the active-medium crystals were directly assembled onto the DCB by this means. However, the same technology was also implemented to preassemble the SHG and output mirror element to a sub-mount that could better fit in a conical gap (allowing for tip and tilt alignment), as is explained on the following subsection “b2”).

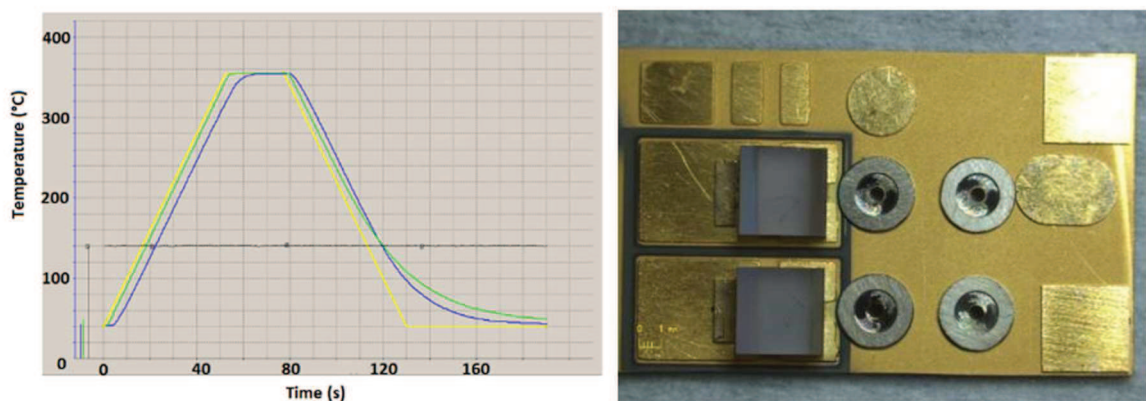


Fig. 5.7. Left, temperature reflow ramp used to solder the active-medium crystal laser component to the DCB substrate with the fine placer. Right, KOVAR Pads and laser active medium crystals soldered on the AlN substrate by a Fine Placer technology.

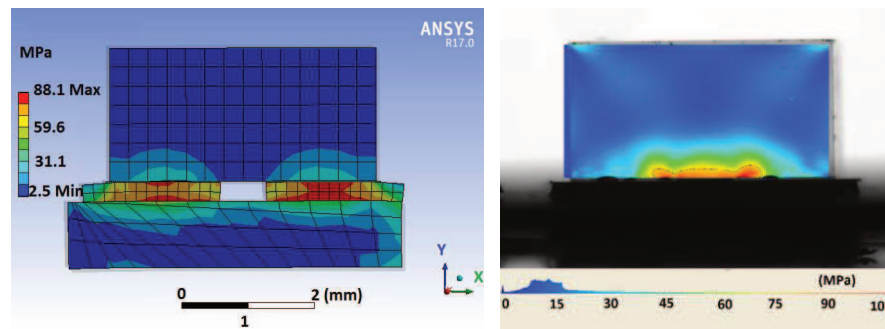


Fig. 5.8. Left, simulated stress created during active-medium crystal assemble. Right, real stress generated during active-medium crystal assemble. Both images show a maximum stress approx. 100 MPa on the crystal base, and around just 2 MPa around the laser propagation beam.

As we can see in Fig. 5.8, the use of the Fineplacer technology as a final bonding process to assemble the YAG medium to the substrate, produced a much higher internal birefringence, as in similar assembled YAG components on chapter 3.2. It was however decided to proceed with the Fineplacer, because the designed process to assemble the whole laser, required to assemble the YAG element previous to the pumping diode by the use of a higher melting alloy; in this case, Au80Sn20. On the other hand, and since the YAG was assembled prior of the laser resonator alignment, this induced stress did not affect the laser resonator configuration by overpassing the imposed requirements of maximum depolarization loss of 1%, as it will be shown in chapter 5.2.2.2.

b) Laser components directly soldered into the resonator by Solderjet means

Active laser resonator components and other optical elements with six DOF alignment needs were assembled on KOVAR pads to avoid CTE mismatch. The components were positioned above the KOVAR pads (with a minimum gap to allow 3D movement but minimizing displacement by soldering shrinkage) and pre-aligned with a vacuum gripper moved by an hexapod (F-206 Physik Instrumente GmbH) with a $\pm 2.5^\circ$ angular travel range in all 3 rotational DOF and a resolution of 0.0001° . Finally, different bumps of SAC305 alloy were applied to bond the components. A correct solderjet technology laser parametrization was performed in each of the different laser material components as explained in chapter 3.2.1 in order to apply the necessary amount of energy on the bonds without damaging the optical components but also guaranteeing enough robustness at the joints [12], [76]-[77].

In the case of the laser resonator components (the SHG and the out-put mirror), the different elements were pre-soldered on a fused-silica half-sphere by the use of fine-placer

procedures, for later being soldered into a KOVAR-ring pad as seen on Fig. 5.4. This procedure was followed in order to provide three rotational degrees of freedom and to guarantee and homogeneous an equally spaced distance between the components and the contact area where to be soldered.

b.1) Theoretical approach for soldering laser resonator components:

Laser resonator components (in this case the SHG and the output-mirror) had been pre-assembled first into a fused quartz sub-assembly platform in order to later be precisely soldered to the KOVAR pads. The purpose was to allow both components enough alignment freedom (3DOF), guaranteeing also an equal distributed spacing between the sub-mount and the KOVAR ring pad to avoid components misalignment due to soldering shrinkage. Moreover, soldering the components onto a half-sphere sub-mount helped to minimize stress-induced birefringence effects after the components alignment and their soldering onto the DCB. The better fitting spherical geometry and KOVAR ring pad used for our purpose was studied in [78], where a theoretical friction analysis was carried out.

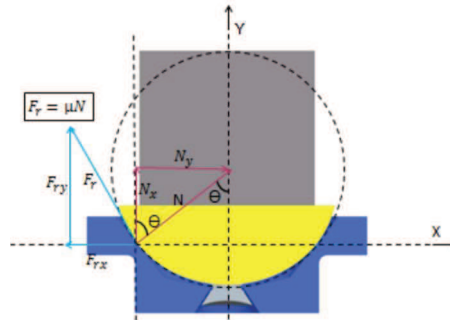


Fig. 5.9. Contact point forces distributed for a case of a ball-in-socket. In our case, a fused quartz half-sphere into a KOVAR ring pad geometry. Here, N is the normal force at contact point, F the frictional force, θ the angle contact point, and μ is the coefficient of friction between to surfaces at the joining area. [78].

In equilibrium conditions, the sum of forces produced during the alignment and soldering can be expressed as,

$$\Sigma F_x = -N \sin \theta + \mu N \cos \theta = 0 \quad (5.1)$$

$$\tan \theta = \mu \quad (5.2)$$

with the resulting frictional force,

$$F_r = \mu N = N \tan \theta \quad (5.3)$$

for which it can be infer,

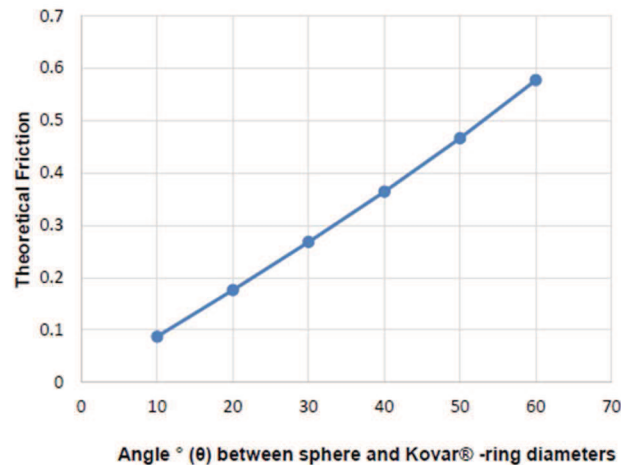


Fig. 5.10. Theoretical relation between sphere-sub-mount diameter and frictional force during soldering [78].

In addition to the above-mentioned studies, a theoretical angular misalignment study was carried out to identify the best possible geometry to minimize the laser components misalignment during soldering. This was followed under the assumption that solderjet bumping technology will always induce a small misalignment due to the kinetic energy of the bump adjoining both components, and because of the alloy shrinkage.

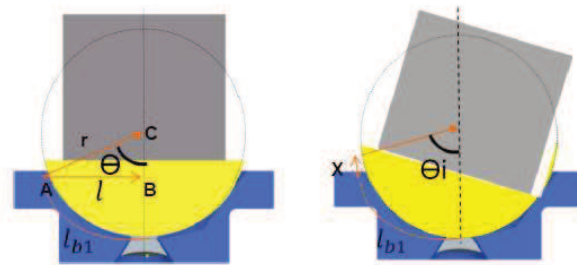


Fig. 5.11. Misalignment study depending on the sphere sub-mount radius r , and KOVAR ring pad hole radius l [78].

This movement can be explained mathematically with,

$$\theta = \sin^{-1} \left(\frac{l}{r} \right), l_{b1} = \frac{\pi r \theta}{180^\circ} \quad (5.4)$$

assuming an arbitrary component misalignment by the soldering reaction forces,

$$l_{b2} = l_{b1} + x \quad (5.5)$$

$$\theta_i = \frac{l_{b2}180^\circ}{\pi l} = \frac{(l_{b1} + x)180^\circ}{\pi l} \quad (5.6)$$

and to obtain that the difference in angle,

$$\theta_{diff} = \theta_i - \theta \quad (5.7)$$

Thus, the misalignment produced by external forces during solderjet bumping assembly on these components will have an effect on the different possible geometries as,

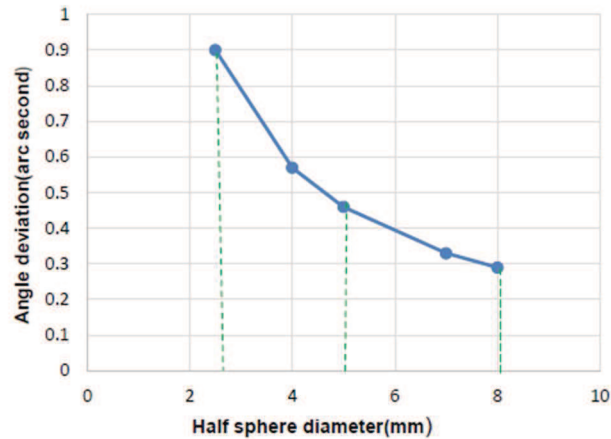


Fig. 5.12. Misalignment relation produced by an equal distributed force on different sub-mount geometries [78].

Following the above-mentioned theoretical studies, it was decided to mount the laser resonator components into 8 mm sub-mount fused silica spheres to allow them tip and tilt alignment, but guaranteeing minimal spacing between the component sub-mount and conical KOVAR-pad area where they will be mounted.

b.2) Laser resonator components with 3DOF needs soldering procedures:

b.2.1) Output mirror preassembly

The laser out-put mirror made of fused silica was preassembled to the 8 mm diameter fused silica sub-mount using the FinePlacer technology. First, the sub-mount and the mirror were metallized with Ti/Pt/Au layers. Later, a 200 μm AuSn alloy was applied to the sub-mount to later assemble both components by using the FinePlacer technology (Fig. 5.13).

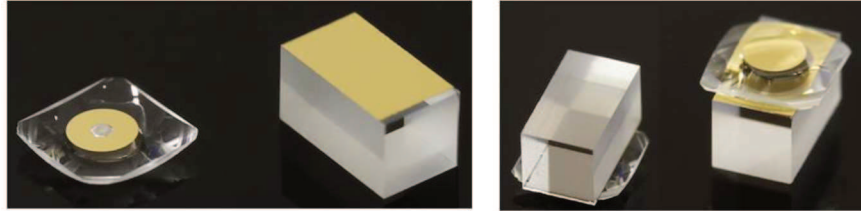


Fig. 5.13. 2x2x4 mm output mirror before and after being assembled onto an 8 mm radius FS sub-mount.

The induced-simulated and created-real stresses on the out-put mirror after assembling appears to be below 0.1 MPa across the laser beam propagation (Fig. 5.14), showing almost no influence on the laser profile beam shape nor on its depolarization effects, as was discussed on section 3.1.1.4. However, as happened in the case of the YAG, also assembled by a Fineplacer hotplate, it is seen on Fig. 5.14 how the maximum created stress (around 1.7 MPa) inside the crystal, is superior to similar components directly assembled by the use of solderjet, as seen in chapter 3.2. On the other hand, being this stress far from the laser beam path, it did not affect the final laser emission; thus the assembling procedure remained by the use of AuSn alloy and the Fineplacer technology.

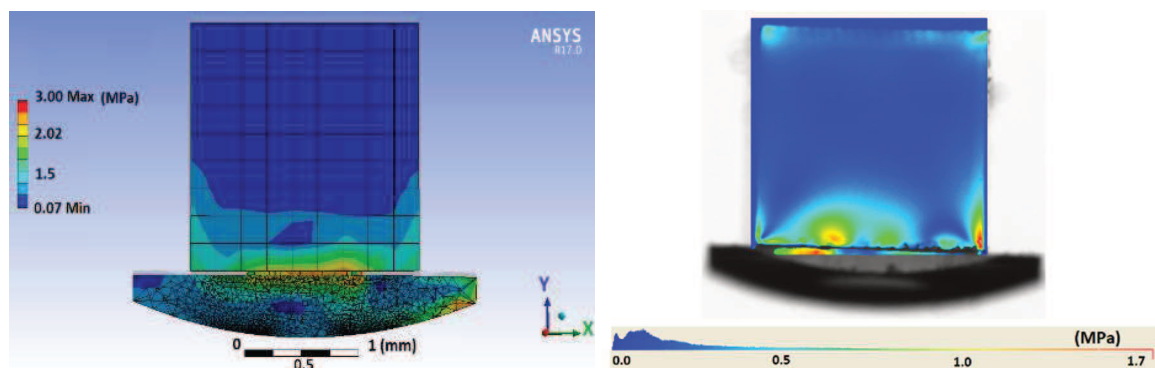


Fig. 5.14. Induced stress on soldered FS output mirrors.

b.2.2) SHG crystal preassembly

In the case of the SHG, due to the high fragility of the components, another approach was used. Instead of using FinePlacer technology, the crystal was pre-assembled to the sub-mount by the use of solderjet technology, since it induced less stress on the components to be soldered; and reduced the final internal damage on the components. In order to guarantee a robust join between both components but also to minimize the thermal damage on the crystal, an initial array of 100 μm diameter SAC305 bumps (60 bumps per side) was applied

at first on the crystal surface, to later use adjoining 300 μm SAC305 between the SHG and the fused silica sub-mount.

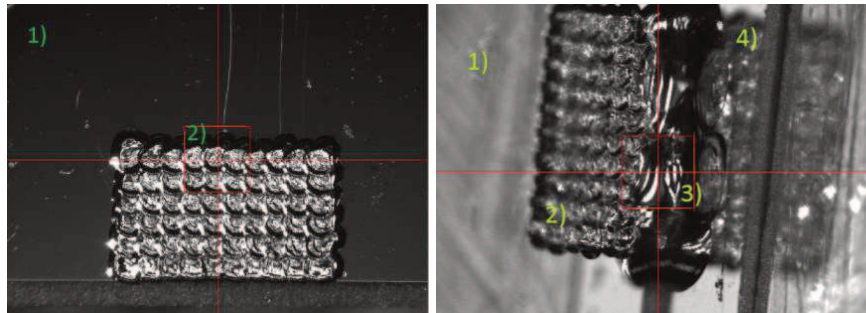


Fig. 5.15. Left, 1) SHG crystal pre-soldered with an array of 60 μm SAC305 bumps 2), the energy used to place each one of the bumps was approximately (using a laser 2220 mA current and 0.425 ms pulse width) 5.9 mJ. Right, 300 μm SAC305 bumps 3) to solder the SHG 1) to the fused quartz sub-mount 4), the energy used for mounting both components was approximately 150 mJ (using a laser 5100 mA current and 5.25 ms pulse width).

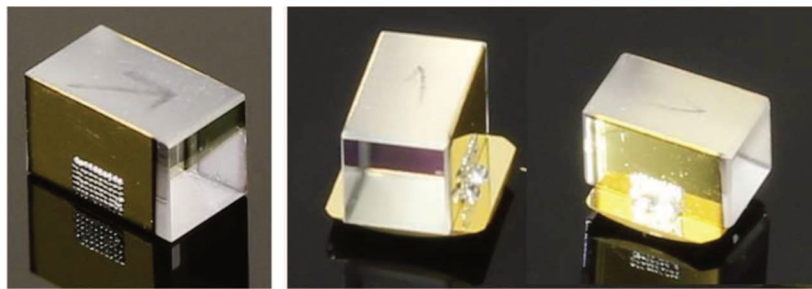


Fig. 5.16. Left, detail of 100 μm SAC305 alloy applied on SHG surface to prevent further damage. Right, mounted SHG crystal onto the spherical fused silica sub-mount.

In the case of the SHG, because it is a highly birefringence uniaxial crystal cut out of the z-optical axis, it was impossible to analyse the induced stress with the Illis polarimeter device; however mechanic simulations performed by ANSYS 17.0 show a maximum of 0.5 MPa stress along the laser beam path.

The mechanical simulations seen on Fig. 5.17 were performed with a unique step for the application of one set of one-hundred twenty bumps of 100 μm diameter and another set of six 300 μm diameter SAC. This is the reason why the simulated stress on the SHG lateral surfaces seems to be in the order of 50 MPa, however, in the real case, the time relaxation between bumps, made the assembly of the components possible without creating internal damage on them.

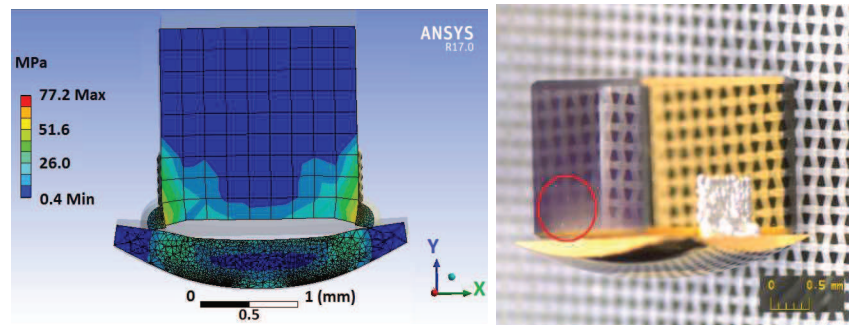


Fig. 5.17. Left, ANSYS stress simulations on the SHG component. Right, detail of small-induced superficial damage created on the SHG crystal. The damage was produced due to defects of the polished SHG crystal surface.

b.3) Laser cavity Alignment and soldering procedures

Grippers for the SHG and output-power laser cavity mirror had shared the same design to allow for simultaneous placement of these two components. The SHG and output-laser mirror were fed to the laser DCB from a bottom-side position allowing access for the solderjet placement capillary. The gripper design comprised a flexure hinge that decreased restraints induced by movement of the Hexapod. Gripper arms made from brass provided a high mechanical stiffness during adjustment and soldering. The components were retained by application of vacuum through a precisely manufactured tip made of Macor®.

The gripper was transversally decoupled from the movements of the Hexapod by means of an air-bearing. A moving plate on the air-bearing contained a distortion lock allowing for self-centring of the components inside the KOVAR ring pad.

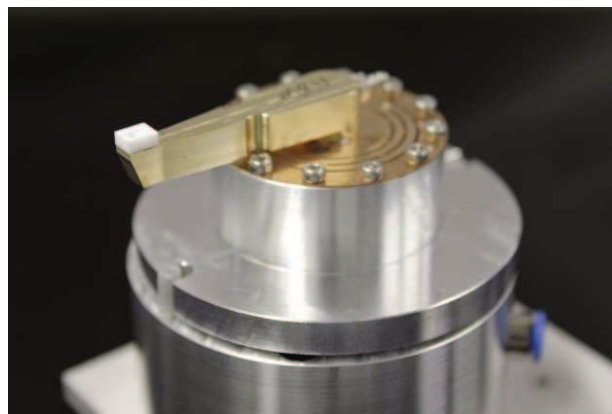


Fig. 5.18. Air bearing gripper used to mount BBO and laser output mirror.

A traverse component above the moving stages of the Hexapods was used to hold the DCB substrate during alignment and soldering.

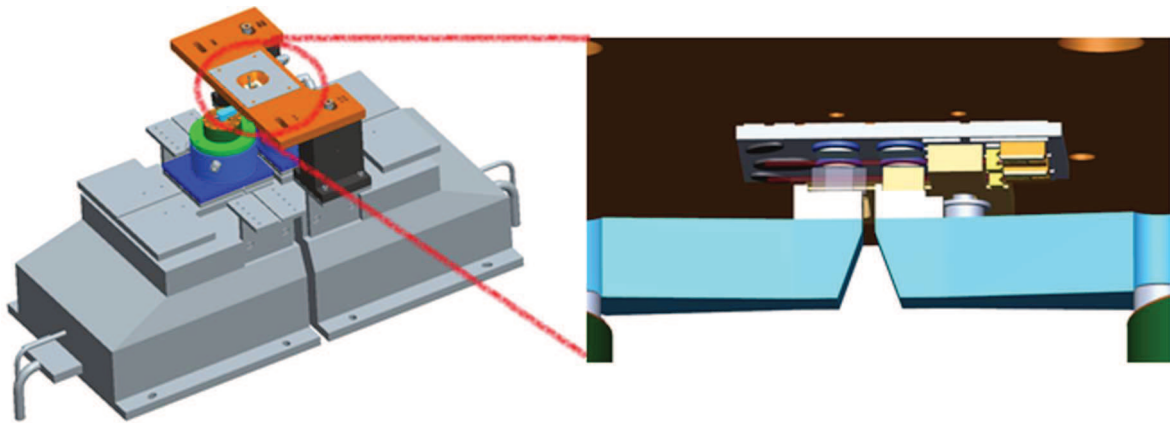


Fig. 5.19. Left, two hexapods allowed for the correct alignment of the SHG and output mirror due to the air-bearing grippers. Allowing for a self-centring procedure of the components that have to be soldered on the on the DCB hold by the traverse component (orange). Right, detail of the output mirror and SHG positioning into the DCB.

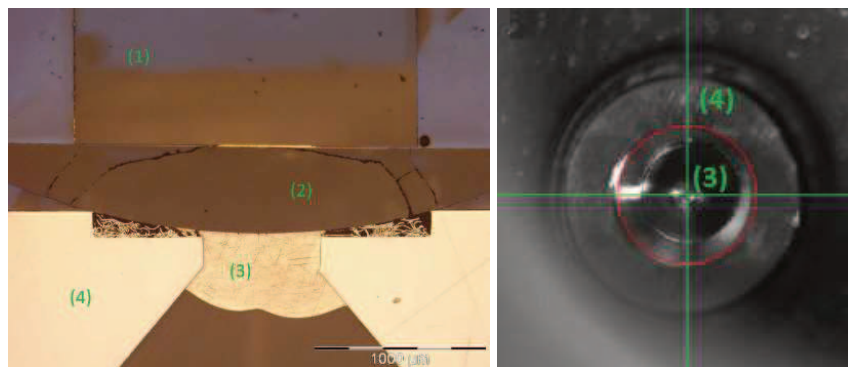


Fig. 5.20. Left, Cross section of soldered component. Right, solderjet bump SAC305 applied from the DCB rear side pad. The mechanical strength provided by this $760\ \mu\text{m}$ bumps proved to withstand shear forces as high as $60\ \text{N}$ [78]. (1) laser component, and (2) $8\ \text{mm}$ half-sphere fused quartz substrate allowing 3DOF inside the KOVAR ring pad (4). (3) Applied $760\ \mu\text{m}$ SAC305 solderjet bump through the (4) small conical feeding geometry under the KOVAR ring pad.

5.2.2.1 VirtualLab Fusion soldered Exomars laser results

Following the assembling procedures described on the previous chapter 5.2.2, and by using the VirtualLab Fusion steps as in chapter 3.1.1.4, several crystal cases per input wavelength were evaluated as described in Table 5.3 in order to investigate the effects produced on the Exomars resonator laser crystal emission due to the soldering of the laser components (Fig 5.21).

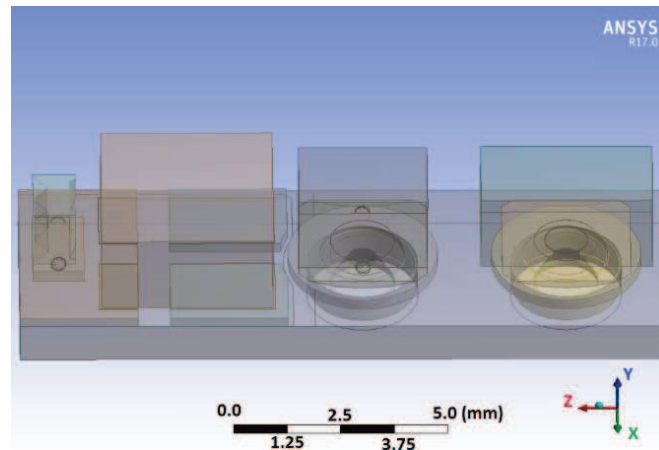


Fig. 5.21. Exomars laser resonator configuration as designed with a FAC, active crystal, a SHG and a FS output mirror.

Table 5.3. Studied laser resonator cavity produced beams and stress crystal conditions. The diode-pumping emission wavelength of 808 nm was avoided for being granted between both extreme 532 nm and 1064 nm laser cavity wavelengths.

| Laser cavity beam | Crystal condition (Active-media/SHG/Fused quartz) |
|--|--|
| 1. Gaussian @1064 nm from active-medium crystal emission, 50 μm waist radius, E_y -polarization | a. Ideal case: without stress |
| | b. Real case: with actual applied stress |
| | c. Comparing case: with increased stress (10x) by design |
| 2. Gaussian @532 nm produced by SHG, 50 μm waist radius, E_x -polarization | |

Starting with the active-medium crystal, as it is established by design on Fig.5.21 and by using the simulated induced stress on the component as shown in Fig. 5.8; it is possible to compare E_y -polarized input Gaussian at 1064 nm in front of the crystal and the output field behind the crystal under the three different crystal conditions (Fig. 5.22).

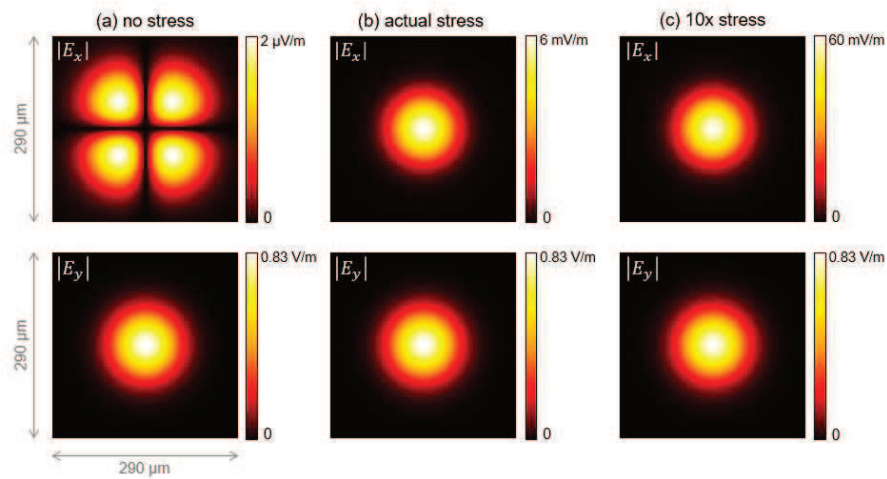


Fig. 5.22. Amplitude of the transmitted field behind the active-medium crystal, with E_y -polarized Gaussian at 1064 nm as the input. Column (a) ideal case without stress; column (b) with actual solderjet bumping packaging induced stress; column (c) with 10 \times increased stress. Upper row corresponds to the E_x -component and lower row the E_y -component.

Again, after introducing a linearly polarized input field along the y-direction, a crosstalk effect produced by the reflection of light at the crystal surface shows a non-zero output field on $|E_x|$ for the case with no applied stress, as seen in column (a) on Fig. 5.22. Comparing column (a) with no stress, to the applied stress in columns (b) and (c), we can appreciate a beam depolarization factor of 0.7 % in (b) and 7% for the case of 10x stress in (c). This stronger stress-effect (although still below 1 % on the actual stress case), is mainly produced by the soldering procedure by a Fineplacer hotplate with AuSn alloy instead of using SAC305.

Later, the SHG was investigated following similar steps to those described on chapter 3.1.1.4, and using the ANSYS results as shown in Fig. 5.17. Starting with the E_y -polarized input Gaussian at 1064 nm the results are shown in Fig. 5.23.

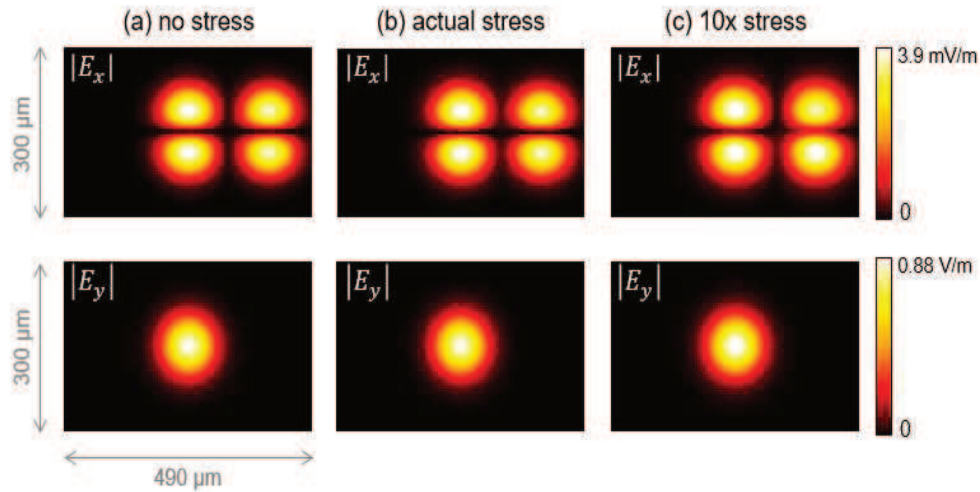


Fig. 5.23. Amplitude of the transmitted field behind the SHG crystal, with E_y -polarized Gaussian at 1064 nm as the input. Column (a) ideal case without stress; column (b) with actual stress; column (c) with 10 \times increased stress. The upper row corresponds to the E_x -component and lower row the E_y -component.

As on chapter 3.1.1.4, it is also seen here, a lateral shift or a walk-off effect produced for being the SHG crystal a uniaxial anisotropic material. When the E_x -polarized Gaussian at 532 nm was used as the input, the output field was obtained as can be seen in Fig. 5.24.

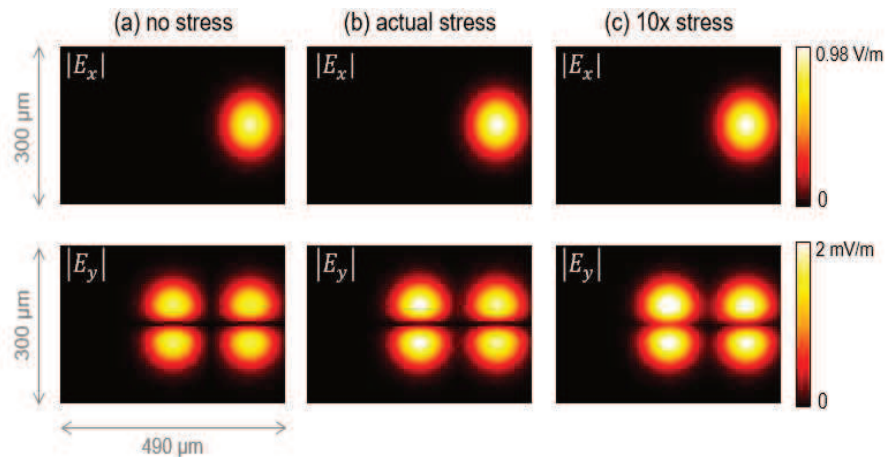


Fig. 5.24. Amplitude of the transmitted field behind the SHG crystal, with E_x -polarized Gaussian at 532 nm as the input. Column (a) ideal case without stress; column (b) with actual studied stress; column (c) with 10 \times increased stress. Upper row corresponds to the E_x -component and lower row the E_y -component.

In the SHG crystal case, and due to the inherent material's high birefringence, the three studied cases for 532 nm and 1064 nm show no influence related to the applied stress. On the three columns (a), (b) and (c), on both Fig. 5.23 and Fig. 5.24, similar depolarization

effect is shown with a depolarization value around 0.5% produced by the material's internal birefringence. Finally, considering the FS output mirror with HR1064 nm and HT532 at the first surface, only the 532 nm study case was necessary.

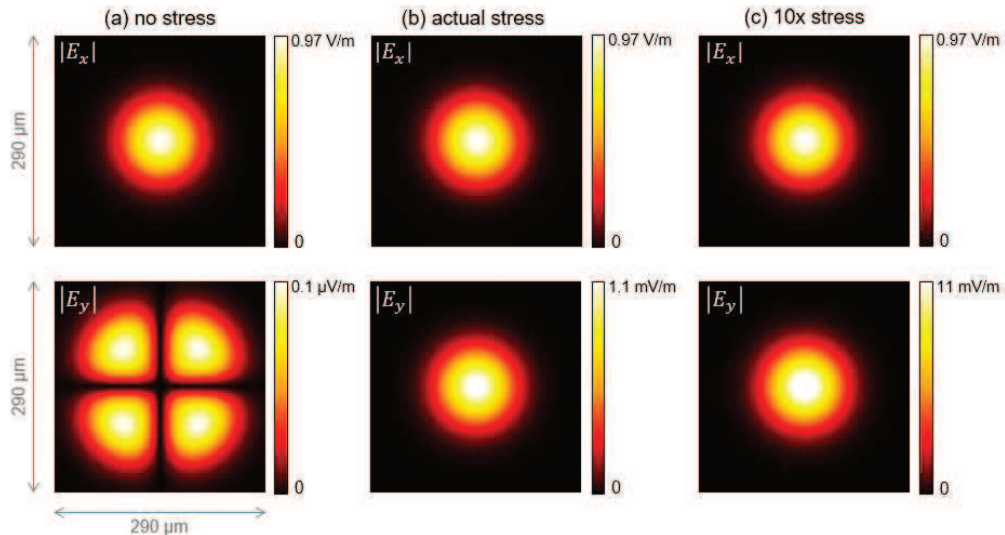


Fig. 5.25. Amplitude of the transmitted field behind the FS output mirror, with E_x -polarized Gaussian at 532 nm as the input. Column (a) ideal case without stress; column (b) with actual studied stress; column (c) with 10 \times increased stress. Upper row corresponds to the E_x -component and lower row the E_y -component.

For the final case of FS output mirror with a with E_x -polarized Gaussian at 532 nm as the input using the ANSYS results as seen on Fig. 5.14, we obtained a depolarization effect for the actual stress (column (b) in Fig.5.24) of around 0.1%, and for the case of 10x stress (column (c) in Fig.5.24) of 1%. Both cases also appeared to be non-relevant for the laser's optical requirements.

Taking into account that the produced effects would be added one after another inside the laser cavity, it may have occurred that the final depolarization effect overpassed the 1% on the overall laser resonator emission; affecting the required 532 nm emission needed for the mission's purpose. However, due to the components' assembling procedure, for which each component had been preassembled onto a substrate, (active-medium crystal soldered to the DCB pads, and SHG crystal and FS output mirror soldered to a FS substrate to guarantee tip/tilt alignment, as described on chapter 5.2.2), this depolarization effects would have been reduced since the final laser resonating cavity is achieved after the components' pre-assembly. For that reason, during the assembly of the Exomars laser cavity, no major

depolarization effect nor effects on the output beam shape were reported. The Exomars laser beam shape obtained achieved a Gaussian fit of 95.44% as seen in Fig. 5.26.

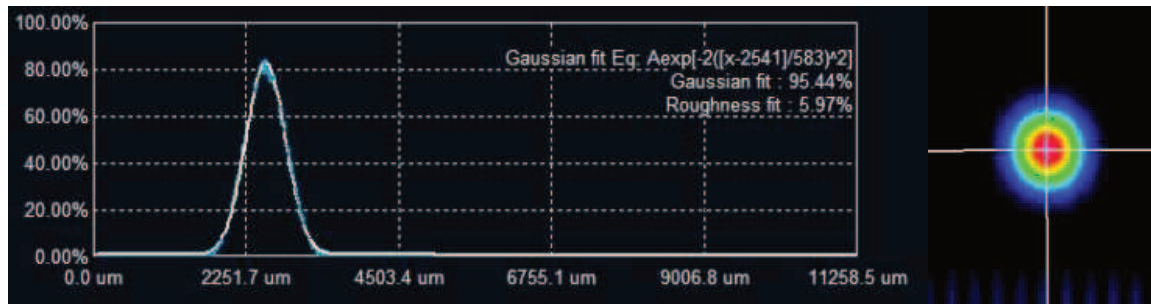


Fig. 5.26. Although high stress had been applied on the laser components, the Exomars green beam spot is still fitting a Gaussian beam. Beam measured 30 cm from laser resonator end mirror.

With this, it is demonstrated that solderjet bumping technology can assemble a laser cavity such as the Exomars' with no stress produced effects on the laser emission. Even more, the amount of SAC305 and AuSn employed as a bonding alloy used for the optical components, will guarantee that the assembled laser cavities can withstand the mission demands [25] described on chapter 5.1.2.

5.2.2.2 FEM structural analysis for the low-stress technology assemblies

The non-operational temperature loads showed a von Mises maximum stresses of 120 MPa (Fig. 5.27) in the boundary regions of the soldered areas (yield strength of Au80Sn20 is 275 MPa, yield strength of SAC305 is 45 MPa), however the joining areas stayed commonly under the 30 MPa as an average, especially those laser resonator optical components for which the SAC305 solder was applied (Fig. 5.27). The conclusion, thus, is that during non-operational thermal cycling, no relevant stresses that could lead to irreversible deformation are detected.

The modal analysis showed a first, second and third eigenfrequencies of 10089 Hz, 12882 Hz and 12182 Hz respectively. Thus, the soldered assembled devices also fulfilled the modal first frequency requirement. The increase in the first eigenfrequency is mostly due to design modifications of the laser structure itself from the adhesive based to the soldered devices. Sine and random analysis did not show any irreversible deformation; no eigenfrequencies into the 0-2000 Hz were expected. Due to the low weight of the components, the stress due to shock load showed to be very low

(less than 10 MPa on the laser housing, around 2 MPa on the soldered areas and <1 MPa on the laser resonator components), hence, no plastic strain and irreversible deformation it is expected [79] to occur due to shock load on a range between 100-1500 g.

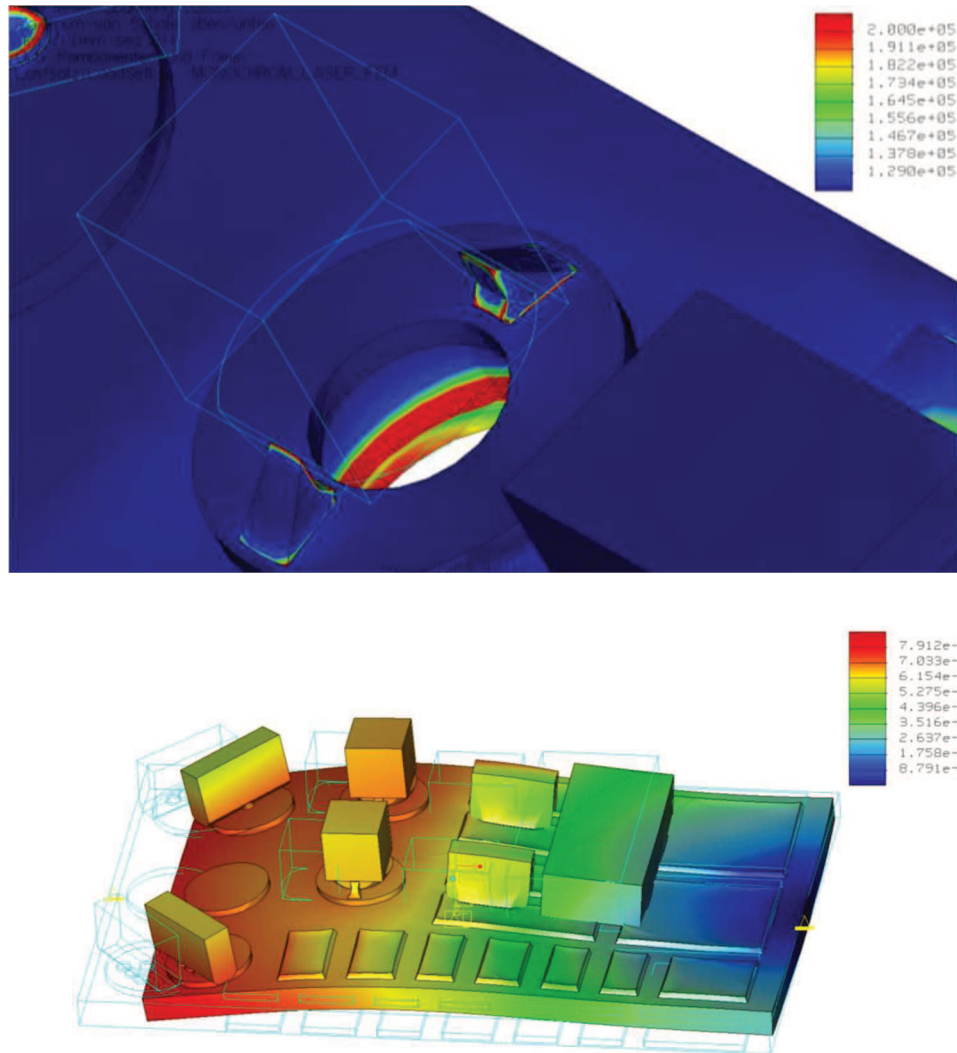


Fig. 5.27. First row, Von Mises stress shown on the soldered areas by means of SAC305. Below, assembly magnified deformation in millimetres due to temperature difference during laser operation (+15 °C to +45 °C).

5.2.2.3 Power loss due to components metallization

Laser crystal emission, produced by internal laser cavity oscillation is mostly achieved due to the use of the proper coatings (high-reflective HR and anti-reflective AR) applied on the laser's components. The coating quality is a key factor to obtain high oscillation inside the cavity that allows achieving a final high conversion efficiency and out-put power. The evaporated dielectric films [80] on components are usually applied

by evaporation and condensation of materials inside a vacuum chamber [37], following similar procedures to the ones used to create wettable surfaces (Ti/Pt/Au layers) on the components to be soldered. It has been noticed that Exomars lasers built following gluing procedures had higher out-put power in average than the ones obtained by soldering means. However, a comparative study is difficult to be completed, since not a relevant statistical number of devices has been assembled, and also because the SHG tends to create unstable non-linear cavities with different out-put power. Nevertheless, the maximum obtained out-put power by the laser assembled using adhesive means was around 800 mW @532 nm (@3,5 A) when for the same wavelength and current, the case of the soldered devices had a maximum out-put power around 500 mW (during alignment). This made us consider the fact that even creating complex masking tools for the components' metallization (Ti/Pt/Au layers), some deterioration of the original coatings or even some Ti/Pt/Au layer leakage occurred on the their optical surfaces.

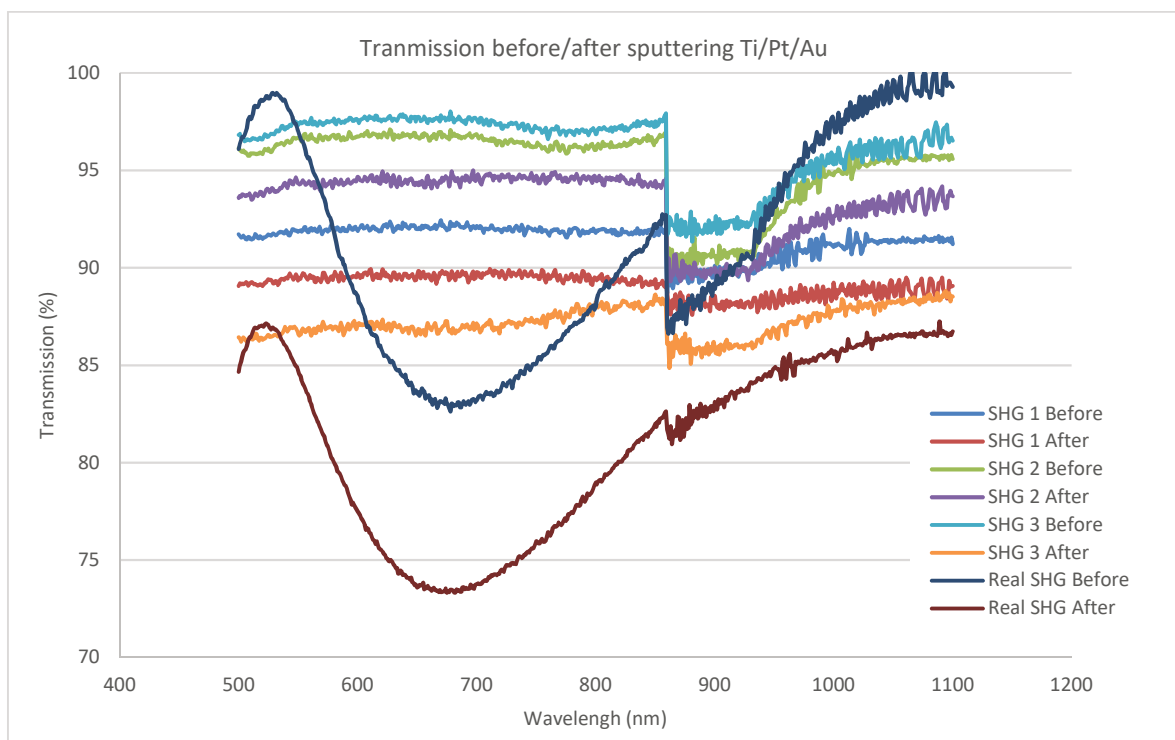


Fig. 5.28. Comparison between optical transmissions (from 500 nm to 1100 nm) before and after components' metallization with Ti/Pt/Au. The comparison was made using a UV-VIS-NIR Spectrophotometer Lambda 950 Perkin Elmer. The attached graphic shows the comparison between three SHG dummy components similar to the one used on the Exomars laser with dimensions of 2X2X3 mm, and a real SHG component later soldered to one of the Exomars lasers. The light transmission curves of the dummies and the real SHG is different because the real components had AR coating for 532 and 1064 nm.

In average, the light transmission loss for the analysed components (dummy SHG, SHG, dummy active-medium crystal, real active-medium crystal, dummy out-put mirror and output mirror) was around 6% (Fig. 5.28), effect that could be the reason for the power loss due to the light oscillation by several passes through the components surfaces. Since for our purpose the laser did not require more than an operational output power of 30 mW, and the working capacity studied trough a burn-in tests seems not to be compromised, this was not considered a project bottleneck; however, it is to be studied for future improvements.

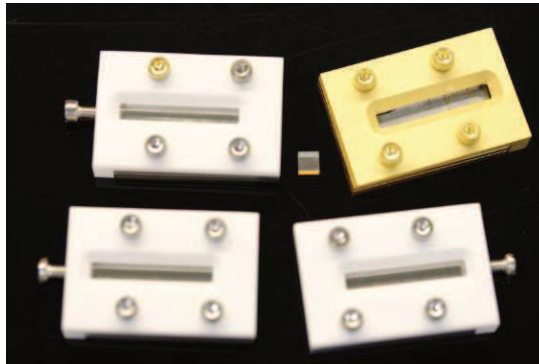


Fig. 5.29. Designed and manufactured devices to metallize only the surfaces required for soldering. After the components' metallization no Ti/Pt/Au layers were seen on the optical surfaces through a visual inspection with a microscope.

5.3 Performed environmental tests on adhesive and soldered devices

After assembling the laser devices by adhesive and low-stress soldering based procedures, functional tests before, during and after environmental tests were carried out to assure that laser's performances were endured. Laser power and wavelength, being both crucial parameters for the Raman spectroscopy analysis, had to be guaranteed. Thus, power stability, FWHM and linewidth shifting were constantly checked during tests on devices assembled by both technologies (Fig. 5.4 & 5.5). Measurement data of input current versus output laser power were analysed at different temperatures between +15 °C and +45 °C. Any change during and after environmental tests might indicate a laser resonator or on any of the other passive components misalignments, leading to a laser power drop. Power stability and noise tests at constant temperature were also performed. Stability studies included laser peak wavelength and linewidth emission measurements over 20 min periods (time needed for the analysis of samples on the Martian surface) at a constant temperature [66].

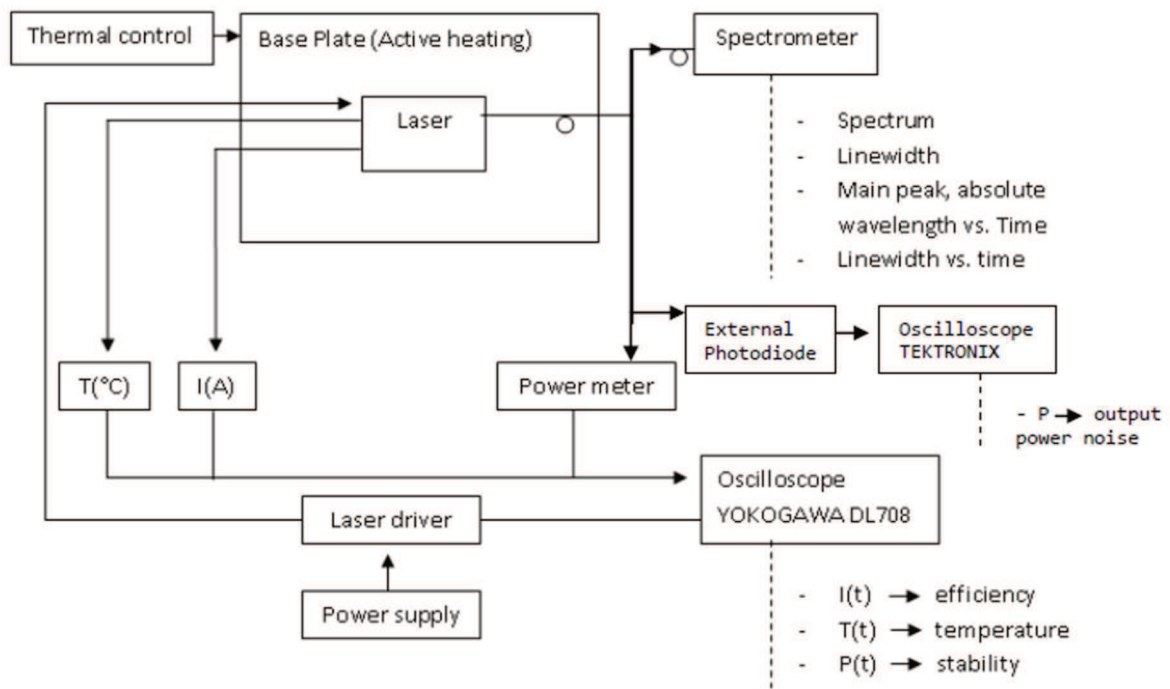


Fig. 5.30. Test set-up diagram for the laser functional tests.

As for the environmental tests, both the adhesive based and soldered lasers were subject to vibration (random and sine) and shock tests under standard conditions of pressure and temperature. Cycles of non-operational thermal conditions were conducted in a temperature range between $-60\text{ }^{\circ}\text{C}$ and $+70\text{ }^{\circ}\text{C}$, with a maximum gradient of $5\text{ }^{\circ}\text{C}/\text{min}$ and with a dwell time of 150 min at the maximum and minimum temperatures after the fulfilment of the stabilization criteria.

Last, radiation resistance tests were performed both on the optical components and onto the assembled devices [81]. Although it is true that some optical components (as fused silica, second-harmonic generation crystals), and other laser devices passed similar gamma and proton radiation tests [82]-[83], it is difficult to analyse how this effects can change the emission of a particular laser resonator, as is the case for the present Exomars laser. The tests were performed with a conservative 20 krad TID (Total Ionizing Dose) gamma radiation and 10 MeV proton with a frequency of $2.4 \cdot 10^{10}\text{ p}/\text{cm}^2$ (Table 5.4 & Table 5.5) [84]. The ion radiation was applied by a Co-60 source housed in an AEXL Theratron 780 in four different steps with an absorbed homogeneity dose better than 5% as shown in Table 5.4.

Table 5.4. Ion radiation steps applied at the assembled Exomars lasers (measured in rad(Si), radiation absorbed relative to silicon).

| Step | Step dose (krad(Si)) | Accumulated dose (krads(Si)) |
|------|-------------------------|---------------------------------|
| 1 | 5 | 5 |
| 2 | 5 | 10 |
| 3 | 5 | 15 |
| 4 | 5 | 20 |

The maximum calculated proton radiation that the laser devices will have to withstand is calculated to be $5.4 \cdot 10^{10}$ 10 MeV p/cm². These tests were performed at Radiation Effects Facility (RADEF), Accelerator laboratory of the University of Jyväskylä (Finland). The doses were applied in five different radiation fluencies as shown in Table 5.5.

Table 5.5. Proton radiation steps applied at the assembled Exomars lasers.

| Step | Step fluence (10 MeV p/cm ²) | Accumulated fluence (10 MeV p/cm ²) |
|------|---|--|
| 01 | $\sim 5.0 \cdot 10^8$ | $\sim 5.0 \cdot 10^8$ |
| 02 | $\sim 2.0 \cdot 10^9$ | $\sim 2.5 \cdot 10^9$ |
| 03 | $\sim 2.5 \cdot 10^9$ | $\sim 5.0 \cdot 10^9$ |
| 04 | $\sim 2.0 \cdot 10^{10}$ | $\sim 2.5 \cdot 10^{10}$ |
| 05 | $\sim 3.0 \cdot 10^{10}$ | $\sim 5.4 \cdot 10^{10}$ |

5.4 Results and conclusions

The assembled miniaturized laser on the AlN substrate by means of adhesive processes (seen in Fig. 5.5) finally weighted 4.1 g, with a designed laser housing of 47.5 g, which represented a total weight of 51.6 g. The laser volume assembled on the AlN by design was 2.4 cm³; with a laser housing total volume of 6.5 cm³. On the other hand, the solder-miniaturized laser on the AlN substrate weighted 3.1 g (as seen in Fig. 5.4); its laser housing

was designed with a weight of 42.4 g, which represented a total device weight of 45.5 g. The assembled laser on the AlN substrate had an approximate volume of 2.4 cm³; and a total laser volume of 4.7 cm³, including the laser housing. Design changes due to assembling procedures demands created differences on the final weight and sizes for the assembled devices; however, both techniques passed the Exomars mission approximate requirements of 7 cm³ and 50 g.

The devices assembled with both procedures also passed initial functional laser performance tests right after the components had been assembled. Giving results as; device efficiency below the 1.5 W of electrical consumption (pumping diode laser current <0.85 A) with an output power of 30 mW (@532 nm), power stability better than 5%, power signal noise under the 1.5% required, central wavelength stability below the 50 pm, and a linewidth below the 30 pm. Fig. 5.31 shows an example of results on the functional performance test of one of the lasers assembled by adhesive means.

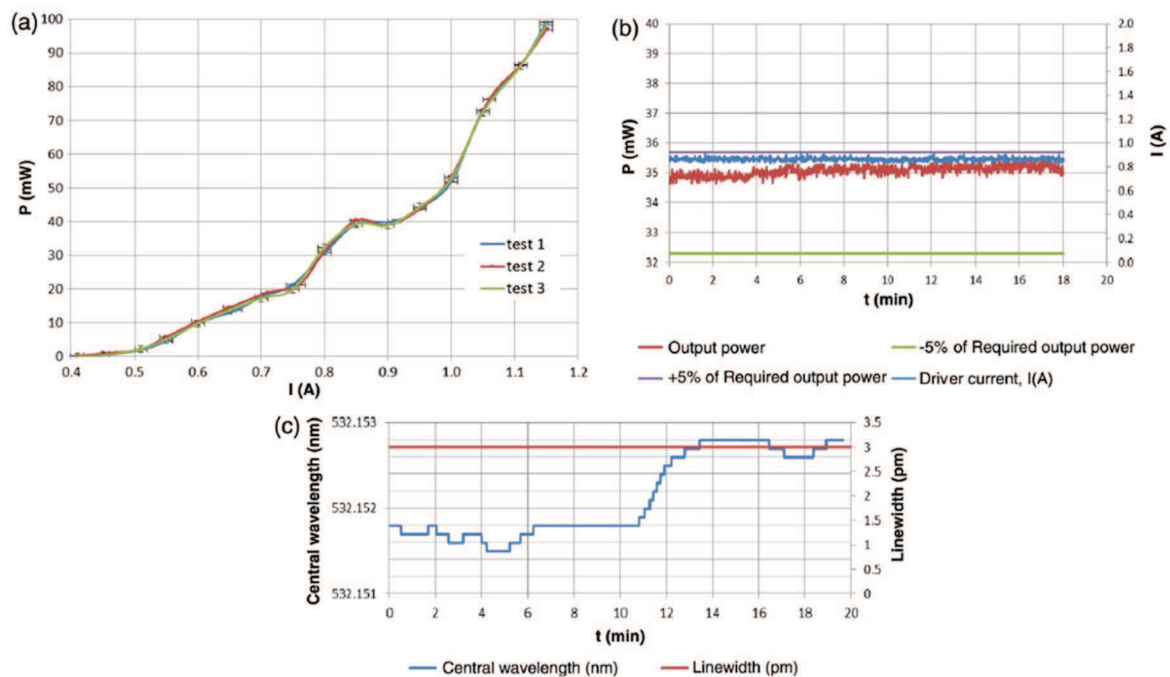


Fig. 5.31. Examples of results seen on one prototype assembled by adhesive means. First image left (a), input current versus output power of the green laser, different measures were taken on the same device to verify laser emission repetitively; second image on the right (b), an output power stability better than 5%. Last image below (c), centre wavelength and linewidth stability over 20 min at constant temperature.

Although no damages were identified after the vibrational and shock tests on adhesive based miniaturized green lasers, a constant degradation on the output power was observed during thermal non-operational and functional thermal on/off laser cycles. After the thermal tests, the results on functional optical performance tests showed that the output power stability deviation overpassed the maximum of 5% permitted; also the laser emission changed to a deteriorated spectrum with secondary competitive peaks (Fig. 5.32).

It was also noticed that laser cavities that did not pass environmental tests had gradually misaligned along the few weeks that followed the laser's assembly. Changes due to post-curing adhesive and aging processes in these laser cavities have been calculated to be between ~10-30 arcsec: enough to achieve a loss of the optical performances in such sensitive laser cavities [66]. This unreliable behaviour made the adhesive assembled prototypes not valid for the Martian space mission. Moreover, the assembled adhesive based prototypes and also independent optical components passed ion radiation tests; no major degradation was observed on the devices. Nevertheless, these lasers did not overcome the conservative proton radiation performed tests. It is believed, however, that since the lasers will be screened by the rover shell, the actual proton radiation rates will be significantly lower ($\sim 5.0 \cdot 10^8$ MeV p/cm² total), enabling a correct laser operation during the Exomars mission.

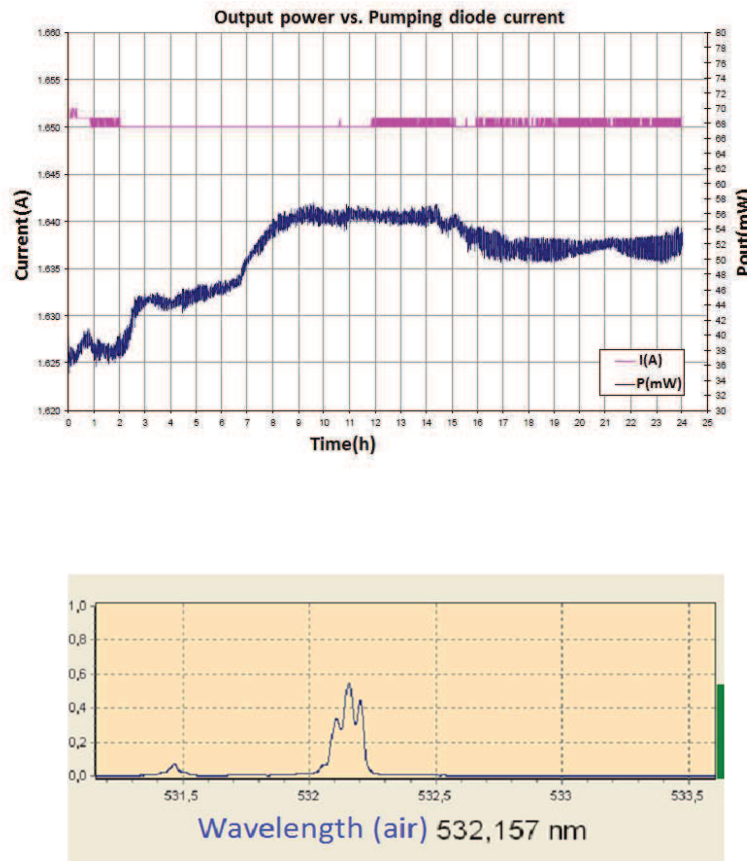


Fig. 5.32. Left, example of power instabilities encountered after thermal cycles on adhesive assembled lasers. Right, appeared competitive peaks after adhesive based devices thermal cycles.

Thermal non-operational, functional thermal-cycles, mechanical and ion radiation tests on the soldered miniaturized green lasers were performed as described above with no damages noticed during visual inspection of the samples. There were no important changes in the stability of the main optical parameters (linewidth, wavelength, and peak level) or output power degradation of the tested samples before and after mentioned above environmental tests. However, the soldered devices did not either overcome proton radiation tests due to laser power drop during the radiation steps; probably caused by the darkening of the laser crystal [85]-[86]. The proton radiation tests are arranged to be repeated using significant lower doses ($\sim 5.0 \cdot 10^8$ MeV \cdot p/cm 2).

The environmental tests and functional characterization showed an improvement in terms of laser stability and aging for soldered lasers in comparison to adhesive based lasers. Exomars Raman laser adhesive based prototypes showed a constant degradation after thermal cycles and also after periods of scarce weeks' time due to adhesive post-curing processes, leading to misalignment of the laser resonator cavities and final laser failure. On

the other hand, the laser cavity components alignment remained stable in the devices assembled with the solderjet technology. This proves that soldering the optical components solves the issues that adhesives introduced to the Exomars laser's performances.

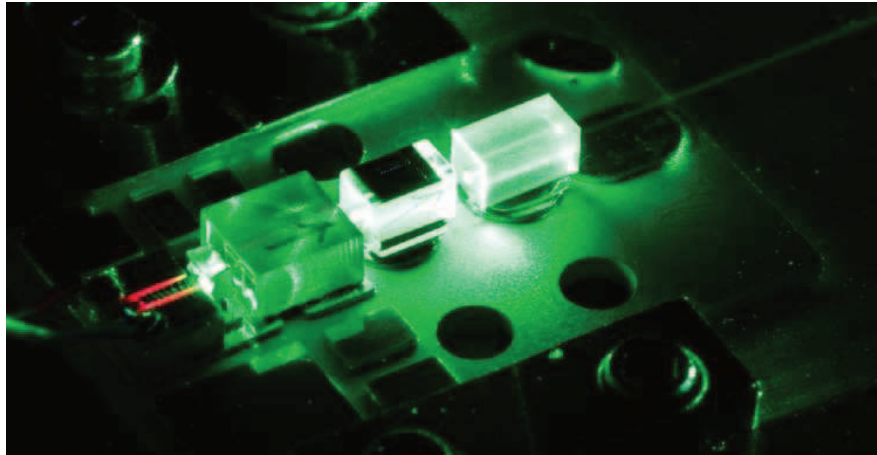


Fig. 5.33. Exomars EQM assembled laser by solderjet bumping technology emitting at 532 nm after SHG.

6 Conclusions and outlook

As exposed in the introduction of this dissertation, the main disadvantage of soldering optical components when compared to common adhesive technologies is the stress induced onto the components. This effect could inevitably lead to a decreased laser beam quality ($M^2 > 1$), to a beam depolarization ratio, and even cause an impaired output power. On the other hand, laser devices are nowadays required for several applications in which their robustness needs are hardly reached by gluing technologies. These unsolved difficulties drove our attention and led us consider evaluating the effects of a low-stress soldering technology called solderjet bumping, for which a theoretical investigation on stress-induced birefringence produced by the soldering packaging process was implemented and here described for the first time.

In order to design this analysis, a theoretical modelling case study that included 2 mm cube side laser components was considered. Using those geometries and materials, different sets of thermo-mechanical simulations by ANSYS 17.0 were performed with the final stress results being converted into dielectric permeability matrix through the use of a detailed mathematical approach. With those results, and by applying a self-made written code into VirtualLab Fusion software, the different consequent effects on laser cavities produced by stress-induced birefringence due to components' packaging in terms of beam depolarization and beam quality were studied. As a result, the first study cases proved that the solderjet bumping technology only produces a residual effect on the devices, barely affecting laser components with a few millimetres body sizes. This theoretical demonstration not only provided the solution to overcome the stated **Objective 1** (*create a theoretical model design that relates induced packaging stress, induced birefringence and cavity lasers output misbehaviors*) at this thesis work, but also created a new package module in VirtualLab Fusion software that will help any other user to study and improve their optical packagings. By adjusting the different parameters included in the simulations, such as material data, crystal morphology and tensorial expressions, other readers can use the created method not just to investigate the laser crystal packagings, but also for heat dissipation removal on laser crystal's, simplifying the present mathematical methods found in the literature ([32]-[39]).

Later on, the decision to optimize the study by decreasing the size of the laser components while guaranteeing robust enough joints to withstand harsh environments was

taken. For this, the limiting factors of the technology were studied to understand the ratio between the minimum components sizes and maximum beam size, at which the laser beam is not affected and the devices can withstand external loads produced by harsh environmental conditions. As a result, it was concluded that the use of solderjet bumping technology made it possible to build miniaturized laser devices on the size ranges of the laser beam emission without affecting the lasing capabilities with a depolarization ratio below 0.1 %. With this, the thesis's **Objective 2** (*investigate the laser based soldering technique used to assemble laser devices, and get the basic knowledge of minimum laser cavities size without affecting laser output performances*) was achieved. Moreover, these miniaturized components proved to withstand loads similar to the required for space missions such as the Exomars ESA 2020 mission.

The above explained results and the consequent achievement of Objectives 1&2 proved that solderjet bumping technology overpassed the requirements of the current state of the art, showing that the initially assumed main disadvantage of induced stress and consequent birefringence is not a constrain to assemble miniaturized laser cavities. It was shown how solderjet bumping could be applied just by using a localized and minimized induced thermal energy without affecting consecutively the components' laser emission.

After assessing the components' size limitations, solderjet bumping technology was used to assemble a DPSSL meant for a space mission, for which robustness was a key limiting factor not reachable by adhesive means. Moreover, the devices miniaturization was a constrain for clamping methods. The methods chosen to align and robustly solder the brittle materials and sensitive laser resonator cavities designed have been tested and demonstrated along the present dissertation, and have been proved to work under the optical and technical requirements established by the ESA mission's needs.

The devices assembled by the use of solderjet technology have been proved to pass Engineering Qualification Model (EQM) tests, and in better conditions than similar devices assembled by adhesive means. Finally, the EQM devices were installed into the Martian scientific platform of the rover RLS and into ICEU Martian unit, where they were able to properly measure Raman spectra from simulated Martian samples (Fig. 6.1). With this, the **Objective 3** (*investigate the use of new laser assembling techniques that could work beyond the actual state of the art in terms of robustness. And compare former assembling techniques with new soldering assembling techniques*) was achieved. Once more, solderjet bumping technology proved to work beyond the current state of the art of previously used technologies.

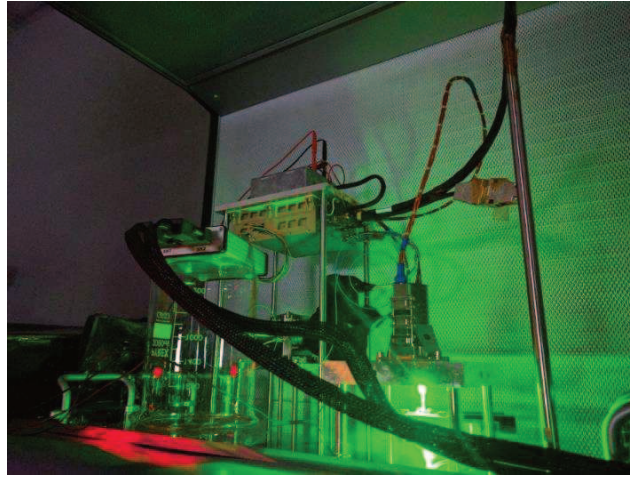


Fig. 6.1. EQM DPSSL assembled by solderjet means mounted on Exomars scientific body (ICEU) fully operating and measuring Raman spectra [87].

After passing the EQM tests, several FM laser devices have been assembled (Fig. 6.2) and are in process to be tested to finally select the one that will be launched on the long journey to the red planet. In the literature, there is no report of any fully soldered and miniaturized DPSSL device able to withstand similar environmental level condition requirements; or soldered and assembled laser device previously sent to the space. The last **Objective 4** (*achieve laser device operation assembled with soldering techniques, being able to perform in harsh environmental conditions*), was finally accomplished after a stringent process to evaluate the best laser design and assembling procedures. The final laser design and the used technologies were also successfully qualified under the EQM tests campaign. This points the solderjet bumping technology as a qualified technology for other ESA space missions.

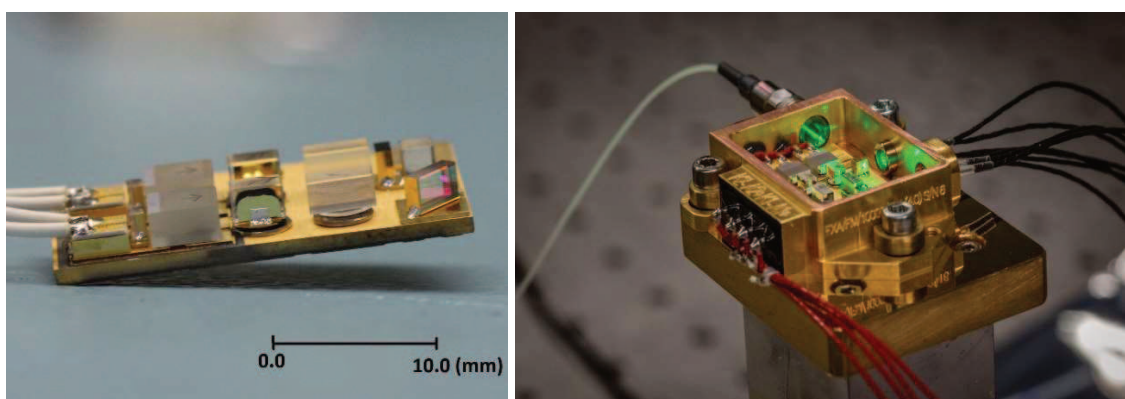


Fig. 6.2. Finished miniaturized FM DPSSL-laser assembled by solderjet technology means and ready to be delivered to ESA.

Once the final laser is installed onto the final Martian Exomars rover, and launched to Mars in 2020, the scientific goal of the miniaturized frequency doubled DPSSL assembled using solderjet bumping technology will be to help searching for signs of past and present life on the fourth planet from the sun in the solar system (Fig. 6.3) [3],[88]-[89].

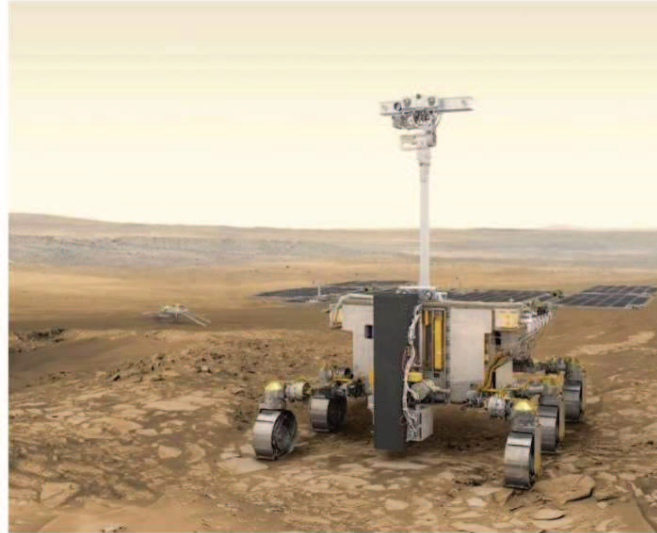


Fig. 6.3. Schematic of the designed Exomars Rover at which the final FM laser will be installed [90] and launched direction to Mars in 2020.

The work developed in this thesis can be used to improve laser packaging and assembling techniques by following the steps and the design guidelines showed on the dissertation previous chapters. The mathematical theoretical demonstrations can be used for any other laser manufacturing applied technique, including laser components heat-removal during laser operation. Moreover, interested readers that want to use other soldering techniques to assemble miniaturized laser devices should consider the minimum exposed size boundary conditions in terms of maximum reached stress to avoid altering the optical device-requested characteristics of the laser operation.

The Exomars Laser Spectrometer is a project funded by Ministerio de Economía y Competitividad (MINECO), Spain, and supervised and followed by Instituto Nacional de Tecnología Aeroespacial (INTA), Spain. The activities related to the dissertation chapter 5 were partially performed under a contract with Monocrom s.l, Spain, which was at the same time contacted by INTA, under the Exomars project Spanish funding. The rest of the dissertation activities were funded by the Fraunhofer Institute for Applied Optics and Precision Engineering IOF, and by the Friedrich-Schiller-University of Jena, Germany.

References

- [1] D. Wernham, J. Alves, F. Pettazzi, A.P. Tihe, “Laser-induced contamination mitigation on the ALADIN laser for ADM-Aeolus”, in Proceedings of SPIE, Vol. **7842**, (2010); doi:10.1117/12.867268.
- [2] S. Ferrando, M. Galan, E. Mendez, E. Romeu, D. Montes, A. isern, M. Jardí, J. Juliachs, G. Viera, “Novel compact 500 mW green laser for extreme enviroments”, www.monocrom.com.
- [3] F. Rull, S. Maurice, I. Hutchinson, A. Moral, C. Perez, C. Diaz, M. Colombo, T. Belenguer, G. Lopez-Reyes, A. Sansano, O. Forni, Y. Parot, N. Striebig, S. Woodward, C. Howe, N. tarcea, P. Rodriguez, L. Seoane, A. Santiago, J.A. Rodriguez-Prieto, J. Medina, P. Gallego, R. Canchal, P. Santamaría, G. Ramos, J. L. Vago, on behalf of the RLS Team, “The Raman Laser Spectrometer for the ExoMars Rover Mission to Mars”, ExoMars Rover Mission, Astrobiology, Vol. **17**, Iss. 6 and 7, (2017); doi: 10.1089/ast.2016.1567.
- [4] V.K. Jain, U.S. Dixit, C.P. Paul, A. Kumar, “Micromanufacturing: A review--part II”, Proceedings of the Institution of Mechanical Engineers, Parts B: Journal of Engineering Manufacture, (2014); doi: 10.1177/0954405414539492.
- [5] R. M. do Nascimento, A. E. Martinelli, A. J. A. Buschinelli, “Recent advances in metal-ceramic brazing”, *Cerâmica* **49**, pp. 178-198, (2003); doi: 10.1590/S0366-69132003000400002.
- [6] P.Ribes, C. Koechlin, M.Hornaff, A. Kamm, E. Beckert, G. Fiault, R. Eberhardt, A. Tünnermann., “High-precision opto-mecanical lens system for space applications assembled by innovative local sodlring technique”, *Opt. Eng.* Vol. **55**, Iss. 6, 065101 (2016). doi:10.1117/1.OE.55.6.065101 .
- [7] P. Wagner, “Laser-induced contamination on high-reflective optics”, Master Thesis, University of Applied Science Darmstadt & DLR- German Aerospace Center (2014).
- [8] H. Faidel, “Montage nichtlinearer optischer Kristalle für den Einsatz in der Luft- un Raumfahrt”, Dissertation RWTH Aachen University (2014).
- [9] A. Würsch, M. Scussat, R. Clavel, R.P. Salathe, “An innovative micro optical element

-
- assembly robot characterized by high accuracy and flexibility,” in *Electronic Components and Technology Conf.*, pp. 218–222 (2000).
- [10] A. Schoeppach, J. Rau, G. Fedosenko, L. Gorkhover, G. Klose, S. Wiesner, H. J. Trefz, M. Widmann, U. Bingel, C. Ekstein, G. Albrecht, “Method and device for connecting an optical element to a frame,” Patent No. PCT/EP2007/009177 (2007).
- [11] M. Kühnelt, T. Schwarz, and U. Steegmüller, “Arrangement of a micro-optical component on a substrate, a method for adjustment of the arrangement, and an optical system with the arrangement,” U.S. Patent No. US20,050,276,542 A1 (2005).
- [12] H. Banse, E. Beckert, R. Eberhardt, W. Stöckl, J. Vogel., “Laser beam soldering—a new assembly technology for microoptical systems,” *Microsyst. Technol*, Vo. **11**, pp. 186–193 (2005).
- [13] E. Beckert, T. Oppert, G. Azdasht, E. Zakel, T. Burkhardt, M. Hornaff, A. Kamm, I. Scheidig, R. Eberhardt, A. Tünnermann, and F. Buchmann, “Solder Jetting - A Versatile Packaging and Assembly Technology for Hybrid Photonics and Optoelectrical Systems,” *IMAPS 42nd International Symposium on Microelectronics, Proceedings*, Vo. **42**, pp. 406-412 (2009).
- [14] J. Braeuer, J. Besser, M. Wiemer, T. Gessner, “A novel technique for MEMS packaging: Reactive bonding with integrated material systems”, *Sensors and Actuators A: Physical*, Vol. **188**, Elsevier (2012).
- [15] M. Datta, R.D. Jr. Whaley, M. Dagenais, “Design and fabrication of thin film resistive heaters for hybrid optoelectronic packaging”, *IEEE Transactions on Advanced Packaging*, Vol. **25**, Issue 4, pp. 495-502, (2002); doi: 10.1109/TADVP.2002.807605.
- [16] H. Faidel, B. Gronloh, M. Winzen, E. Liermann, D. Esser, V. Morasch, J. Luttmann, M. Leers and D. Hoffmann, “Passive alignment and soldering technique for optical components,” *Proc. SPIE*, Vol. **8235**, 82351I (2012); doi:10.1117/12.906726.
- [17] A. Diening, D.E. Harryman, E. Allee, “Athermalized permanent-alignment optical-element mount”, U.S. Patent No. US20130200062A1, (2012).
- [18] FINEPLACER® lambda, Flexible Sub-micron Die Bonder. <http://eu.finetech.de/products/micro-assembly/fineplacerr-lambda.html>.
- [19] Ficontec micro assembly machines, <http://www.ficontec.com/applications/laser-bar->

bonding/.

- [20] M. Leers, M. Winzen, E. Liermann, H. Faidel, T. Westphalen, J. Miesner, J. Luttmann and D. Hoffmann, "Highly precise and robust packaging of optical components," Proc. SPIE, Vol. **8244**, 824404 (2012); doi:10.1117/12.920016.
- [21] T. Burkhardt, M. Hornaff, A. Kamm, M. Rütz, T. Possner, E. Beckert, R. Eberhardt and A. Tünnermann, "Assembly of a photonic wavelength-division multiplexing device using laser-based soldering," Proc. SPIE, Vol. **8069**, 80690V (2011); doi:10.1117/12.887001.
- [22] T. Burkhardt, M. Mohaupt, M. Hornaff, B. Zaage, E. Beckert, H. J. Döring, M. Slodowski, K. Reimer, M. Witt, R. Eberhardt, and A. Tünnermann, "Packaging Technology of Multi Deflection Arrays for Multi-Shaped Beam Lithography," IMAPS 44th International Symposium on Microelectronics, Proceedings, Vo. **44**, pp. 600-607 (2011).
- [23] T. Burkhardt, M. Hornaff, P. Ribes, A. Kamm, D. Burkhardt, S. Kousar, E. Beckert, R. Eberhardt and A. Tünnermann, "Laserlöten optischer Systeme – Anwendungen des Solderjet Bumpings," 9. Jenaer Lasertagung 2014, in: DVS-Berichte Band 370, Innovative Fertigung durch Lasersysteme neuester Generation, Vorträge und Posterbeiträge der 9. Jenaer Lasertagung am 20. und 21. November 2014, DVS Media, Düsseldorf, (2014), ISBN 978-3-945023-04-4, ISSN 0418-9639.
- [24] Ilis GmbH. StrainMatic®. <http://www.ilis.de/en/strainmatic.html>.
- [25] S. Ott. Exomars Project Team, "Exomars 2018 mission and system requirements document EXM-M2-RSD-ESA-00003 Issue 1," http://emits.sso.esa.int/emits-doc/ALENIA/Exomars/ExoMars_Mission_2018/EXM-M2-RSD-ESA-00003_M-SRD1.0_paper%5B1%5D.pdf (2013).
- [26] Zwick Roell. <https://www.zwick.com>
- [27] TIRA GmbH. <http://www.tira-gmbh.com/>
- [28] J. F. Nye, "Physical properties of crystals", Oxford Universty Press, (2010).
- [29] The Engineering ToolBox. http://www.engineeringtoolbox.com/stress-strain-d_950.html

-
- [30] ANSYS, Inc., “ANSYS Mechanical APDL Theory Reference”, <http://148.204.81.206/Ansys/150/ANSYS%20Mechanical%20APDL%20Theory%20Reference.pdf>. (2013)
- [31] P. Ribes-Pleguezuelo, S. Zhang, E. Beckert, R. Eberhardt, F. Wyrowski, A. Tünnermann, “Method to simulate and analyse induced stresses for laser crystal packaging technologies”. *Optics Express*, Vol. **25**, Issue 6, pp. 5927-5940 (2017) <https://doi.org/10.1364/OE.25.005927>
- [32] Q. Lü, U. Wittrock, S. Dong, “Photoelastic effects in Nd:YAG rod and slab lasers,” *Opt. Laser Technol.* Vol. **27**, Iss. 2, 95–101 (1995).
- [33] Y. B. Band “Light and Matter: Electromagnetism, Optics, Spectroscopy and Lasers”, Wiley, ISBN: 978-0-471-89931-0 (2006).
- [34] G. Golub, and F. Charles, *Matrix Computations*, Johns Hopkins University, (1983).
- [35] X. Liu, W. Zhao, L. Xiong, H. Liu “Packaging of High Power Semiconductor Lasers”, Springer (2015).
- [36] H. Y. Zhu, C. W. Xu, J. Zhang, D. Y. Tang, D. W. Luo, Y. M. Duan, “Highly efficient continuous-wave Nd:YAG ceramic laser at 946 nm”, in *Laser Physics Letters*, Vol. **10**, Iss. 7. (2013)
- [37] W. Koechner, “Solid-State Laser Engineering”, Springer Series in Optical Science, Springer (2006).
- [38] T. Graupeter, C. Pflaum, “Simulation of Birefringence in Laser Crystals”, *Proc. of SPIE*, Vol. **8959** (2014). Doi:10.1117/12.2037321.
- [39] S. Chenais, F. Druon, S. Forget, F. Balemnois, P. Georges, “On thermal effects in solid state lasers: the case of ytterbium-doped materials”, *Progress in quantum electronics*, Vol. **30**, pp. 89-126 (2007).
- [40] T. Graupeter, R. Hartmann, C. Pflaum, „Calculations of Eigenpolarization in Nd:YAG Laser Rods due to Thermally Induced Birefringence”, *Journal of quantum electronics*, Vol. **50**, Iss.12 (2014); doi: 10.1016/j.pquantelec.2006.12.001
- [41] D. Asoubar, F. Wyrowski, “Fully vectorial laser resonator modeling of continuous-wave solid-state lasers including rate equations, thermal lensing and stress-induced

-
- birefringence”, *Opt. Express*, Vol. **23**, Iss. 15, 18802-22, (2015), doi: 10.1364/OE.23.018802.
- [42] S. Zhang, F. Wyrowski, “Fully vectorial simulation of light propagation through uniaxial and biaxial crystals”, *SPIE Photonics Europe, Proceeding* (2016); doi: 10.1117/12.2234310.
- [43] H. Bremmer, “The W.K.B approximation as the first term of a geometric-optical series,” *Commun. Pure. Appl. Math.*, Vol. **4**, pp. 105–115 (1951).
- [44] F. Wyrowski, M. Kuhn, “Introduction to field tracing,” *J. Mod. Opt.*, Vol. **58**, pp. 449–466 (2011).
- [45] D. W. Berreman, “Optics in stratified and anisotropic media: 4×4 -matrix formulation,” *J. Opt. Soc. Am.*, Vol **62**, pp. 502–510 (1972).
- [46] G. D. Landry, T. A. Maldonado, “Gaussian beam transmission and reflection from a general anisotropic multilayer structure,” *Appl. Opt.*, Vol. **35**, pp. 5870–5879 (1996).
- [47] L. Li, “Reformulation of the Fourier modal method for surface-relief gratings made with anisotropic materials,” *J. Mod. Opt.*, Vol. **45**, pp. 1313–1334 (1998).
- [48] L. Li, “Note on the S-matrix propagation algorithm,” *J. Opt. Soc. Am.*, Vol. **20**, pp. 655–660 (2003).
- [49] Physical optics design software “Wyrowski VirtualLab Fusion”, developed by Wyrowski Photonics UG, distributed by LightTrans GmbH, Jena Germany. <http://www.lighttrans.com>.
- [50] ANSYS, Inc., “Simulation Driven Product”, www.ansys.com.
- [51] C. Rothhardt, J. Rothhardt, A. Klenke, T. Peschel, R. Eberhardt, J. Limpert, A. Tünnermann “BBO-sapphire sandwich structure for frequency conversion of high power lasers,” *Opt. Mater. Express*, Vol. **4**, 1092 (2014).
- [52] D. Eimerl, L. Davis, S. Velsko E. K. Graham A. Zalkin, “Optical, mechanical, and thermal properties of barium borate,” *J. Appl. Phys.*, Vol. **62**, pp. 1968–1983 (1987).
- [53] W. Martienssen, H. Warlimont, *Springer handbook of condensed matter and materials data*, Springer (2005).

-
- [54] W. L. Bond, "Measurement of the refractive index of several crystals," *J. Appl. Phys.*, Vol. **36**, pp. 1674–1677 (1965).
- [55] I. H. Malitson, "Interspecimen comparison of the refractive index of fused silica," *J. Opt. Soc. Am.*, Vol. **55**, pp. 1205–1209 (1965).
- [56] V. G. Dmitriev, G. G. Gurzadyan, D. N. Nikogosyan, "Handbook of nonlinear optical crystals", Springer (1999).
- [57] NIST/SEMATECH "e-Handbook of Statistical Methods", <http://www.itl.nist.gov/div898/handbook/>, (2013).
- [58] M. Mäusezahl, M. Hornaff, T. Burkhardt, E. Beckert, "Mechanical Properties of Laser-jetted SAC305 Solder on Coated Optical Surfaces". *Physics Procedia*, Vol. **83**, pp. 532-539, Elsevier (2016)
- [59] P. Ribes-Pleguezuelo, B. Septriani, S. Zhang, E. Beckert, R. Eberhardt, F. Wyrowski, A. Tünnermann, "Solderjet bumping packaging technique optimization for the miniaturization of laser devices"; *Journal of the European Optical Society- Rapid Publications*, SpringerOpen, (2017); doi: [10.1186/s41476-017-0063-7](https://doi.org/10.1186/s41476-017-0063-7).
- [60] R. Paschotta, *Encyclopedia of Laser Physics and Technology*. https://www.rp-photonics.com/yag_lasers.html.
- [61] P. Ribes-Pleguezuelo, A. Moral Inza, M. Gilaberte Basset, P. Rodríguez, G. Rodríguez, M. Laudisio, M. Galan, M. Hornaff, E. Beckert, R. Eberhardt, A. Tünnermann, "Assembly processes comparison for a miniaturized laser used for the Exomars European Space Agency mission," *Opt. Eng.*, Vol. **55**. Iss.11, 116107 (2016); doi: 10.1117/1.OE.55.11.116107.
- [62] M. Bauer, "European payload selected for ExoMars 2018 surface platform," ESA Science and Robotic Exploration Communication Officer, <http://exploration.esa.int/mars/56934-european-payload-selected-forexomars-2018-surface-platform/> (2015).
- [63] C. Pérez, M. Colombo, D. Diaz, P. Santamaría, R. Ingley, Y. Parrot, S. Maurice, J. Popp, N. Tarcea, H.G.K. Edwards, "Raman laser spectrometer development for ExoMars," in 2013 European Planetary Science Congress, EPSC2013-935, EPSC Abstracts, Vol. **8**, Portugal (2013).

-
- [64] C. P. Marshall, M. Coyle, “Why choose Raman spectroscopy for the exploration of Mars?,” *Mater. Aust.*, Vol. **39**, Iss.5, pp. 26–28 (2006).
- [65] F. Rull, S. Maurice, E. Diaz, G. Lopez, A. Catala, and the RLS Team, “The Raman laser spectrometer (RLS) on the Exomars 2018 rover mission,” in 42nd Lunar and Planetary Science Conf., USA (2011).
- [66] D. Guilhot, M. Gilaberte, S. Ferrando, P. Ribes, D. Montes, M. Galan, T. Burkhardt, E. Beckert, M. Hornaff, “Miniaturized frequency doubled DPSS assembled using solderjet bumping technology,” in Smart Systems Integration Conf., Netherlands (2013).
- [67] S. Ferrando, M. Galan, H. Thiele, M. Glier, M. Goepel, “Innovative optical techniques used in the Raman instrument for Exomars,” in Int. Conf. on Space Optics (ICSO), Greece (2010).
- [68] ECSS Secretariat, ESA-ESTEC, Requirements & Standards Division, “Space engineering testing,” <http://www.ecss.nl/forums/ecss/dispatch.cgi/standards/showFile/100824/d20120604160035/No/ECSS-E-ST-10-03C%281June2012%29.pdf> (2012).
- [69] A.W. Yu, S.X. Li, G.B. Shaw, A. Seas, M.A. Stephen, E. Troupaki, A. Vasilyev, L. Ramos-Izquierdo, A. Lukemier, W. Mamakos, A. Melak, J. Guzek, A. Rosanova, “Overview of space qualified solid-state lasers development at NASA Goddard Space Flight Center,” *Proc. SPIE*, Vol. **7193**, 719305 (2009).
- [70] M. W. Wright, H. Hemmati, “Pulsed fiber amplifiers in simulated space environmental tests,” *Proc. SPIE*, Vol. **8971**, 89710B (2016).
- [71] H. Yagi, K. Takaichi, K. Ueda, Y. Yamasaki, T. Yanagitani, A. A. Kaminskii, “The Physical Properties of Composite YAG Ceramics”, *Laser Physics*, Vol. **15**, Iss. 9, pp. 1338–1349, (2005).
- [72] M. Gilaberte-Basset, “Miniaturized frequency doubled DPSS laser soldered for space applications”. Universitat Politècnica de Catalunya (UPC), Barcelona, Spain (2014).
- [73] I. S. Raju, D. S. Lee, and M. Mohaghegh, “Negative stress margins—are they real?,” American Institute of Aeronautics and Astronautics, <http://ntrs.nasa.gov/archive/nasa/casi.ntrs.nasa.gov/20110010003.pdf> (2011).

-
- [74] ECSS Secretariat, ESA-ESTEC, Requirements & Standards Division, “Space engineering, Spacecraft mechanical loads analysis handbook,” http://www.vibrationdata.com/tutorials2/ECSS-E-HB-32-26A_19February2013.pdf (2013).
- [75] G. Azdasht, L. Titerle, “Method and device for applying a solder to a substrate,” U.S. Patent No. 20040069758 A1 (2002).
- [76] E. Beckert, T. Oppert, G. Azdasht, E. Zakel, T. Burkhardt, M. Hornaff, A. Kamm, I. Scheidig, R. Eberhardt, A. Tünnermann, F. Buchmann, “Solder jetting—a versatile packaging and assembly technology for hybrid photonics and optoelectronic systems,” in Proc. IMAPS 42nd Int. Symp. on Microelectronics, California, Vol. **42**, pp. 406 (2009).
- [77] T. Burkhardt, M. Hornaff, E. Beckert, R. Eberhardt, A. Tünnermann, “Parametric investigation of solder bumping for assembly of optical components,” Proc. SPIE, Vol. **7202**, 720203 (2009).
- [78] S. Kousar, “Highly Precised Soldering of End Mirrors of a Miniature Diode-Pumped Solid-State Laser for European Space Agency ExoMars Mission”, Friedrich Schiller University Jena, Germany (2014).
- [79] European Cooperation for Space Standardization, “ECSS-E-ST-32-01C Rev.1 Space Engineering- Fracture Control”, ESA Requirements and Standards Division, Noordwijk (2009).
- [80] E. Ritter, “Optical film materials and their applications”, Applied Optics., Vol. **15**, Iss. 10. (1976)
- [81] ECSS Secretariat, ESA-ESTEC, Requirements & Standards Division, “Space product assurance, radiation hardness assurance,” <https://escies.org/download/webDocumentFile?id=48643>, ESA-TEC-QE/2009/22, Issue 1 (2009).
- [82] M. Hoek, E.D. Bennet, D. Branford, E.N. Cowie, M. Düren, K. Föhl, D. Glazier, R. Kaiser, A. Lehmann, S. Lu, J. Marton, R. Ostendorf, G. Schepers, C. Schwarz, B. Seitz, A. Teufel, D. Watts, “Radiation hardness study on fused silica,” Nucl. Instrum. Methods Phys. Res., Vol. **595**. Iss. 1, pp. 190–193 (2008).

-
- [83] C. Barnes, R. Greenwell, “Radiation effects in photonic modulator structures,” Proc. SPIE, Vol. **2482**, 48 (1995).
- [84] ThalesAlenia, “ExoMars product assurance requirements for subcontractors,”http://emits.sso.esa.int/emits-doc/ALENIA/Exomars/ExoMars_Mission_2018/EXM-M2-RQM-AI-0067_v4.pdf (2015).
- [85] H. Hemmati, “Near-Earth Laser Communications (Optical Science and Engineering)”, CRC Press, (2009); ISBN 9780824753818.
- [86] D. Doyle, ESA-ESTEC, “Radiation Hardness of Optical Materials”, 3rd Europa Jupiter System Missions Instrument Workshop, (2010).
- [87] C.P. Canora, A.G. Moral, F. Rull, S. Maurice, I. Hutchinson, G. Ramos, G. Lopez-Reyes, T. Belenguer, R. Canchal, J.A.R. Prieto, P. Rodriguez, P. Santamaria, A. Berrocal, M. Colombo, P. Gallego, L. Seoane, C. Quintana, S. Ibarria, J. Zafra, J. Saiz, A. Santiago, A. Marin, C. Gordillo, D. Escribano, M. Sanz-Palomino, “How to improve a critical performance for an ExoMars 2020 Scientific Instrument (RLS). Raman Laser Spectrometer Signal to Noise Ratio (SNR) Optimization”, European Planetary Science Congress, EPSC Abstracts, Vol. 11, (2017).
- [88] ESA robotic exploration of mars “<http://exploration.esa.int/mars/59461-a-window-on-the-exomars-rovers-search-for-martian-life/>.
- [89] J. L. Vago, F. Westall, Pasteur Instrument Teams, Landing Site Selection Working Group, and other contributors, “Habitability on Early Mars and the Search for Biosignatures with the Exomars Rover”, *Astrobiology*, Volume **17**, Iss. 6 and 7, (2017); doi: 10.1089/ast.2016.1533.
- [90] European Space Agency, “Exomars Rover” http://www.esa.int/spaceinimages/Images/2017/03/ExoMars_rover. (2017).
- [S1] Majority of section of 2.3.1, 2.3.4 and 3.1 are reproduced from P. Ribes-Pleguezuelo, S. Zhang, E. Beckert, R. Eberhardt, F. Wyrowski, A. Tünnermann, “Method to simulate and analyse induced stresses for laser crystal packaging technologies”. *Optics Express*, Vol. **25**, Issue 6, pp. 5927-5940 (2017); doi: 10.1364/OE.25.005927, under the agreement of open access publication.

- [S2] Parts of the sections of the chapter 5 are reproduced from P. Ribes-Pleguezuelo, Andoni Moral Inza, Marta Gilaberte Basset, Pablo Rodríguez, Gemma Rodríguez, Marco Laudisio, Miguel Galan, Marcel Hornaff, Erik Beckert, Ramona Eberhardt, Andreas Tünnermann, “Assembly processes comparison for a miniaturized laser used for the Exomars European Space Agency mission,” *Opt. Eng.*, Vo. **55**, Iss. 11, 116107 (2016); doi: 10.1117/1.OE.55.11.116107, under the copy right agreement to let the authors prepare derivate publications, including books or book chapters.

Nomenclature

Symbols

| <i>Symbol</i> | <i>Full expression</i> | <i>Unit</i> |
|-----------------|-------------------------------------|--------------------------------|
| A | area | m ² |
| B_{ij} | indicatrix | |
| C | stress-optic coefficient | Pa |
| $C_{S,L}$ | heat capacity (solid, liquid) | J |
| c_{ijkl} | elastic stiffness tensor | Pa |
| d | diameter | μm |
| E | Young modulus | Pa |
| $E_{x,y,z}$ | electric field | V m ⁻¹ |
| F | force | N |
| g | acceleration | m s ⁻¹ |
| h | Planck constant | J s |
| H | enthalpy | J kg ⁻¹ |
| k | Boltzmann constant | J K ⁻¹ |
| l | length | mm |
| n | refractive index | |
| N | normal force | N |
| M ² | beam quality factor | |
| p | parallel polarization of light | |
| R | radius | mm |
| s | perpendicular polarization of light | |
| t | thickness | mm |
| T | temperature | K |
| UTS | ultimate tensile strength | MPa |
| α | CTE difference | K ⁻¹ |
| δ | density | kg/m ³ |
| Δ | optical retardation | nm |
| ε | dielectric permittivity | F m ⁻¹ |
| ϵ_{ij} | dielectric constant (tensor) | F m ⁻¹ |
| ε | extensional strain | m |
| ϵ_{kl} | extensional strain (tensor) | m |
| λ | wavelength | nm |
| μ | friction | |
| ν | Poisson's ratio | - |
| ν ₂₁ | frequency | Hz |
| π_{ijkl} | piezo-optic tensor | m ² N ⁻¹ |
| σ | mechanical stress | N m ⁻² |
| σ_{ij} | mechanical stress (tensor) | N m ⁻² |
| τ | yield strength | MPa |

Abbreviations

| | |
|-------------------|--|
| AlN | Aluminum Nitride |
| AR | Anti-Reflective |
| BBO | Barium Borate |
| CAD | Computer-Aided Design |
| CVCM | Collected Volatile Condensable Materials |
| CTE | Coefficient of Thermal Expansion |
| CW | Continuous-Wave |
| DCB | Direct Copper Bonding |
| DoE | Design Of Experiments |
| DOF | Degrees Of Freedom |
| DPSSL | Diode-Pumped Solid-State Laser |
| ESA | European Space Agency |
| EQM | Engineering Qualification Model |
| FAC | Fast Axis Collimator |
| FEM | Finite Element Method |
| FM | Flight Model |
| FS | Fused Silica |
| FWHM | Full Width at Half Maximum |
| GdVO ₄ | Gadolinium Vanadate |
| iOH | Internal Optical Head |
| HR | High Reflection |
| HT | High Transmission |
| IR | Infrared Radiation |
| ICEU | Instrument Control and Excitation Unit |
| KGW | Potassium-Gadolinium Tungstate |
| KTP | Potassium titanyl phosphate (KTiOPO ₄) |
| LBO | Lithium triborate (LiB ₃ O ₅) |
| LIC | Laser-Induced Contamination |
| LID | Laser-Induced Damage |
| MEMS | MicroElectroMechanical Systems |
| NASA | National Aeronautics and Space Administration |
| Nd | Neodymium |
| NIR | Near Infrared |
| RADEF | Radiation Effects Facility |
| RLS | Raman Laser Spectrometer |
| SAC305 | Sn96.5%, Ag3%, Cu0.5% |
| SHG | Second Harmonic Generator |
| SPU | Spectrometer Unit |
| TEM ₀₀ | Transverse mode of ElectroMagnetic radiation lowest order or fundamental, equal to a Gaussian beam |
| TML | Total Mass Loss |
| TID | Total Ionizing Dose |
| UTS | Ultimate Tensile Strength |
| UV | Ultraviolet |
| VCSEL | Vertical-Cavity Surface-Emitting Laser |
| VIS | Visible |
| YAG | Yttrium Aluminum Garnet |

Prefixes

| Symbol | Prefix | 10^n |
|--------|--------|------------|
| G | Giga | 10^9 |
| M | Mega | 10^6 |
| k | Kilo | 10^3 |
| m | Milli | 10^{-3} |
| μ | Micro | 10^{-6} |
| n | Nano | 10^{-9} |
| p | Pico | 10^{-12} |

List of publications

Refereed publications

First author:

- P. Ribes, C. Koechlin, M. Hornaff, A. Kamm, E. Beckert, G. Fiault, R. Eberhardt, A. Tünnermann, “High-precision opto-mecanical lens system for space applications assembled by innovative local sodlring technique”, *Opt. Eng.*, Vol **55**, Iss. 6, 065101 (2016); doi:10.1117/1.OE.55.6.065101.
- P. Ribes-Pleguezuelo, Andoni Moral Inza, Marta Gilaberte Basset, Pablo Rodríguez, Gemma Rodríguez, Marco Laudisio, Miguel Galan, Marcel Hornaff, Erik Beckert, Ramona Eberhardt, Andreas Tünnermann, “Assembly processes comparison for a miniaturized laser used for the Exomars European Space Agency mission,” *Opt. Eng.*, Vo. **55**, Iss. 11, 116107 (2016); doi: 10.1117/1.OE.55.11.116107.
- P. Ribes-Pleguezuelo, S. Zhang, E. Beckert, R. Eberhardt, F. Wyrowski, A. Tünnermann, “Method to simulate and analyse induced stresses for laser crystal packaging technologies”. *Optics Express*, Vol. **25**, Issue 6, pp. 5927-5940 (2017); doi: 10.1364/OE.25.005927.
- P. Ribes-Pleguezuelo, B. Septriani, S. Zhang, E. Beckert, R. Eberhardt, F. Wyrowski, A. Tünnermann, “Solderjet bumping packaging technique optimization for the miniaturization of laser devices”, *Jounral of the European Optical Society- Rapid Publications*, SpringerOpen, (2017); doi: 10.1186/s41476-017-0063-7.
- P. Ribes-Pleguezuelo, K. Frei, G. Bruckner, E. Beckert, R. Eberhardt, A. Tünnermann, “Lithiumniobate Die Assembled by a Low-stress Soldering Technique- Method to Fasten a Surface Acoustic Wave Sensor”, accepted after a peer review process at the 6th International Conference on Photonics, Optics and Laser Technology PHOTOPTICS on 11/2017, Madeira, Portugal (2018).

Co-author:

- T. Burkhardt, M. Seifert, P. Ribes, N. Lange, G. Lopez-Reyes, A. Moral-Inza, A. Sansano, “Laser-based Soldering Technique for Hermetical Sealing of the Calibration Target for Exomars‘ Raman Instrument“. In Proceedings of the 4th International Conference on Photonics, Optics and Laser Technology, PHOTOPTICS, Rome, Italy (2016); doi: 10.5220/0005653200550061.

Non-refereed publications:

First author:

- P. Ribes, T. Burkhardt, M. Hornaff, S. Kousar, D. Burkhardt, E. Beckert, M. Gilaberte, D. Guilhot, D. Montes, M. Galan, S. Ferrando, R. Eberhardt, A. Tünnermann, “Solderjet technology used to assemble a robust miniaturized solid-state laser”. OPTICS & PHOTONICS International Congress 2014. The 2nd. Laser Ignition Conference (LIC'14), Yokohama, Japan (2014).
- P. Ribes, T. Burkhardt, M. Hornaff, S. Kousar, D. Burkhardt, E. Beckert, M. Gilaberte, D. Guilhot, D. Montes, M. Galan, S. Ferrando, M. Laudisio, T. Belenguer, S. Ibarria, P. Gallego, J. A. Rodríguez, R. Eberhardt, A. Tünnermann, “Solderjet bumping technique used to manufacture a compact and robust green solid-state laser”, Proc. SPIE 9520, Integrated Photonics: Materials, Devices, and Applications III, 952009, Barcelona, Spain, (2015); doi:10.1117/12.2178373.
- P. Ribes, C. Koechlin, T. Burkhardt, M. Hornaff, D. Burkhardt, A. Kamm, S. Gramens, E. Beckert, G. Fiault, R. Eberhardt, A. Tünnermann., “High-precision opto-mecanical lens system for space applications assembled by innovative local soldering technique”, SPIE Proceed. Photonics West 2016, *Proc. SPIE* 9750, Integrated Optics: Devices, Materials, and Technologies XX, **97501K**, San Francisco, USA (2016); doi:10.1117/12.2208123.
- P. Ribes-Pleguezuelo, C. Koechlin, T. Burkhardt, M. Hornaff, A. Kamm, S. Gramens, E. Beckert, G. Fiault, R. Eberhardt, A. Tünnermann, “ Low-Stress soldering technique used to assemble an optical system for aerospace missions”, International Conference on Space Optics (ICSO), Biarritz, France, (2016).

-
- P. Ribes-Pleguezuelo, S. Zhang, E. Beckert, R. Eberhardt, F. Wyrowski, A. Tünnermann, “Study of a Laser Packaging Technique Simulated with ANSYS and VirtualLab Fusion Software”, The 5th. Laser Ignition Conference (LIC'17), Bucharest, Rumania (2017); doi: /10.1364/LIC.2017.LWA2.4.

Co-author:

- T. Burkhardt, E. Beckert, M. Hornaff, J. Thiele, D. Burkhardt, M. Galan, M. Gilaberte, S. Ferrando, D. Montes, P. Ribes, R. Eberhardt, A. Tünnermann, “Solder joining of a miniaturized laser on a multi-material smart platform”, Smart System Integration Conference, International Conference & Exhibition on Integration Issues of Miniaturized Systems – MEMS, Switzerland (2012).
- D. Guilhot, M. Gilaberte, S. Ferrando, P. Ribes, D. Montes, M. Galan, T. Burkhardt, E. Beckert, M. Hornaff, “Miniaturized frequency doubled DPSS assembled using solderjet bumping technology,” in Smart Systems Integration Conf., Netherlands (2013).
- T. Burkhardt, M. Hornaff, P. Ribes, A. Kamm, D. Burkhardt, S. Kousar, E. Beckert, R. Eberhardt, A. Tünnermann, “Laserlöten optischer Systeme – Anwendungen des Solderjet Bumpings,“ 9. Jenaer Lasertagung 2014, in: DVS-Berichte Band 370, Innovative Fertigung durch Lasersysteme neuester Generation, Vorträge und Posterbeiträge der 9. Jenaer Lasertagung am 20. und 21. November 2014, DVS Media, Düsseldorf, (2014); ISBN 978-3-945023-04-4, ISSN 0418-9639.
- M. Hornaff, T. Burkhardt, P. Ribes-Pleguezuelo, M. Mohaupt, B. Zaage, A. Kamm, E. Beckert, R. Eberhardt, “Laserlöten hochpräziser optischer Mikrosysteme- Laserbased Soldering of highprecision micro-optical Systems”, Mikrosystemtechnik Kongress, Germany (2015).
- B. Septriani, P. Ribes-Pleguezuelo, E. Beckert, R. Eberhardt, A. Tünnermann, “Bond strength and stability of solderjet bumping packaging technique for laser device miniaturization”, submitted to the International Conference and Exhibition of Smart Systems Integration on 10/2017, Dresden, Germany (2018).

Presentations

- P. Ribes, T. Burkhardt, M. Hornaff, S. Kousar, D. Burkhardt, E. Beckert, M. Gilaberte, D. Guilhot, D. Montes, M. Galan, S. Ferrando, R. Eberhardt, A. Tünnermann, “Solderjet technology used to assemble a robust miniaturized solid-state laser”. OPTICS & PHOTONICS International Congress 2014 The 2nd. Laser Ignition Conference (LIC'14), April 2014, Yokohama, (Japan).
- P. Ribes, T. Burkhardt, M. Hornaff, S. Kousar, D. Burkhardt, E. Beckert, M. Gilaberte, D. Guilhot, D. Montes, M. Galan, S. Ferrando, M. Laudisio, T. Belenguer, S. Ibarria, P. Gallego, J. A. Rodríguez, R. Eberhardt, A. Tünnermann, “Solderjet bumping technique used to manufacture a compact and robust green solid-state laser”, SPIE, Integrated Photonics: Materials, Devices, and Applications III, May, 2015, Barcelona (Spain).
- P. Ribes-Pleguezuelo, C. Koechlin, T. Burkhardt, M. Hornaff, A. Kamm, S. Gramens, E. Beckert, G. Fiault, R. Eberhardt, A. Tünnermann, “ Low-Stress soldering technique used to assemble an optical system for aerospace missions”, International Conference on Space Optics (ICSO), October 2016, Biarritz, (France).
- P. Ribes-Pleguezuelo, S. Zhang, E. Beckert, F. Wyrowski, R. Eberhardt, A. Tünnermann, “Study of a Laser Packaging Technique Simulated with ANSYS and VirtualLab Fusion Software”, The 5th. Laser Ignition Conference (LIC'17), June 2017, Bucharest, (Rumania).
- P. Ribes-Pleguezuelo, K. Frei, G. Bruckner, E. Beckert, R. Eberhardt, A. Tünnermann, “Lithiumniobate Die Assembled by a Low-stress Soldering Technique- Method to Fasten a Surface Acoustic Wave Sensor”, accepted after a peer review process at the 6th International Conference on Photonics, Optics and Laser Technology PHOTOPTICS on 11/2017, January 2018, Madeira, (Portugal).

Poster

- P. Ribes, C. Koechlin, T. Burkhardt, M. Hornaff, D. Burkhardt, A. Kamm, S. Gramens, E. Beckert, G. Fiault, R. Eberhardt, A. Tünnermann., “High-precision opto-mecanical lens system for space applications assembled by innovative local soldering technique”, SPIE Photonics West 2016, 13-18 February 2016 San Francisco, California, (USA).

Acknowledgements

First of all, I would like to thank Dr. Erik Beckert for his trust during the years I have spent at the Fraunhofer IOF. He has been a great boss, always with an open door and open mind to hear any new ideas, requests or suggestions. To Prof. Andreas Tünnermann and Dr. Ramona Eberhardt, for accepting me at IOF, and for their support and supervision. I would also like to thank Miguel Galan, one of the founders of Monocrom Company, from whom I learned almost all I know about laser devices. He is a crazy genius, a mentor and a friend. No less, I would like to thank Dr. Sergi Ferrando, the former head of the R&D department at Monocrom, to let me take over responsibilities and also for the trust he put in me. These five persons are the main reason why I started this personal project that ended up in this PhD thesis.

I would like also to mention Zhe Shu, Rossá Mac Ciarnaín, Sophie Sauva and Aoife Brady. They have been brothers in arms and partners in crime, and because work without friendship is meaningless. Also, all Fraunhofer Institute for Applied Optics and Precision Engineering, specially the soldering group, from them I learned a lot; the mechanical workshop; and the glass department of *meine lieblich* Leibelung, where I improved my German. Also, thanks to all students who helped to carry out some test for the Exomars project, especial thanks to Sumera Kousar, Muhammad Assad Arshad and Brigitta Septriani.

I have to include also Marta Gilaberte, for chasing me in almost any step of my life since University.

From Monocrom I would also like to mention David Montes, responsible for many of the designs of the Exomars lasers, and Dani. Two persons that deserve much more recognition as they will ever have.

It has been now my fourth year in Jena, and this I have to thank it to Frau/Komissar/Dr./Amish Julia Schneider for helping me to settle and turn this small city in something I can also call home. I am sure without you Jena would not be Jena.

I have/must include my Physics-Rock-mariachi-band High Energy Shift (soon in the best music festivals), Pol di Alonso, Lorena FlordeLeon, Cast-away Oscar, Mateusz Jesus-Oleszko, Florencia Flor de Campetella, Odlo (the freedom giver), Jannik “it’s a Trapp!”, Robert (also known as the ghost photographer), Shulin and Florian Müller.

Also to my cousins Lluna Pleguezuelo and Dr. Sandra Ribes. Especially to Sandra for being part of my German family and a model person to respect and follow. It is nice to have a close and growing family for which I have the chance to contribute with memories and episodes. For this, I also thank to the little rock star Nora, the future brilliant pseudo-villain or super-hero Viktor, and for one of the greatest/good man and kind father that ever existed, Dr. Sergi Papiol.

And to Dr. Lilia Espada, my gintonic-friend with a Nature paper, and Dr. Denis Gilhot for the Rickies nights and the friendship that will for sure continue for many more years (even in the distance).

Finally, to the tennis player Roger Federer because he always had an eye on me. And to my beloved Agnieszka Małysz for being a point in my life, whatever this was good or bad.

I dedicate this work to my parents, my creators and my gods; for building Lego piece by Lego piece thanks to the applied matter and time the bases of who I am.

Ehrenwörtliche Erklärung

Ich erkläre hiermit ehrenwörtlich, dass ich die vorliegende Arbeit selbstständig, ohne unzulässige Hilfe Dritter und ohne Benutzung anderer als der angegebenen Hilfsmittel und Literatur angefertigt habe. Die aus anderen Quellen direkt oder indirekt übernommenen Daten und Konzepte sind unter Angabe der Quelle gekennzeichnet. Bei der Auswahl und Auswertung folgenden Materials haben mir die nachstehend aufgeführten Personen in der jeweils beschriebenen Weise unentgeltlich geholfen:

1. Site Zhang (IAP, Jena): VirtualLab Fusion software, for helping to open the path into the stress-induced birefringence with VirtualLab Fusion.

Weitere Personen waren an der inhaltlich-materiellen Erstellung der vorliegenden Arbeit nicht beteiligt. Insbesondere habe ich hierfür nicht die entgeltliche Hilfe von Vermittlungs- bzw. Beratungsdiensten (Promotionsberater oder andere Personen) in Anspruch genommen. Niemand hat von mir unmittelbar oder mittelbar geldwerte Leistungen für Arbeiten erhalten, die im Zusammenhang mit dem Inhalt der vorgelegten Dissertation stehen. Die Arbeit wurde bisher weder im In- noch im Ausland in gleicher oder ähnlicher Form einer anderen Prüfungsbehörde vorgelegt. Die geltende Promotionsordnung der Physikalisch-Astronomischen Fakultät ist mir bekannt.

Ich versichere ehrenwörtlich, dass ich nach bestem Wissen die reine Wahrheit gesagt und nichts verschwiegen habe.

Jena,

.....

Pol Ribes Pleguezuelo